Mechanisms and function of asynchronous flight motor pattern generation

Dissertation zur Erlangung des Grades Doktor der Naturwissenschaft

Am Fachbereich Biologie
Johannes Gutenberg - Universität Mainz
Institut für Entwicklungsbiologie und Neurobiologie

Silvan Hürkey

geb. am 22.08.1991 in Seeheim-Jugenheim a.d.B.

Mainz, 2023

Dekan: Prof. Dr. Eckhard Thines

Erstgutachter:

Zweitgutachter:

Tag der mündlichen Prüfung: 16.11.2023

Table of contents

Abbreviations

AIFM = asynchronous indirect flight muscle

AP = Action potential

CBX = Carbenoxolone

ChR = Channelrhodopsin

CPG = central pattern generation

DLM = dorsal longitudinal muscle

DVM = dorsoventral muscle

GCaMP = GFP calmodulin binding domain

GFP = green fluorescent protein

GJs = Gap junctions

GluCl = glutamate gated chloride channel

HOM = saddle homoclinic orbit

ISI = inter spike interval

IPI= inter pulse interval

MN = motoneuron

oe = overexpression

PDMN = posterior dorsal mesothoracic nerve

PTX = picrotoxin

Rdl= Resistant to dieldrin

SERCA = sarco/endoplasmic reticulum Ca^{2+}-ATPase

SNIC = saddle node on an invariant cycle

SNL = saddle node loop

SR = sarcoplasmic reticulum

STG = stomatogastric ganglion

VNC = ventral nerve cord

wb = wingbeat

Summary

The vast majority of insect species and therefore overall species uses asynchronous indirect flight as locomotion. Highly specialized muscles generate the power for the up and down stroke of the wing and are the most energy consuming tissues in biology. In *Drosophila melanogaster* a small network of five motoneurons (MNs) controls the activity of the wing depressor muscle. The firing pattern of these five MNs is well described, as a firing equidistantly splayed-out in time and in a preferred sequence. The approximate firing rate of ~5 Hz is asynchronous, hence the name, to the muscle contraction frequency of around 200 Hz. However, the mechanism that generates this splayed firing pattern and the functional consequences are not yet fully understood.

This thesis will describe how the motor pattens are generated by a minimal central pattern generating network (CPG) that consists of five electrically coupled MNs and translates common, unpatterned, cholinergic, excitatory input into splayed-out patterned firing of the MNs. For a given power demand all MNs fire at similar frequencies but in specific sequences, thus desynchronized. Mechanistically, weak electrical coupling together with a specific excitability class is responsible for network desynchronization. Increasing or decreasing the expression of the gap junction protein ShakB through genetic manipulation disrupts the splay state and increases MN firing synchronization, leading to wingbeat frequency fluctuations during flight. Changing the excitability class of the electrically coupled MNs using genetic manipulation of the Shab delayed rectifier potassium channel also shifts network activity to a more synchronized state. The functional consequence of the desynchronized splayed-out motor patterns is to minimize fluctuations in wingbeat frequency. *In vivo* calcium imaging in single muscle fibers reveals the kinetics of myoplasmic Ca^{2+}-signals, which can be used to link the MN firing pattern and the wingbeat frequency fluctuations: Splayed-out MN firing minimizes fluctuations of average myoplasmic Ca^{2+}-levels across all muscle fibers, ultimately allowing a uniform wingbeat frequency and thus a steady power output over time. The capability of weak electrical coupling together with the right neuronal excitation class to desynchronize network activity has far-reaching implications for neuronal network activity, since gap junction proteins are ubiquitously expressed in neuronal networks throughout different species. It provides a novel mechanism for different synchronization states in all nervous systems, from flies to humans.

1 Introduction

While for some the baffling fast flight maneuvers of flies are a nuisance, others are inspired to discover the intricate machinery that makes such feat possible. Great discoveries have been made from describing morphology and behavior in miniscule detail to the underlying genetics, biomechanics and physiology, but there are plenty of discoveries to be made. In this thesis I want to give further insight into how the nervous system of *Drosophila melanogaster* regulates the power output for the wingbeat during flight and answer some fundamental questions. What are the activity patterns of motoneurons to asynchronous muscles during flight? What is the architecture of the central pattern generating network that produces patterned output from flight motoneurons to wing power muscles? What are the network mechanisms that underlie the specific motor patterns observed in insects during asynchronous flight? What are the functional consequences of the patterned activity of flight motoneurons during asynchronous flight? To address these questions, I combine the genetic tools available in the Drosophila model system with electro- and optophysiology, neuroanatomy, and high-speed video recordings. In collaboration with the group of Prof. Dr. S. Schreiber (Humboldt University Berlin), my physiological findings are incorporated into computational models and theory to make predictions, which are in turn verified by physiological experiments.

1.1 Insect flight

With over one million described species, insects are the species richest lifeform (Stork, 2018). They are found in nearly all ecosystems and can thrive under the most challenging conditions. Their evolutionary success is not only driven by their small body size, but also by the fact that they are the only invertebrates with the ability to fly. Flying insects cover three orders of magnitude in body size, ranging from 0.15 mm small fairyflies to 15 cm big Hercules beetles. Multiple forms of insect flight evolved over hundreds of millions of years: the most primordial mode evolving around 400 million years ago during a time with a notably high atmospheric oxygen level and is the first time animals achieved flight (Dudley, 2000). It is called synchronous flight and used by lower insect species with low wingbeat frequencies, like dragonflies (*Odonata*), butterflies, moths (*Lepidoptera*) and locusts (*Orthoptera*) (Cao & Jin, 2020). For this a *synchronous* muscle is used, where the MN activity is synchronous to the muscle

contraction or wingbeat frequency. One notable difference in flight muscle architecture is how they are connected to the wing base. In dragonflies (*Odonata*) and mayflies (*Ephemeroptera*) muscles are directly linked to the wing base, therefore called direct flight muscle. Contrary to that, all remaining insect orders use indirect flight muscles, where the muscle is connected to the cuticle of the thorax. The deformation of the cuticle is indirectly moving the wing (Deora et al., 2017).

At least 75% of all insect species are asynchronous flyers, making it the most used form of locomotion in terms of species count. To this end, a highly specialized muscle called the asynchronous muscle evolved, capable of strong contractions at high frequencies. Especially smaller insects are relying on this modality to achieve high wingbeat frequencies. For small insects, high wingbeat frequencies are necessary, since the equation describing the aerodynamic forces depends on the wing length to the 4th power, whereas the volume decreases only with a 3rd power. This means, the smaller the animal and the shorter the wings, the higher the wingbeat frequency for the same amount of lift, while at the same time the relative body volume for the muscles to generate the required force is lost (Deora et al., 2017). Probably, these constraints led to the evolution of the most energy demanding tissue in biology (Wegener, 1996). And still, a large volume of the body is attributed to the flight power muscle. Therefore, a precise control of this muscle is crucial for the efficiency of the system. The motor control for the asynchronous muscle is temporally decoupled between the motoneuron (MN) firing and the muscle contraction, hence the name asynchronous muscle. Additionally, one action potential (AP) of a MN can be sufficient to generate ~40 contractions of the innervated muscle fiber in case of *Drosophila*. This is a fundamentally different concept in comparison to synchronous muscle control in vertebrates and insects with synchronous flight, with MN firing synchronous to the muscle contraction in a 1:1 ratio. For asynchronous flight this MN firing and muscle contraction relation is more complex and not completely understood making it a particularly intriguing topic to unravel in greater depth. In the following I will give an overview of motor control in general and introduce the flight system of the fruit fly to provide a deeper understanding of asynchronous flight and answer the main question of this dissertation: How does *Drosophila* generate a flight motor pattern for its power muscle and what are the consequences of this motor pattern for the power output?

1.2 Motor control of locomotion

Locomotion is the ability to move through the environment and is a fundamental behavior of animals. Active locomotion requires animals to exert force on their environment to move their bodies through space. Most often, this is done through appendages adapted to the elements they interact with to maximize this force. Rhythmic movement then enables swimming, walking, and flying. This seemingly simple behavior is only possible through a complex cascade of processes. An animal must process sensory information to perceive its position in space and time, as well as the relative positions of its appendages or joints to each other. Moreover, it has to create a motor plan to navigate in the intended direction while integrating new sensory input and correcting the plan if perturbations occur.

Muscular, skeletal, respiratory, circulatory, and nervous system have to interact in an organized manner to allow locomotion. The main center to coordinate these systems is the nervous system. To generate a motor program for rhythmic behavior the nervous system developed specialized circuits called central pattern generators (CPGs). These circuits consist of interconnected neurons which receive an unpatterned input and generate a patterned output, without the need of sensory feedback. Although sensory input is by definition not required for pattern generation in these networks, CPG network activity is constantly adjusted to different demands by sensory feedback. Not only locomotion but also other rhythmic behaviors like breathing, chewing, heartbeat or sound production rely on CPGs (for reviews: Guertin, 2009; Katz, 2016). CPGs were first discovered in cat (Brown, 1911) and later in crayfish (Wiersma & Hughes, 1961), locusts (B. Y. D. M. Wilson, 1961) and over the years in many other invertebrates and vertebrates (Delcomyn, 1980). It was not until 1988 that evidence of CPGs in humans were discovered (Bussel et al., 1988) and there is still no definitive proof, because there is no human injury model in which peripheral feedback and supraspinal control are completely absent (Minassian et al., 2017). However, CPGs are also thought to generate the patterned activity of spinal motoneurons that underlies human bipedal gait. The simplest form of a CPG is Brown's half-center model (Fig. 1). Two premotor neuron groups receive tonic input and inhibit each other reciprocally to produce an alternating rhythmic output on the flexor MNs and the extensor MNs.

The group of neurons that activates the flexor is the flexor half-center, and the group that activates the extensor, is the extensor half-center. This model was proposed by Graham Brown in 1911, when he conducted research on spinal cord transected cats and contradicted the view that locomotion is a concatenation of reflexes relying on proprioceptive feedback and the involvement of higher centers (Brown, 1911). First evidence supporting this model of central pattern generation were achieved through intracellular recordings in cat in the 60s (Jankowska et al., 1967; Lundberg, 1965). However the idea of a network generating a motor pattern without

Half-center model

Figure 1: The half center model shows interneurons (blue) and extensor/flexor motoneurons (white) interconnected via inhibitory (o) and excitatory (v) synapses. This circuit leads to alternating activation of extensor and flexor (Guertin, 2009).

sensory feedback was first formulated for invertebrates (Holmes Bullock, 1961; D. M. Wilson & Wyman, 1965). In the following decades models of CPGs became more elaborate. One of the best understood CPGs to date is the stomatogastric ganglion (STG) of the lobster (*H. americanus*) or crab (*C. borealis*). The STG is a great model system, because it can be removed from the animal into a dish where it can generate a fictive motor pattern, which is also true for many other animals as lampreys, locusts or *aplysia*. But especially STG recordings can last up to 24 h and cultured STGs can be even viable for 8 days (Mizrahi et al., 2001). The STG in the crab has 25-26 neurons while the lobster 29-32. The network can be divided into the neurons for the gastric mill and the pylorus. In the pyloric rhythm different burster neurons are firing in three phases with approximately 1 Hz. Inhibitory chemical synapses lead to anti-phasic bursting while electrical synapses lead to synchronous bursting and generate a triphasic firing pattern (Marder & Bucher, 2007). The anterior burster (AB) is an intrinsic oscillator and is electrically coupled to the pyloric dilator neurons (PD). These oscillations drive the PY to fire bursts of APs. The lateral pyloric neuron (LP) and the PYs are inhibited during these bursts of AB and PD by chemical synapses. The LP is rebounding sooner than the PYs and when LP finished the PYs follow (Marder & Bucher, 2007; Fig. 2b right panel). Therefore, mechanistically, central pattern generation is based on the network structure and the intrinsic membrane properties of the component neurons.
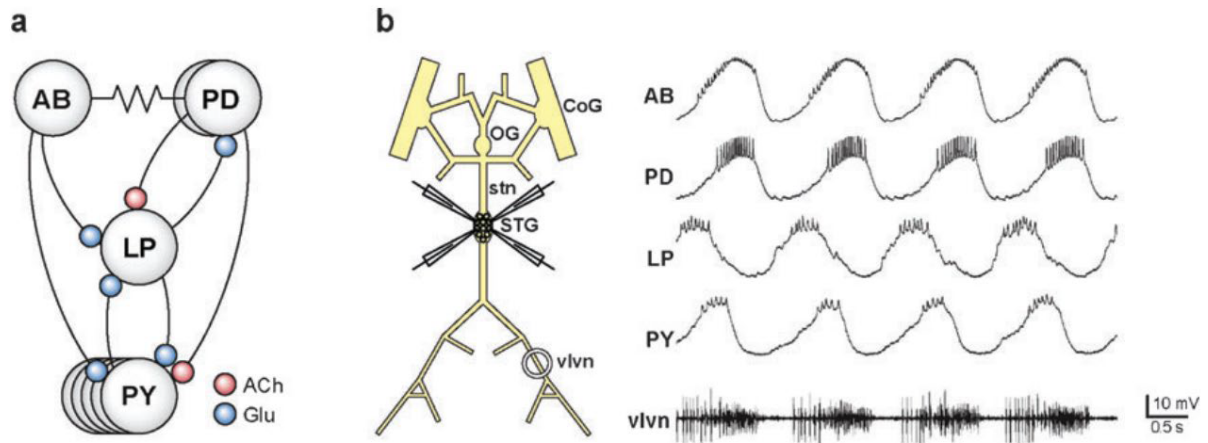
Figure 2: Motor pattern of the pylorus CPG, including the anterior burster (AP), the pyloric dilator (PD), lateral pyloric (LP) neuron and the pyloric (PY) neurons. **A** Pylorus CPG circuit with inhibitory synapses in red and blue. Electrical synapse as resistor. **B** Localization of stomatogastric nervous system with patch pipettes and motor pattern of the pyloric CPG (Marder and Bucher, 2007).

Since the motor pattern is established, it can be used to analyze neuromodulation. Reagents can be applied and the resulting changes in the firing pattern can be measured. This led to the discovery that all neurons in the pyloric CPG are affected by modulators and many neuromodulators cause the production of different motor programs (Flamm & Harris-Warrick, 1986b, 1986a). Therefore, it is a valuable tool to investigate the effect of substances not only on single neurons but on a whole network. There are many more investigated CPGs, from relatively small networks controlling leech heartbeat or swimming (Kristan et al., 2005) to large and complex networks controlling vertebrate respiration (Smith et al., 2013) or walking (Guertin, 2009). They all have in common that a core central network can produce patterned output that depends on the network architecture and intrinsic neuronal properties, and typically both, synaptic strength and intrinsic membrane properties can be adjusted by neuromodulation.

1.3 Insect flight CPG

Wilson was one of the first to investigate the flight CPG of the blow fly *Calliphora* and his student Wyman discovered the out of phase activity of single muscle fibers within one muscle (R. Wyman, 1965). This was later also shown in *Drosophila melanogaster* by Levine (J. Levine, 1973). Wilson and Wyman attributed the asynchronous splayed-out activity of the MNs to reciprocal inhibition via chemical synapses between the MNs themselves (Harcombe & Wyman, 1977). Koenig and Ikeda however, argued that

weak electrical coupling is sufficient to generate the firing pattern (Koenig & Ikeda, 1983). Up until now these two mechanisms are still under debate. In 2007 Schlurmann and Hausen published a paper showing dye coupling between the DLM-MNs in *Calliphora erythrocephala* and announced a paper in preparation to show electrical coupling in electrophysiological recordings. With regard to firing pattern and morphology of MNs *Drosophila* and *Calliphora* are similar, and therefore, the announced work by (Schlurmann & Hausen, 2007) hints to electrical coupling also in *Drosophila,* but the paper was never published.

If synapses between the MNs shape the motor patterns without requiring patterned input from interneurons, this would imply that MNs take over the function of a CPG, which is commonly constituted of interneurons. It was previously shown that MNs can also be involved in the pattern generation (Brodfuehrer et al., 1995; Marder & Calabrese, 1996; Matsunaga et al., 2017; Song et al., 2016). In the STG, most CPG neurons are interneurons and MNs, because they innervate muscles but also form chemical and electrical output synapses in the CPG network, but there is no example where only MNs are responsible for pattern generation.

1.4 *Drosophila melanogaster* flight system and behavior

To highlight the physiological context and the demands that the motor control system of wing power muscles has to meet, I will next introduce the flight system of *Drosophila melanogaster*.

As all Diptera, the fruit fly has only one pair of wings, and the hind wings evolved into halteres. These small appendages oscillate antisynchronously to the wingbeat and sense the positioning and movement of the fly via mechanoreceptors. Together with proprioceptive feedback from the wing they provide an equilibrium sense. Visual input is perceived by a pair of compound eyes and can be sufficient to start flight behavior via the giant fiber system (GFS). Fast on/off light signals are transferred via the giant fiber to the jump muscle (TTM) and the DLM-MNs to initiate flight. The optic flow created by the passing environment during flight is used to calculate the ground speed for flight (Lawson & Srinivasan, 2017). Regulating the flight speed in free flight is mainly done by tilting the body axis and therefore shifting the thrust vector, similar to a helicopter (David, 1978; Medici & Fry, 2012). But also wingbeat frequency and

amplitude are adapted to regulate flight speed (Dickinson et al., 2016; Dickinson & Muijres, 2016). Olfactory stimuli are sensed by two antennae and also influence flight behavior. The wings are connected to the thoracic shell, an elastic cuticle whose stiffness can be adjusted by fast muscle activity. The elasticity of the thorax and muscles is used to form a resonating system for energy efficient flight at high wingbeat frequencies (Pons et al., 2023). All the different sensory inputs are integrated by the nervous system to generate a flight motor pattern for the flight muscles to allow the appropriate behavior.

1.5 Drosophila melanogaster flight muscles
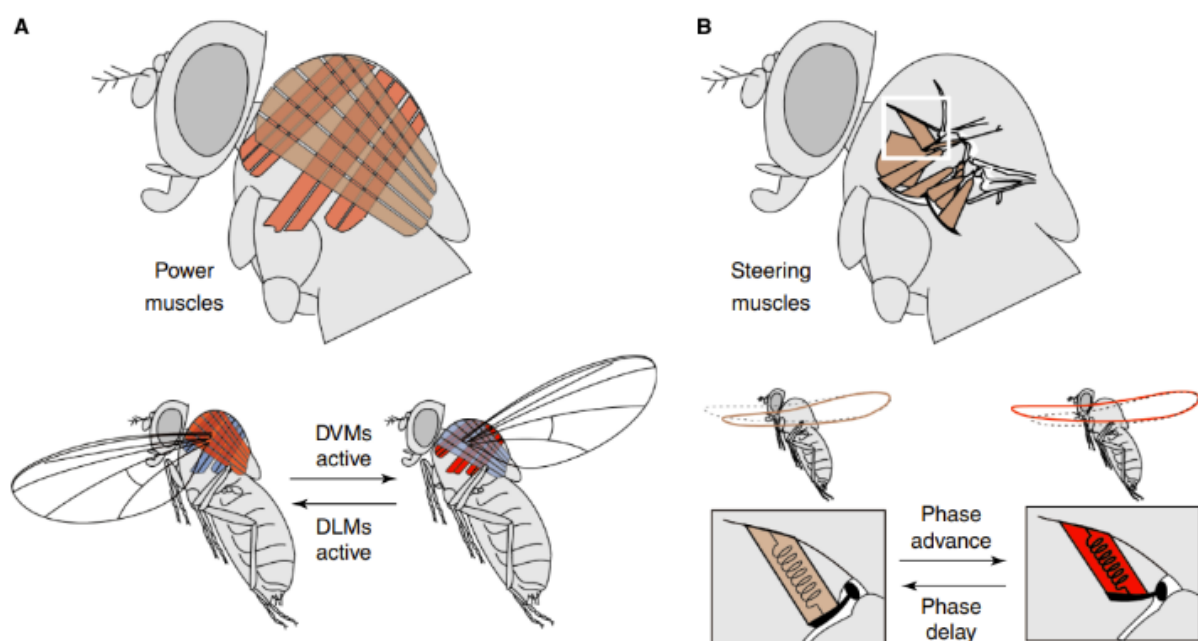
Figure 3: Schematic of *Drosophila melanogaster* during flight. **A** Two antagonistic asynchronous power muscles are responsible for the down (dorsolongitudinal muscle, DLM) and upstroke (dorsoventral muscle, DVM) of the wing. **B** Small synchronous steering muscles are changing the trajectory of the wing movement to allow flight maneuvers. Some muscles do this by changing their stiffness in response to different neuronal input (Dickinson, 2006).

Drosophila melanogaster has two types of flight muscles. One set of muscles are fast and precise but weak steering muscles, and the other set consists of strong power muscles. The steering muscles are synchronous direct muscles and contract synchronously, whenever the innervating MN is firing an AP. To be able to contract synchronously with every MN AP they cycle Ca^{2+} between every contraction from the sarcoplasmic reticulum (SR) into the muscle lumen and back. This energy demanding Ca^{2+} cycling (consumes ~30% of ATP produced in muscle (Szentesi et al., 2001)) is also the time limiting factor for the contraction frequency. Consequently, in fast

contracting flight steering muscles power generating myofibrils have been sacrificed for SR to accelerate the Ca^{2+} cycling. These fast muscles are directly linked to the base of the wing and can alternate the wingbeat trajectory for steering (Fig. 3B). The steering muscles are in turn divided into phasic and tonic muscles. Phasic muscles are responsible for rapid maneuvers like body saccades, while tonic muscles are comparable to springs which influence wing posture and thus the general direction of flight (Lindsay et al., 2017). This direction is given by the integration of visual and olfactory stimuli. In general flies try to aim for distinct landmarks like a dot on an artificial horizon in an experimental setup. But these steering muscles are not capable of moving the wings up and down for the actual wingbeats. For this purpose, an asynchronous indirect flight muscle (AIFM) evolved.

1.6 Asynchronous indirect flight muscle

AIFMs are capable of high contraction frequencies to maintain a high power output for the wingbeat. In this type of muscle the MN firing does not cause an immediate contraction as in synchronous muscles, but is priming the muscle for contraction and puts it in a stretch activatable state (Ca^{2+} switching hypothesis) (Pringle, 1949). In this state a mechanical stretch is sufficient to trigger the contraction. The power muscle consists of two antagonistic muscles, the dorsolongitudinal muscle (DLM), responsible for the downstroke (Fig. 3A) and the dorsoventral muscle (DVM), responsible for the upstroke (Fig. 3A). They are indirectly moving the wing by the deformation of the thorax cuticle, hence the name indirect muscle. It is not clear which muscle it is, but one of the synchronous muscles should kickstart the system by stretching one of the power muscles. In the stretch activatable state, the following contraction is stretching the antagonistic muscle which is contracting again and is consequently forming an oscillating system. Depending on the stiffness of the thoracic shell, which can be adjusted by synchronous muscles and MN firing frequency, the muscles oscillate at ~200Hz and the contractions are indirectly transmitted to the wingbeat via the deformation of the thoracic shell. To control or even decouple the force transduction from the thoracic oscillation to the wingbeat a complex wing hinge evolved, which can be manipulated by fast steering muscles (Deora et al., 2017). The MNs are firing at ~2.5% of the wingbeat frequency with ~5Hz and control the power output by varying their firing frequency (Gordon & Dickinson, 2006). An increase in the MN firing

frequency results in a higher myoplasmic Ca^{2+} concentration, opening more myosin binding sites and allowing more actin myosin crossbridges. The following elevated isometric stiffness then increases the contraction frequency (Wang et al., 2011). In synchronous muscles, power output is regulated by differential recruitment of motor units, especially in large muscles and by MN firing frequency, which is referred to as rate coding (Enoka & Duchateau, 2017). Here, Ca^{2+} released from the SR into the muscle lumen after the arrival of the MN AP is actively pumped back in the SR via the sarco/endoplasmic reticulum Ca^{2+}-ATPase (SERCA). The reuptake of Ca^{2+} is terminating the contraction cycle. In rattle snake, toadfish, or the steering muscle b1 in *Drosophila,* synchronous muscles can achieve contraction frequencies >100 Hz and the cicada *Okanagana vanduzeei* even >500 Hz (Josephson et al., 2000). At high contraction frequencies the high Ca^{2+} cycling rate is energy demanding, requiring a high number of mitochondria for the ATP synthesis fueling the SERCAs. Additionally, a high volume of SR is necessary for a fast reuptake of Ca^{2+}. This constrains the space for the muscle fibrils which mediate the actual force production. Therefore, synchronous muscles achieve high contraction frequencies at the cost of force.

Asynchronous muscles circumvent this limitation by allowing very slow changes in myoplasmic Ca^{2+} level. Therefore, less SR and mitochondria are required for calcium uptake. But there are still large numbers of mitochondria sufficient for ATP production to fuel the cross bridge cycling, and evidence suggests that high numbers of mitochondria correlate with sustained power generation (Rome & Lindstedt, 1998). In AIFMs the myofibrils are more abundant and thicker (Fig. 4A , Josephson et al., 2000). This is also the reason why the AIFM is sometimes called fibrillar muscle,

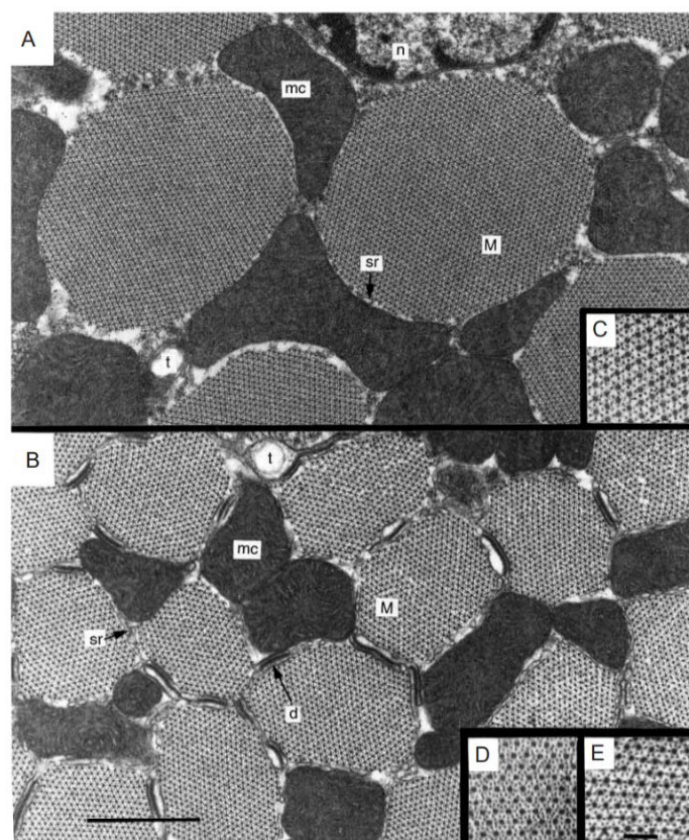**Figure 4:** Cross section of an asynchronous (**A**) and a synchronous muscle (**B**). Myofibrils (M) are thicker in comparison to myofibrils in synchronous muscle and sarcoplasmic reticulum (sr) is only sparsely distributed (Josephson et al., 2000).

as single fibers can be identified under the light microscope. Since asynchronous muscles lose the ability to be precisely activated in time with a single MN AP, asynchronous muscles are optimized for high power output at high contraction frequencies, but at the expense of high temporal resolution for changes in power output.

1.6.1 Delayed stretch activation and shortening deactivation

The force an asynchronous muscle is generating can be divided into two main components: the base tension of the muscle F_0 (Ca^{2+} tension in Fig. 5) and the stretch activated force F_{SA}. F_{SA} describes an increase in muscle tension shortly delayed after a rapid mechanical stretch of the muscle fiber (Phase 3 in Fig. 5 from Swank, 2012). These two forces vary in relative strength between species, but also between publications (Wang et al., 2011). Actually, stretch activation is present in all striated muscles, just weaker than in AIFM, and in cardiac muscle it lies in between these two (Vigoreaux, 2006). For example F_{SA} is also important for efficient locomotion in synchronous slow twitch muscle fibers in mice (Straight et al., 2019). F_0 and F_{SA} are

Ca^{2+} dependent, and in *Drosophila*, in the Ca^{2+} concentration range which is probably prevalent during flight, F_{SA} is responsible for ~80% of the force and F_0 for 20% (Wang et al., 2011). Although F_{SA} is well described in AIFM, the exact mechanism for F_{SA} is not yet completely understood. It is clear, that the increased tension through
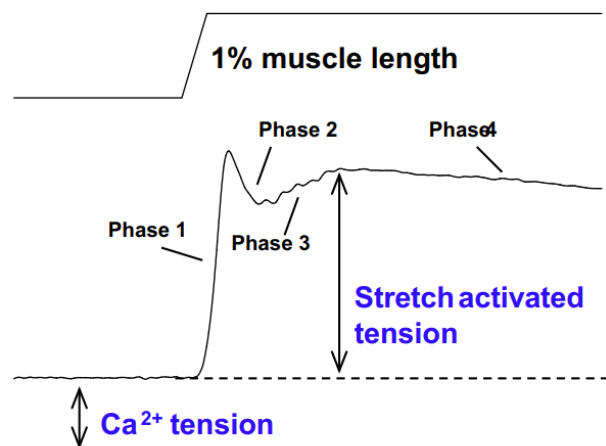
Figure 5: There are four phases of stretch activated tension in *Drosophila* AIFM after a 1% stretch in muscle length for 0.5 ms on top of a Ca^{2+} dependent tension (Swank, 2012).

stretch is caused by an increase of cross bridges to actin. There are a multitude of proposed models how this could be accomplished. For a long time, a Ca^{2+} switching hypothesis was prevalent, where it was assumed that the increased Ca^{2+} level through MN input is necessary to allow contraction, since the MN frequency is 1/40th of the wingbeat frequency and a single MN firing should have no influence on a single wingbeat. For *Drosophila* at least two additional mechanisms are proposed (Straight

et al., 2019): The expression of an embryonic myosin isoform increases F_{SA} in the jump muscle drastically, indicating a myosin-isoform-based mechanism (Zhao & Swank, 2013) and a thin filament mechanism. In *Drosophila* two Troponin C isoforms are expressed in the AIFM: DmTnC1 and DmTnC4 in the ratio 1:10 respectively. DmTnC4 is sensitive to stretch, whereas DmTnC1 is sensitive to calcium (Qiu et al., 2003).

1.6.2 Modulation of power output

The consequence of these mechanisms is a direct influence of the myoplasmic Ca^{2+} on the power output of the muscle. Power output and myoplasmic $[Ca^{2+}]$ are indeed linearly positively correlated during flight (Gordon & Dickinson, 2006). MN firing frequency correlates with stroke amplitude and stroke frequency. However, sometimes the system decreases the wingbeat frequency and compensates by an increase in stroke amplitude or *vice versa* to hold the mechanical output constant (Gordon & Dickinson, 2006). It could also be shown that power balancing during turning is achieved by different Ca^{2+} levels in the left and right DLM (F.-O. Lehmann et al., 2013). Consequently, the firing pattern of the DLM-MNs should have an influence on the steadiness of the power output. Differential recruitment of muscle fibers, as occurring in vertebrate motor units (Belanger, 2005), is not responsible for the adaptation of power output (Gordon & Dickinson, 2006).

1.7 Function of DLM-MN firing pattern

The DLM is the biggest muscle group in the fly and consists of 12 muscle fibers, 6 parallel fibers on each body side. These fibers elongate from posterior to anterior and attach directly to the cuticle in the middle of the thoracic axis and are stacked on top of each other (Fig. 6C from Ryglewski et al., 2014). The ventral most 4 fibers are each innervated by a MN, with their somata located on the ipsilateral side in the ventral nerve cord (VNC). The MNs are named by the number of the fiber they innervate MN1-4, accordingly DLM fibers 1-4 are innervated by MN1-4. The most dorsal two fibers 5 and 6 are innervated by one MN, called MN5. The soma of MN5 is located on the contralateral side in the VNC (Fig. 6A; Coggshall, 1978). MN5 is a unipolar neuron with a soma connected to a primary neurite with dendrites in the central VNC. The primary neurite extends into an axon leaving the VNC adjacent to the axons of the other MNs in the PDMN (posterior dorsal mesothoracic nerve) to the DLM (Fig. 6). On the DLM fibers the axonal branches cover the entire surface of the muscle fibers (Fig. 6D).
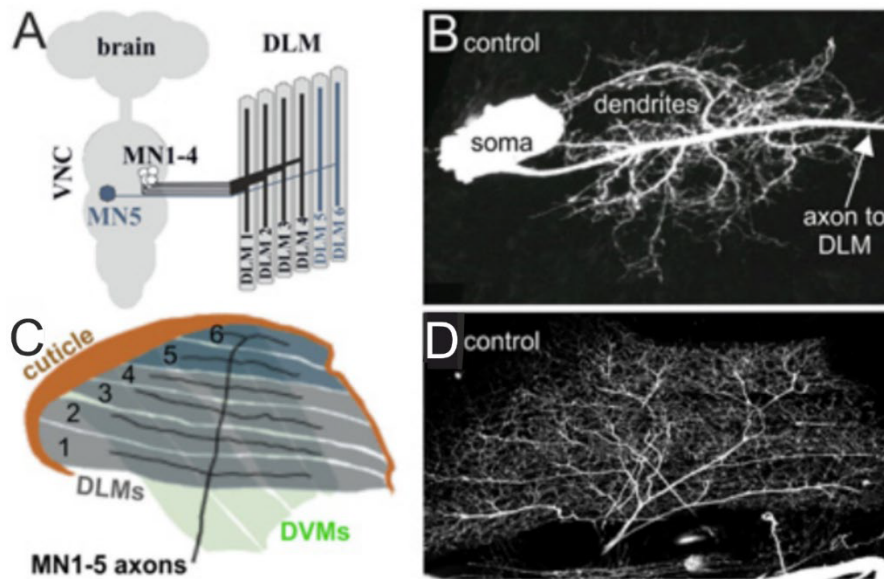
Figure 6: Morphology of DLM-MN network. **A** MN1-5 somata are located in the VNC and MN5 contralateral to MN1-4. MN1-4 innervate DLM1-4 and MN5 innervates DLM5+6. **B** Morphology of MN5 with soma connected to primary neurite with dendrites and axon leaving to DLM. **C** Schematic of cross-section of thorax with DLM1-6 and the axons of MN1-5. D Maximal projection view of confocal image stack showing axons of MN1-5 in the DLM (Ryglewski et al., 2014).

The DLM-MNs 1-5 fire at the same frequencies but splayed-out in time and fire therefore in sequence (Fig. 7). MN5 fires around 10% faster and is therefore changing its position in the sequence more frequently. MNs typically do not fire synchronously, but occasionally a synchronous spike of 2 MNs within 3 ms can occur. Moreover, no firing of one MN occurs shortly before and after (±20 ms) the firing of another MN, which we refer to as near synchronous firing. MN1+2 as well as MN3+4 have a broader time window where no concomitant firing is possible, which indicates stronger interactions. This leads to two preferred sequences 1324 and 1423 which occur around ~80% of the time (Harcombe & Wyman, 1977) for "several hundred cycles" continuously (Harcombe & Wyman, 1978). An old example of a DLM recording is shown in Fig. 7.
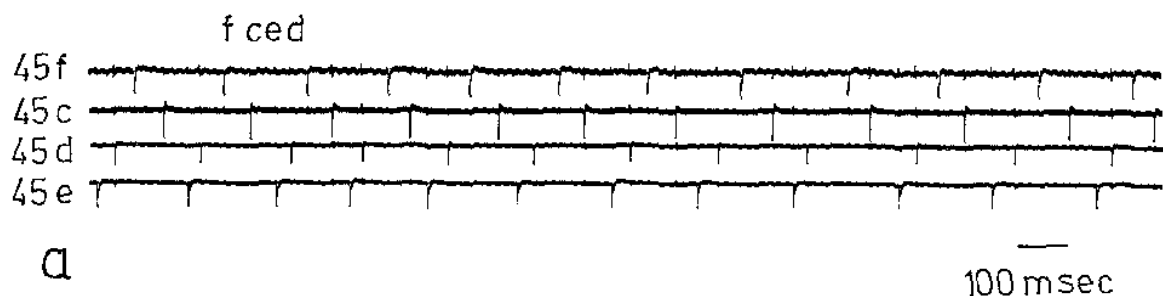
Figure 7: Electromyography of the indirect muscle fiber 1-4 or f, e, d, c respectively. The spikes are dispersed equidistantly in time and are firing at the same frequency (Harcombe and Wyman, 1977).

The MN firing pattern in a splayed-out state and the linear correlation between $[Ca^{2+}]$ and power output (Gordon & Dickinson, 2006) allows the conclusion for a smoothening effect of splayed-out firing on power output. This notion was already mentioned by Wyman in 1966:

"If all the units of a muscle were activated simultaneously then the power output of the whole muscle would decline during the period of successive activations. However, when the muscle units are activated sequentially the muscle will always contain some freshly re-excited units and some units that are relatively weak. Possibly this smoothing of the power output is the purpose of the sequential pattern of activation." (R. J. Wyman, 1966). But until now, this concept has not been proven for the function of the firing pattern.

1.8   Mechanism for generating the splayed state firing pattern

Several mechanisms are conceivable to achieve a splayed-out firing. As described previously, it is common in CPGs that interneurons shape the input of upstream neurons into a motor program which is passed on to the downstream MNs. These interneurons can be interconnected via inhibitory chemical synapses or in combination with electrical synapses (Selverston, 2010). In our case the DLM-MNs change their firing frequency simultaneously and therefore should receive a common but still unpatterned drive (Gordon & Dickinson, 2006; Harcombe & Wyman, 1977). Although it has never been shown that the input to the DLM-MNs is unpatterned, examination of the early work by Harcombe, Wyman and Ikeda lead to the working hypothesis that the MNs form a CPG network that generates the splayed-out pattern.

1.8.1 Lateral inhibition via reciprocal chemical synapses

Wyman suggested that lateral inhibition via chemical synapses is responsible for pattern formation (R. J. Wyman, 1969). He suggested that the MNs fire autorhythmically and the duration of the inter spike interval (ISI) is set by the number of inhibitions received by the other MNs. Synchronous firing within 3 ms is possible because inhibition by chemical synapses would be too slow to cancel synchronous firing.
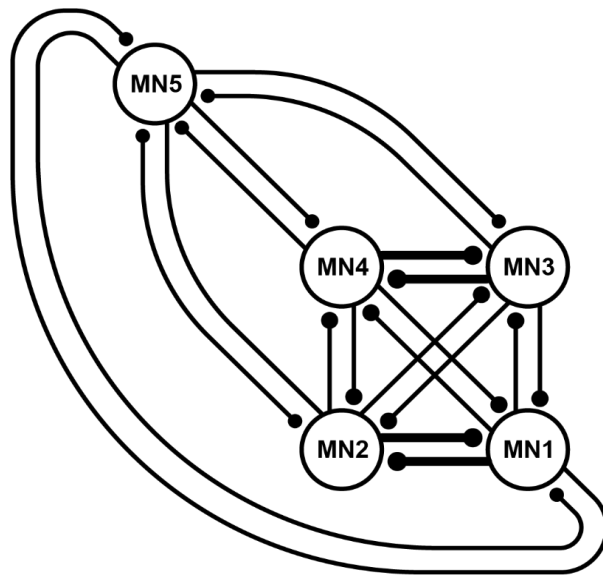
Figure 8: Model of interconnections of MNs. Thickness of lines depicts connection strength (adapted from Harcombe and Wyman 1977).

1.8.2 Candidate receptors for lateral inhibition by chemical synapses

In my master thesis, I performed preliminary experiments to test whether the lateral inhibition model via chemical synapses could be responsible for the generation of motor pattern. If glutamatergic MNs were interconnected by inhibitory chemical synapses the glutamatergic chloride channel (GluCl) could be responsible for inhibition between the MNs. I patch clamped MN5 in current clamp mode and applied glutamate onto the dendrites. The MN responded with a hyperpolarization at resting membrane potential of -70 mV and inhibition of firing during tonic firing. The response could be partially blocked with the chloride channel blocker picrotoxin (PTX). By changing the reversal potential for Cl^- with different extra- and intracellular solutions I could show that a Cl^- current is responsible for the hyperpolarizing response. Therefore, I concluded that the glutamate gated chloride channel could be a candidate for the lateral inhibition model. It is already known that the MNs express the GABA receptor Rdl (Kuehn & Duch, 2013). Consequently, it could also be possible that the MNs are able to co-release GABA for inhibition. Immunocytochemistry co-labeling of VGLUT (vesicular glutamate transporter) and VGAT (vesicular transporter for GABA) was shown for spider sensory neurons (Fabian-Fine et al., 2015). Therefore, in this thesis I tested whether Rdl GABA-A receptors and/or GluCl are required for shaping motor patterns (Fig. 18).

1.8.3 Electrical coupling via gap junctions

Koenig and Ikeda proposed that weak electrical coupling between the MNs underlies the generation of the splayed state (Koenig & Ikeda, 1980a, 1980b). They reasoned that spikes are transmitted electrotonically and that the differential coupling strength leads to the preferred sequences. Electrotonically transmitted spikes only have an effect when the postsynaptic MN is near threshold and synchronizes with the presynaptic neuron (synchronizing effect). Sometimes a delaying effect is visible, where the postsynaptic neuron is delaying the spike. For the delaying effect they also give a possible explanation: "the delay might be caused by the activation of the K^+ channels right at the AP threshold". However, at the time of their studies, they themselves admitted that there was no mechanistic understanding of how electrical synapse can delay or advance the spikes of coupled neurons, and they stated that "we do not want to go into further detail how the mechanism works, because of too many uncertainties." In summary, Koenig and Ikeda proposed that electrical coupling may underlie pattern generation, but the mechanism by which spike transmission through an electrical synapse can cause a delay of the spike in the coupled neuron remains unknown.

1.8.4 Gap junctions in invertebrates

Gap junctions (GJs) are channels connecting cells to allow direct diffusion of ions and small molecules. GJs are important for a wide variety of developmental, metabolic, and physiological functions. They are also called electrical synapses and their common key features for information transfer between neurons as described in textbooks (Purves Biologie, 2011) are:

- Information transfer is fast, because there is no neurotransmitter release over the synaptic cleft, only direct diffusion of ions through the gap junction membrane pore.
- Information transfer is bidirectional. The current flow is directed along the concentration gradient and can go into both directions of two connected cells.
- Both hyper-and depolarizations are transmitted similarly through a gap junction (non-rectifying).

- They are passive. There is no ATP consumption or conformation changes of the channel.
- There is no amplification of the signal via the synaptic machinery over the neurotransmitter release to activation of the receptor to the PSP.

But this view has been updated considerably during recent years: gap junctions can be directional as well es rectifying. They can be selective to ions, opened by mechanical stress and can also be modulated by pH, Ca^{2+} (high $[Ca^{2+}]$ leads to closing of GJs to prevent apoptosis of connected cells), $[K^+]$, or phosphorylation. Electrical synapses can also be a predecessor for chemical synapses during development or build mixed chemical-electrical synapses (Pereda, 2014).

An example of the use and dynamic properties of gap junctions in a network is the vertebrate retina, in which all five major neuron types express gap junctions (Bloomfield & Völgyi, 2009). The coupling allows the summation of synchronous activities in receptive neurons, while at the same time, it attenuates asynchronous activities. This improves the signal-to-noise ratio drastically (DeVries et al., 2002). One mechanism to regulate electrical coupling is between amacrine cells, which is controlled in an activity dependent manner by light sensitive amacrine cells, which release dopamine at higher light intensities. Dopamine binds to the D2/D4 dopamine receptor, activating the adenylate cyclase, which produces cAMP and the cAMP dependent protein kinase is phosphorylating connexins, resulting in a reduced conductance. Under starlight conditions, weaker coupling is required, so the small receptive fields have a higher sensitivity, but the signal-to-noise ratio is lower. In twilight conditions, stronger coupling leads to increased receptive fields with a lower sensitivity but higher accuracy, since the blur created by increased receptive field size is smaller than the resolution of the optics of the eye. By daylight the coupling is again decreased to prevent the spread of the excitation to far distal regions and thus decreasing the resolution (Bloomfield & Völgyi, 2009). This was just one example to illustrate the relevance of dynamic properties of gap junctions in a biological system.

The genes which encode gap junctions are called connexins in vertebrates and their invertebrate analogues are innexins (**in**vertebrate analogues of conn**exins** (Phelan et al., 1998)). Like connexin proteins, innexin proteins have 4 transmembrane domains that form one innexon and 6 or 8 innexons (depending on the isoform) create one circular innexin (6 in vertebrates). One innexin can be homo- or heteromeric, i.e., a

hemichannel consists of the same innexon protein or of different innexon proteins. If both hemichannels with the same composition form one channel, it is called a homotypic channel, and if the two hemi-channels differ in their composition, they are called heterotypic. These combinatorial possibilities allow a wide variety of channel properties.

In *Drosophila* there are 8 innexin genes on the X chromosome (Bauer et al., 2005) (Table 1). Shaking-b or ShakB is the best described GJ protein in *Drosophila*. The *shakB* gene can be transcribed into 8 possible transcripts, but only three seem to be translated into proteins (Phelan & Starich, 2001). ShakB(lethal), ShakB(neural) and ShakB(N+16) are the three isoforms. *shakB* is widely expressed in the CNS, including the giant fiber system (Ammer et al., 2022; Boerner & Godenschwege, 2010).

Table 1: Innexin genes in *Drosophila* (adapted form flybase.com).

Gene Symbol	Gene name	Synonyms
ogre	*Optic ganglion reduced*	*inx1*
inx2	*Innexin 2*	*kropf, prp33*
inx3	*Innexin 3*	*inx3*
Zpg	*Zero population growth*	*inx4*
inx5	*Innexin 5*	*inx5*
inx6	*Innexin 6*	*pas related protein, prp6*
inx7	*Innexin 7*	*pas related protein, prp7*
shakB	*Shaking B*	*as, R-9-29, shB, inx8*

In the giant fiber system ShakB(N+16) is expressed presynaptically in the giant fiber interneuron, and the isoform ShakB(L) postsynaptically in the TTMn (tergotrochanter motoneuron) or PSI (peripherally synapsing interneuron). This combination of ShakB isoforms creates heterotypic channels, which are rectifying electrical synapses when expressed in Xenopus oocytes (Phelan et al., 2008). This configuration of gap junctions could be a possible solution to produce an inhibitory mechanism, in which only the afterhyperpolarization of the action potential but not the spike overshoot is transmitted. The firing of one MN would cause a small hyperpolarization in all coupled MNs and delay the next firing. When the network fires, one MN would receive four hyperpolarization per cycle, which could generate the splayed-out firing.

1.8.5 Gap junctions in central pattern generators and MNs

Innexins are also expressed in central pattern generators (CPGs) and contribute to the motor pattern generation. This was mainly shown for the stomatogastric ganglion and the cardiac ganglion in crustaceans. Here, electrical coupling has the role of network stabilization by synchronizing activity even when synaptic inputs are fluctuating or perturbations occur (Otopalik et al., 2019).

In *Drosophila* larvae, *shakB* is expressed in aCC and RP2 MNs and connect the MNs of consecutive segments. The inhibitory, light-sensitive Cl⁻ ion pump NpHR3 can be expressed with MN driver lines and activated locally in single hemisegments. The inhibitory effect by the Cl⁻ inward current inhibits MN firing. The inhibitory effect is transferred to the following segments and is abolished by a *shakB* RNAi knockdown (BL57706) (Matsunaga et al., 2017). This shows that gap junctions by *shakB* can be used to coordinate MN firing between segments.

1.9 Computational modeling to simulate the MN circuit

We collaborated with the computational neurophysiology group of Prof. Dr. Susanne Schreiber (HU Berlin) to combine our experimental data with mathematical tools of dynamical systems theory to create a model of the DLM-MN network that can be analyzed mathematically in simulation experiments, and further refined by *in vivo* testing. A previous study had already created a Hodgkin-Huxley type model for MN5 (Berger & Crook, 2015) using experimental data from Stefanie Ryglewski and others. This model was used as a starting point. A previous study already incorporated experimental data from Stefanie Ryglewski into to the Hodgkin-Huxley model and was used as starting point (Berger & Crook, 2015). The individual MN is represented by a 3D conductance-based neuron model with a transient sodium and a delayed rectifier potassium current. Nelson Niemeyer and Jan-Hendrik Schleimer created a network by connecting multiple of these model neurons synaptically based on our physiological data. Dynamical systems theory in the context of neuroscience is used to describe and predict the behavior of neurons equipped with different cellular properties in a defined parameter space (Izhikevich, 2007). The neuron is modelled as a set of differential equations, which form a dynamical system. For simulations, these differential equations are integrated numerically. To analyze the dynamics of the model one can use different descriptive tools, such as phase portraits or phase response curves.

In a phase portrait the state of the cell is represented by the membrane voltage together with a recovery parameter (often potassium gating). The shape of the resulting trajectory provides information as to whether there are fixed points where a system is equilibrium and where it is instable. Bifurcations in the mathematical theory are points where the system is deviating strongly from the current state in response to a small parameter change. For example, when a neuron transitions from rest to AP generation through a small parameter change in the input current, this is termed the onset bifurcation. Biophysical properties influence where these bifurcation points are in parameter space. Astonishingly, for regularly spiking neurons there are only three major onset bifurcations. Based on their onset bifurcation neurons are grouped into excitability classes with distinct information transfer and synchronization properties. I want to analyze how the single neuron model behaves when the model parameters are adapted to values from the experimental data. This will allow to define the excitability class of the DLM-MNs and allows to make predictions on the behavior of the network. Parameter changes in the model can be tested experimentally, and *vice versa*, the new experimental data in turn refine the model. We hope to establish this interplay between theory and experiment for this MN network to uncover the mechanisms of motor pattern generation as well as general mechanisms for the dynamic control of the activity in neuronal networks.

1.10 Motivation of this thesis

The DLM-MN firing pattern has been well described for 50 years and multiple ideas have been developed on how this firing pattern could be generated, but it has never been resolved. In this thesis I would like to address two main questions:

- **What mechanisms are responsible for generating the splayed-out DLM-MN firing pattern?**
- **What is the function of the DLM-MN firing pattern?**

Based on these questions and the background presented above, I phrased the following hypotheses and specific predictions:

1.11 Hypotheses and specific predictions

Hypothesis:

- The CPG is comprised of a minimal network that consists only of synaptically connected MNs, with no need for interneurons for shaping the pattern.

Specific prediction:

- Manipulating the drive of the cholinergic interneurons optogenetically onto the MNs does not alter the phase relations of the MNs.

- Manipulating the drive of the MNs optogenetically does not alter the phase relations of the MNs.

Hypothesis:

- Electrical coupling between MNs is necessary for generating a splayed state firing pattern.

Specific prediction:

- Loading a dye in MN5 leads to a transfer of the dye into the other MNs.
- A RNAi knockdown of the gap junction protein ShakB perturbs the DLM-MN firing pattern.

Hypothesis:

- Lateral inhibition by chemical synapses is necessary for generating a splayed state firing pattern.

Specific prediction:

- A RNAi knockdown of the glutamatergic chloride channel or the GABAergic receptor Rdl in the DLM-MNs perturbs the DLM-MN firing pattern.

Hypothesis:

- Lateral inhibition by rectifying gap junctions is necessary for generating a splayed state firing pattern.

Specific prediction:

- Targeting single ShakB isoforms is disturbing the rectifying properties of the gap junctions and the inhibiting effect should be weaker.

- The overexpression of ShakB(N+16) increases the electrical coupling strength and synchronizes the firing pattern.

Hypothesis:

- Heterogeneous coupling between the coupled DLM-MNs leads to a preferred firing sequence.

Specific prediction:

- Using the PARIS method to measure coupling strength, will lead to stronger fluorescence changes between MN1 and MN2 or MN3 and MN4 in comparison to other MN pairs.
- Double patch clamp recordings between the DLM-MN pairs 1+2 and 3+4 will show increased coupling coefficients in comparison to all other possible MN pairs of MN1-5.

Hypothesis:

- The firing pattern in a splayed state creates an even calcium concentration across all muscle fibers and is necessary for a steady efficient flight.

Specific prediction:

- The synchronization of the firing pattern leads to fluctuations in the wingbeat frequency.

- A RNAi knockdown of the Shab potassium channel will change the excitability properties of the MNs in the HOM region and the dynamic firing range should be decreased. Therefore, the firing frequencies should change or single units could even fail to fire consistently.

2 Material and Methods

2.1 Flies

2.1.1 Fly Maintenance

Drosophila melanogaster were reared at 25°C in 60% humidity with a 12h light/dark cycle. As rearing container, a standard cornmeal-based food is filled in 68 ml transparent vials (Kisker Biotech GmbH & Co. KG, 25mm x 95mm) and closed with foam plucks. For crossing, virgin females were collected as pupae. Only male flies were used for experiments. Canton-Special (Canton-S) was used as wildtype control. Most fly lines are bought from the Bloomington Drosophila Stock Center (BDSC) or the Vienna Drosophila Resource Center (VDRC). To the DLM-MNs were selectively target by a split GAL4 driver line. This fly line was created in the Duch lab and combines the two driver lines GMR23H06 (BDSC# 49050 discontinued) and GMR30A07 (BDSC# 49512) from the Rubin Collection (Jenett et al., 2012; Bachelor thesis Silvan Hürkey). The GMR23H06 enhancer expresses the activating domain (AD) and the enhancer GMR30A07 expresses the DNA-binding domain (DBD). Only in the overlapping region of both expression patterns both domains are present and can form a functioning GAL4 protein. The overlap is mostly in the DLM-MNs. With this driver line we expressed multiple transgenes to manipulate the expression of gap junctions or inhibitory glutamate gated chloride channels as well as channelrhodopsins for optogenetic manipulation. A *shakB* RNAi knockdown (BDSC# 57706) was used to decrease the expression of all ShakB isoforms. For the knockdown of single ShakB isoforms we used the line BDSC# 27291 for ShakB(N) and BDSC# 27292 for ShakB(L) (Perkins et al., 2015). The ShakB(N+16) isoform was overexpressed with a fly line, which was kindly gifted by Pauline Phelan (University of Kent). For the knockdown of inhibitory glutamate gated chloride channels the GluClα kk RNAi line VDRC#109167 was used and combined with dcr2 (BDSC# 60533). We also used a Rdl knockdown UAS-Rdl-RNAi (VDRC#41103). As channelrhodopsin the UAS-XXL (BDSC# 58374) variant was used.

Calcium imaging was done with the DLM driver line Act88-GAL4 (BDSC# 38461, (Barthmaier & Fyrberg, 1995) and different GCaMP variants: GCaMP7s (BDSC# 80905), GCaMP7f (BDSC# 80906), GCaMP7c (BDSC# 80908) and GCaMP8f (BDSC#92588). For the dye coupling experiment the FMR1 RNAi knockdown (VDRC

110800) was used to increase the dye coupling effect (Kennedy & Broadie, 2017). Protein trap lines for GluCl (BDSC# 60533) and ShakB (BDSC# 60524) are based on the MiMIC method (Nagarkar-Jaiswal et al., 2015). *Calliphora spec, Musca domestica* and *Lucilia spec* were obtained from pet shops as feed insects and A*pis mellifera* from the local apiculture of the Johannes Gutenberg - University of Mainz.

2.1.2 Fly Stocks

See appendix.

2.2 Solutions

2.2.1 Normal Saline

128 mM NaCl, 4mM $MgCl_2$, 2 mM KCl, 1.8 mM $CaCl_2$, 35 mM sucrose and 5 mM HEPES. Adjusted to 300-310 mosmol kg^{-1} with sucrose. PH adjusted to 7.24-7.26.

2.2.2 Electrolysis solution

10.3 M $NaNO_2$ and 6.05 M KOH dissolved in double-distilled water.

2.3 TRiP CRISPR/Cas9 knock-out

To selectively knock out gap junctions in DLM-MNs we combined GAL4-mediated, tissue-specific expression of UAS-Cas9 with TRiP-CRISPR knockout for *shakB* (Kondo & Ueda, 2013; Port et al., 2014) from the Transgenic RNAi Project (TRiP, Perkins et al., 2015). The single gRNA from the targeted gene is ubiquitously expressed by the U6:3 promoter. The tissue-specific expressed Cas9 is then guided to the target coding sequence, where the gene is cleaved. The following Non-Homologous End Joining (NHEJ) is completing the somatic gene mutagenesis.

2.4 Electromyography/ extracellular recording of motoneurons

The activity of the MNs were indirectly measured by extracellular voltage recordings of their respective muscle fiber. For this, flies are fixated to a metal hook. Flies are cold anaesthetized for 20 s in a plastic vial on ice and then transferred on a cold metal plate (~3°C). The fly is positioned on their ventral side and a small plastic plate is put on their

abdomen to fixate the position. Now a metal hook can be placed in between the head and thorax. On the metal hook is a small droplet of UV-glue, which has to be hardened with a UV-light (Mega Physik Dental Cromalux-E Halogen Curing Light Unit) for 45 s. Now the fly can recover for 10 min with a small piece of Styrofoam or paper in their feet to prevent them from flying before the experiment. The rested fly can be mounted in the DLM recording setup in a clamp. The clamp is attached to a micromanipulator to ease the positioning of the fly for inserting the tungsten electrodes and measuring the wingbeat with a light barrier. The light barrier is a red laser pointed at a LED and an aperture in between. The aperture is decreasing the laser beam size to a diameter of around 1 mm. On the LED is a cover with a pin hole, where the laser beam is aimed at. This prevents other light sources to create background noise and improves the wingbeat read out. When the fly is positioned in the laser beam the tungsten electrodes can be inserted. First the reference electrode is put into the abdomen from the dorsal side in the last segment. To record MN5 and MN4 we insert the sharp tungsten wire 2 small bristles in front of the large anterior dorsocentral bristle and not crossing the midline of the thorax (Fig. 9 from Holtzman, S., Kaufman, 2013). For orientation we used the stereotaxic map of the muscle fibers from J. D. Levine & Hughes, 1973.

If we want to record all 5 units, we have to put the second electrode four small bristles in front of the first electrode, which should record MN4 and MN3. The third electrode should be inserted anterior on the same line as electrode one and two under the spot where the small bristles begin to grow on the thorax. When inserting the electrodes, we first have to break through the cuticle, which is easier by moving the tip of the electrode with slight pressure on the cuticle and then tipping on the back of the micromanipulator, until we break through. Now we should be able to see muscle spikes on the recording channel while the fly is flying. If we now carefully go deeper into the muscle with

Figure 9: Photo of the dorsal side of the thorax with an overlay of the stereotaxic map of the indirect muscle fibers from Levine and Hughes 1973. Photo from Holtzman and Kaufmann (2013).

the electrode, a second smaller muscle spike should appear. When the second unit has approximately half of the amplitude of the first unit, we have two easily
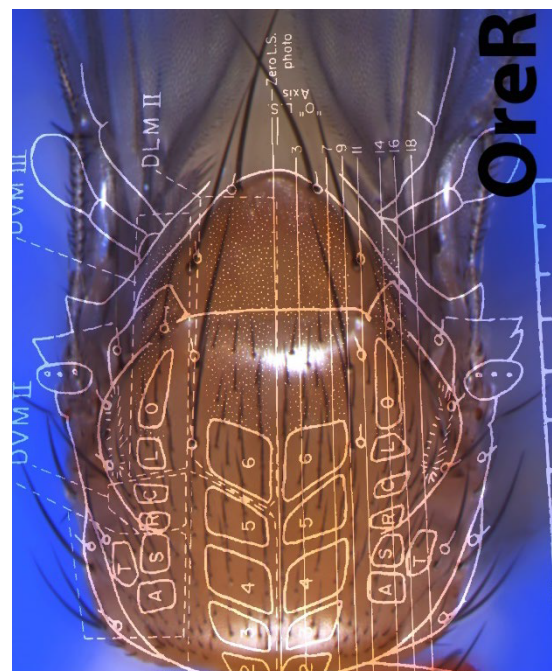
distinguishable signals. Under some circumstances it is also possible to record three units simultaneously, but spike sorting is more time intensive.

All larger insect species than *Drosophila* were cold anesthetized for up to 20 min in the fridge at 5°C and fixated in a 3D printed device to hold the insect in place. Instead of a rectangular tungsten hook, the wire is bent in a half circle and glued on the outer circumference of the posterior dorsal region of the thorax to increase the adhesive surface.

2.5 Electrolytic sharpening of tungsten electrodes

First, 1 cm of 100 μm tungsten wire (125 μm for bigger insects) is crimped onto metal pins taken from a circuit board connector. To do this, the wire is placed onto the pin and covered with a 0.5 mm ferrule. A crimping tool can now compress it to form a pluggable tungsten wire electrode. Now the tip of the wire needs to be sharpened. Therefore, the electrode is placed in an alligator clip, connected to a stimulator (Grass SD9 square pulse stimulator) and the tip is subsequently brought into the sharpening solution (10.3 M $NaNO_2$ and 6.05 M KOH in ddH_2O), which is connected to the other pole of the stimulator. A monophasic current with 120 Hz, 50 V and 1ms duration was applied. By frequently moving the tip in and out of the solution, a long, uniform thin tip is formed. After the sharpening process the electrodes are rinsed with water. A petri dish with play dough is a good repository.

2.6 Optogenetics

To increase the firing rate of the DLM-MNs themselves the UAS-Channelrhodopsin-XXL variant was driven with the split GAL4 line (GMR23H06-ADZ attP49; GMR30A07-DBD attP2) and stimulated with blue light (488 nm) from a Monochromator (Polychrome V, TILL photonics) and delivered with a fiber optic cable from the dorsal side. To increase the presynaptic drive to the DLM-MNs the channelrhodopsin was expressed in cholinergic neurons with ChaT-GAL4 (;;ChaT-GAL4). While the on kinetics are very fast within several milliseconds, the off-time kinetics of the XXL variant are very slow with 76±12 s (Dawydow et al., 2014). Consequently, the increased firing rate during flight is longer than the duration of the blue light stimulus.

2.7 *In situ* whole cell patch clamp

2-3 days old adult male *Drosophila* are cold anesthetized and then the wings and legs are removed. With the ventral side up the fly is pinned down in a 35 mm Petri dish through head and the posterior end of the abdomen. The body is submerged with normal saline. The thoracical cuticle is removed with iris scissors to expose the VNC. The preparation was placed in an upright Zeiss Axio Examiner epifluorescence microscope with a 40x water immersion lens (Zeiss W Plan Apochromat 40x NA 1.0, DIC VIS-R). With a TRITC filter the UAS-6xmCherry in the DLM-MNs is visible. With a patch pipette (tip is manually broken off) 1% protease type XIV (from *Streptomyces griseus*, Sigma Aldrich, Cat# P5147) is applied on the ganglionic sheath to loosen the tissue and remove the excess material covering the MNs. A gravitation perfusion system is washing the preparation (~ 2 ml/min, the bath volume was ~ 300 µl). Recording electrodes (borosilicate glass capillaries, o.d. 1.5 mm, i.d. 1 mm, without filament, World Precision Instruments, Cat# PG52151-4) with a tip resistance of 5 to 6 MΩ were pulled with a PC-10 vertical puller (Narishige, Japan) and filled with internal patch solution (K-gluconate 140 mM, EGTA 11 mM, HEPES 10 mM, Mg-ATP 2 mM, $MgCl_2$ 2 mM, pH 7.24, 300 mOsM/kg). Each of the two patch pipettes is connected to an Axopatch 200B amplifier (Molecular devices) connected to a digitizer (Digidata 1440). The data is filtered with a 5 kHz low pass Bessel filter and recorded with pClamp10.7 and a 10x gain. To establish a double patch recording, first a giga seal has to be formed with one cell, then pipette capacitance artifacts are canceled out and switched into whole cell configuration with a holding potential of -70 mV. When whole cell capacitance is compensated, correction and prediction values are chosen and series resistance is compensated for. To go back into the bath mode the I=0 setting is first switched on, which allows to patch the second MN. For quality control the following parameters were assured: giga seal > 5 GΩ, -70 mV membrane potential was held with a holding current smaller than ± 100 pA, series resistances > 15 MΩ were not accepted to ensure good control when applying current injections. Only if these criteria were met for both MNs, the recordings were switched to current clamp mode. Resting membrane potential was ~ -60 mV without current injection. By injecting depolarizing and hyperpolarizing current in one neuron and simultaneously monitoring the other cell, coupling strength and rectification can be characterized. With small somatic current injections, slow tonic firing (3-8 Hz, as in flight) can be evoked in one or both

cells. Input-output relationships were determined by 1000 ms square pulse current injections in 0.1 nA increments with up to 1 nA.

2.8 Intracellular dye filling

Flies with a FMRP RNAi knockdown in the DLM-MNs (*w;UAS-FMRP^RNAi^/23H06-ADZ UAS-CD4-td-GFP;30A07-DBD/+*) were used to increase dye coupling between the MNs (Kennedy & Broadie, 2017). Dye filling is done with sharp electrodes filled with 1:1 TRITC dextran 3000 lysine fixable (Invitrogen, Cat# 3308) to neurobiotin (Vector Labs, Cat# SP-1120) dissolved in 2 M KAcetate. A HS2A x 0.1xLU headstage is connected to a Axoclamp 2B amplifier (Molecular devices). As digitizer a Digidata 1440 (Molecular devices) was used and recorded with pClamp 10.4. A 2-4 day old fly was dissected (see Dissection) in a Sylgard coated lid of a 35 mm Petri dish and placed under an upright Zeiss Axio Examiner epifluorescence microscope and was viewed with a 40x water immersion lens (Zeiss W Plan Apochromat 40x NA 1.0, DIC VIS-R). The ganglionic sheath was removed with a glass electrode with a broken tip filled with 1% protease type XIV (from *Streptomyces griseus*, Sigma Aldrich, Cat# P5147) (Ryglewski & Duch, 2012). Next the sharp electrode with the dye was positioned next to the targeted cell, the offset was nulled and the electrode could be inserted. If necessary, a buzzer was used to break in the cell. In the next step the positive dye was forced out of the tip by applying a positive current of up to 1 nA for several minutes until the desired amount of fluorescence was visible in the cell. The electrode was carefully removed to not damage the cell, resulting in dye loss. The animal was fixated with 4% paraformaldehyde for 45 min. Next the fixated tissue had to be washed with PBS 6x30 min and then 6x30 min with 0.5% PBS-TritonX. It incubated overnight at 4°C in Cy3 coupled streptavidin in 0.3% PBS-TritonX. This was followed by an ascending ethanol series 50%, 70%, 90%, 100%, for 10 min each. The preparation was then mounted in methylsalicylate, topped with a high precision (170 ± 5 µm) cover slip and sealed with clear nail polish. The dye fill was then visualized with a Leica TCS SP8 confocal laser microscope with a Helium-Neon laser. Alexa 647 was excited at 633 nm and emission was detected between 650 and 680 nm with a photomultiplier tube. Images were taken with a 40x oil objective (NA 1.3) with a 1.75 digital zoom at a resolution of 1024x1024 pixels, z-step size was 1 µm.

2.9   Calcium imaging

To estimate the calcium time constant within the DLM we used genetically encoded calcium indicators. For calcium imaging, flies with different GCaMP7 versions and GCaMP8f expressed in the DLMs with the Act88 driver were used. The flies were pinned on a sylgard coated petri dish with the dorsal side up. Legs and wings were clipped with dissection scissors. The fly is placed in a fluorescence microscope with an Orca Flash 4.0 LT CMOS camera. The video feed was recorded with HoKaWo imaging software 2.10 and TOKUPIC Ver 1.0.

2.10 High speed video

High speed video of tethered flight was recorded with a Photron FASTCAM Mini UX100 and Photron FASTCAM Viewer software (PFV Version 3.6.9.0) at 5000 frames per s. As illumination two IR lights (Sygonix IR illuminator with 48 LEDs) were used but were not sufficient to record without binning and the resulting resolution loss. Later the LED arena to elicit the escape response with 4 string red LEDs was used, which delivers enough light to record without the need of binning, giving a clearer picture. The aperture should be around f/8 to give enough depth of field without losing to much light.

2.11 Dynamical systems theory

The model of the MN network was created by Nelson Niemeyer and Jan-Hendrik Schleimer of Prof. Dr. Susanne Schreiber's lab from HU Berlin. The methodical background is out of scope for this thesis, please see supplementary information Hürkey et al., 2023.

2.12 Splayness index and synchronization index

To quantify the splayness of the firing pattern of multiple neurons Nelson Niemeyer and Jan-Hendrik Schleimer calculated the splayness index. This index expresses the splayness of a network with a value between 0 and 1. 1 indicates a perfectly splayed state, whereas 0 a perfectly synchronized state.

The following section is directly from Hürkey et al., 2023.:

"All phases of all N neurons were sampled with a 1 ms time step at K time points $\tau_k = k \, ms$ for $k = 0, 1, \ldots K - 1$.

For each neuron *i* its phases were interpolated between its spikes $t_{n,i}$ as:

$$\phi_{k,i} = \frac{\tau_k - t_{n,i}}{t_{n+1,i} - t_{n,i}}, \left(t_{n,i} \leq \tau_k < t_{n+1,i}\right) \text{ for } i = 1, 2, \ldots N. \tag{1}$$

Then for each point in time, the phases were ordered such that

$$\phi_{k,l} > \phi_{k,m}(t), (l > m).$$

Phase differences were computed as

$$\psi_{k,i} = \phi_{k,i+1} - \phi_{k,i} \text{ for } i = 1, \ldots N - 1$$

and

$$\psi_{k,N} = 1 - \sum_{i=1}^{N-1} \psi_{k,i}.$$

In order to calculate the splayness, these phase differences were compared to the phase differences of the most splayed state (splay state) and to those of the least splayed state (sync state):

$$\gamma_k = \frac{\sum_{i=1}^{N} \left(\psi_{k,i} - \frac{1}{N}\right)^2}{(N-1)N^{-2} + (1 - N^{-1})^2} = \frac{N}{N-1} \sum_{i=1}^{N} \left(\psi_{k,i} - \frac{1}{N}\right)^2.$$

From this we constructed the time-averaged splayness:"

$$s = 1 - \sqrt{\frac{1}{K} \sum_k \gamma_k}.$$

The Synchronization index:

The synchronization index is used when we want to quantify the splayness of only two MNs. First the phases of two MNs are interpolated with the equation (1) and then "a classical Kuramoto order parameter was evaluated:

$$r_k = \left| \frac{1}{2} \sum_{j=1}^{2} e^{i 2\pi \phi_{k,j}} \right|.$$

The time-averaged $r = \frac{1}{K} \sum_k r_k$ measures in-phase synchronization of the neuron pair, where *K* is the number of time points." (Hürkey et al. 2023).

2.13 Software

2.13.1 Spike2

Spike2 Version 7 was used for extracting the MN firing time points of the extracellular recording of MNs and for spike sorting. The recording in the .abf file format was imported and then the waveform channels of MNs and wingbeat could be analyzed. The wingbeat time points were determined by creating an event, whenever the wingbeat waveform rises above a certain threshold. For spike sorting the wavemark function was used. By creating templates for every unit, only recognized spikes are categorized and imported into a wavemark channel, where they can be separately visualized. Synchronous spikes can be split into their original two units. Now the wavemarks can be translated into events and we receive an event channel for every MN firing activity. We can use the event channels to create phase histograms, but we can also create waveform averages of the wingbeat frequency to MN firing.

2.13.2 Python

Python scripts were created with jupyter notebook. For the import of MN firing events a script from Nelson Niemeyer (PhD student AG Schreiber) was used. Further analysis was not based on any preexisting scripts. For additional functions the Python libraries NumPy, pickle, SciPy and Matplotlib were imported. Most important functions of the python script include: Importing and displaying spikes, reading and quantify firing patterns, calculating ISIs, creating phase histograms, interval histograms, point caré plots, histogram for length of consecutive patterns, calculating correlation of MN frequency to wb frequency and calculating CV of MNs/wbs.

You can find the Python script here: 10.5281/zenodo.8316179

2.14 Statistics

Statistical analyses were conducted with GraphPad Prism Software (Version 9.2.0). The Shapiro-Wilk test was used to test datasets for normal distribution. Students t-test was used to test for normal distribution between two experimental groups. For more than two groups one way ANOVA with Tukey multi post hoc comparisons between groups was used. For not normally distributed data, testing between two groups was done with Mann-Whitney U Test and for multiple comparisons, Kruskal Wallis ANOVA with Dunns multiple post hoc comparison test was used. For relevant datasets mean and standard deviation (SD) or standard error of the mean (SEM) are shown. Significance levels were * $p<0.05$; ** $p<0.01$; *** $p<0.001$.

3   Results

3.1   The firing pattern of the DLM-MNs is in a splayed state during flight

As a first step toward addressing the mechanisms for pattern generation, I characterized the patterned output of the five MNs (MN1-5) to the dorsal longitudinal wing depressor muscle (DLM) during flight. I used the electromyography method to record the timing of MN spikes indirectly via the muscle fiber responses to MN activity. The DLM consists of six muscle fibers, which are innervated by 5 MNs, where fibers 1 to 4 are each innervated by one MN: MN1 to 4 innervate DLM1-4, and MN5 innervates fiber 5 and 6 (Fig. 10A). By placing fine tungsten electrodes into the muscle fibers, the postsynaptic electrical muscle fiber responses to MN spikes are recorded, and therefore, recordings of all fibers reveal the MN firing pattern (Fig. 10A top traces). During flight, all five MNs fire at the same average frequency within each animal, typically ranging from 4 to 8 Hz (Fig. 10B), with an inter animal average of around 5 Hz (Appendix, Fig. 52, mean MN5 frequency = 4.9 Hz and MN4 frequency = 4.7 Hz, n=41). The average firing frequency of a MN for 100 animals correlates with a wingbeat frequency increase (Fig. 10C). However, the MNs do not fire simultaneously but time shifted. They change their firing frequency simultaneously while maintaining the greatest possible distance in time to each other and consequently fire in sequence. MN1-4 fire preferably in the pattern 1423 (Fig. 10D, dark blue circles). A quantification of the patterns follows later in chapter 3.8 "The *shakB* knockdown decreases firing pattern stability".

A CPG output during flight recorded from the DLM target muscle fibers

B common MN firing rate

C MN versus WB rate

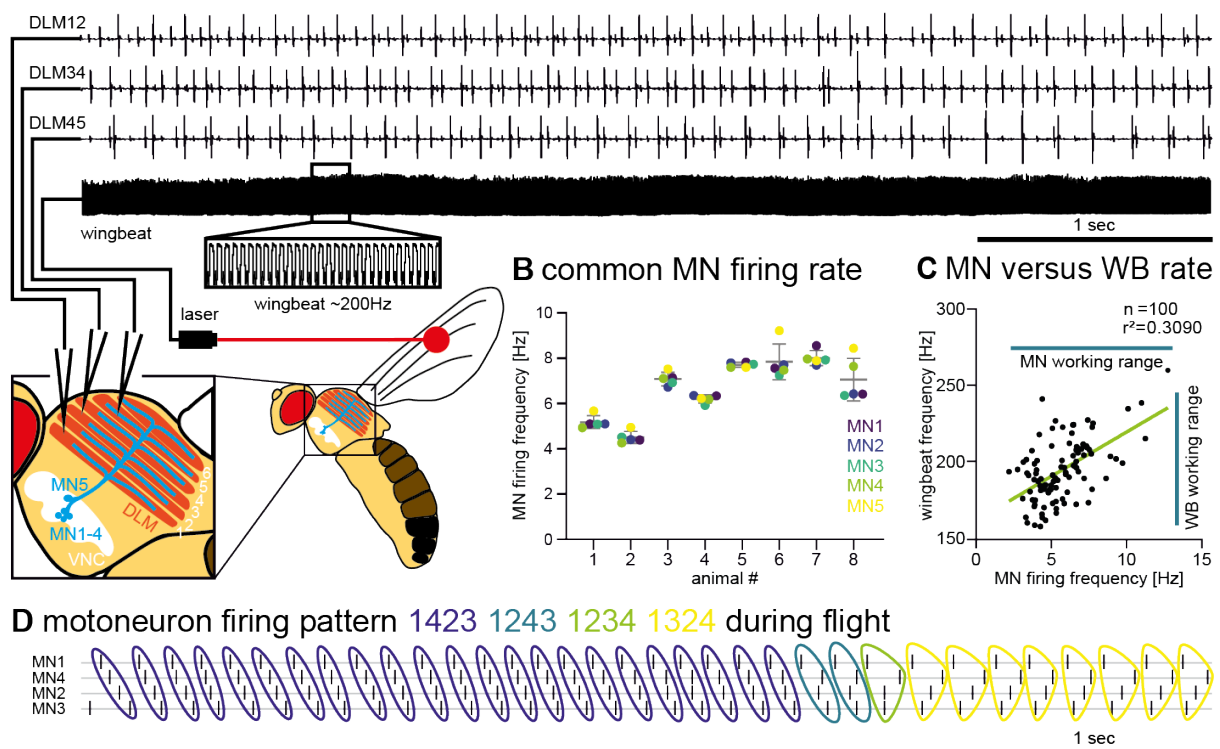**D** motoneuron firing pattern 1423 1243 1234 1324 during flight

Figure 10: The 5 DLM-MNs fire in a splayed state at equal frequencies controlling the wingbeat frequency.
A Three tungsten electrodes are inserted into the six muscle fibers recording the MN firing activity extracellularly. Two MN units per electrode are discernible and are splayed-out in time. Simultaneous wingbeat recording with a laser barrier shows a waveform oscillating at ~200 Hz representing the single wingbeats. **B** Eight animals average MN firing frequency of all five MNs are similar per animal. **C** Over 100 animals the average firing frequency of MN5 to the wingbeat frequency is positively correlated. **D** When the spikes from A are sorted to their corresponding MN we receive a firing pattern, where MN1-4 preferably fire in the pattern 1423 encircled in dark blue and is transitioning in the pattern 1243, 1234 and 1324 (Adapted from Hürkey et al., 2023).

Phase histograms quantify the firing relations of the MNs to each other. These demonstrate when a MN fires in the interspike interval of another MN. In a representative example of a wildtype fly (CantonS), the phase histogram of MN1 and MN2 (Fig.11A) shows that both MNs fire mostly out of phase. MN1 does barely fire in the first or in the last quarter of the interspike interval of MN2, but MN1 firing peaks occur at phases -0.4 and 0.5, thus it fires not synchronously but preferentially in antiphase. Although very few synchronous spikes occur (~0.1% of the spikes), no near synchronous spiking is found as demonstrated by the absence of MN2 firing from phases ~0.2 to 0.3 (Fig. 11A). This phenomenon of no near synchronous firing is apparent in the phase histograms of all combinations of MN pairs (Fig. 11), though to different degrees. This lack of near synchronous firing has previously been reported by R. J. Wyman, 1969 and termed "exclusion band". The broadest exclusion bands are observed between MN1 and MN2 (Fig. 11A) as well as MN3 and MN4 (Fig. 11H).

The narrowest exclusion bands are seen between MN1 and MN5 (Fig. 11D) as well as between MN2 and MN5 (Fig. 11G). In the case of MN1 to MN3 (Fig. 11B), the exclusion band of MN1 is narrower just before spiking of MN3 than shortly after. This effect can also be seen in the phase histogram of MN1 to MN5 (Fig. 11D). Despite the exclusion bands showing an inhibition of near synchronous firing in all MN pairs, some synchronous firing is observed at phase 0 (both spikes occurring simultaneously within 1 hundredth of the interspike interval) in most pairs. The proportion of synchronous firing ranges from 0.1% (MN1 and MN2) to 3% and has no higher probability than the other phases outside the exclusion bands. These phase histograms allow to estimate the strength of firing inhibition between different MN pairs. MN1+2 and MN3+4 have the strongest interactions considering the size of the exclusion bands. The farther apart the MNs are in respect to their muscle fiber, the smaller the exclusion bands become. Accordingly, the weakest interactions are found between MN1 and MN5. These data are consistent with an earlier report (Harcombe and Wyman, 1977), which proposed a schematic model of differential inhibitory interactions of MN pairs in which all MNs are interconnected, and the inhibition strength is represented by the thickness of the connections (see Fig. 8).
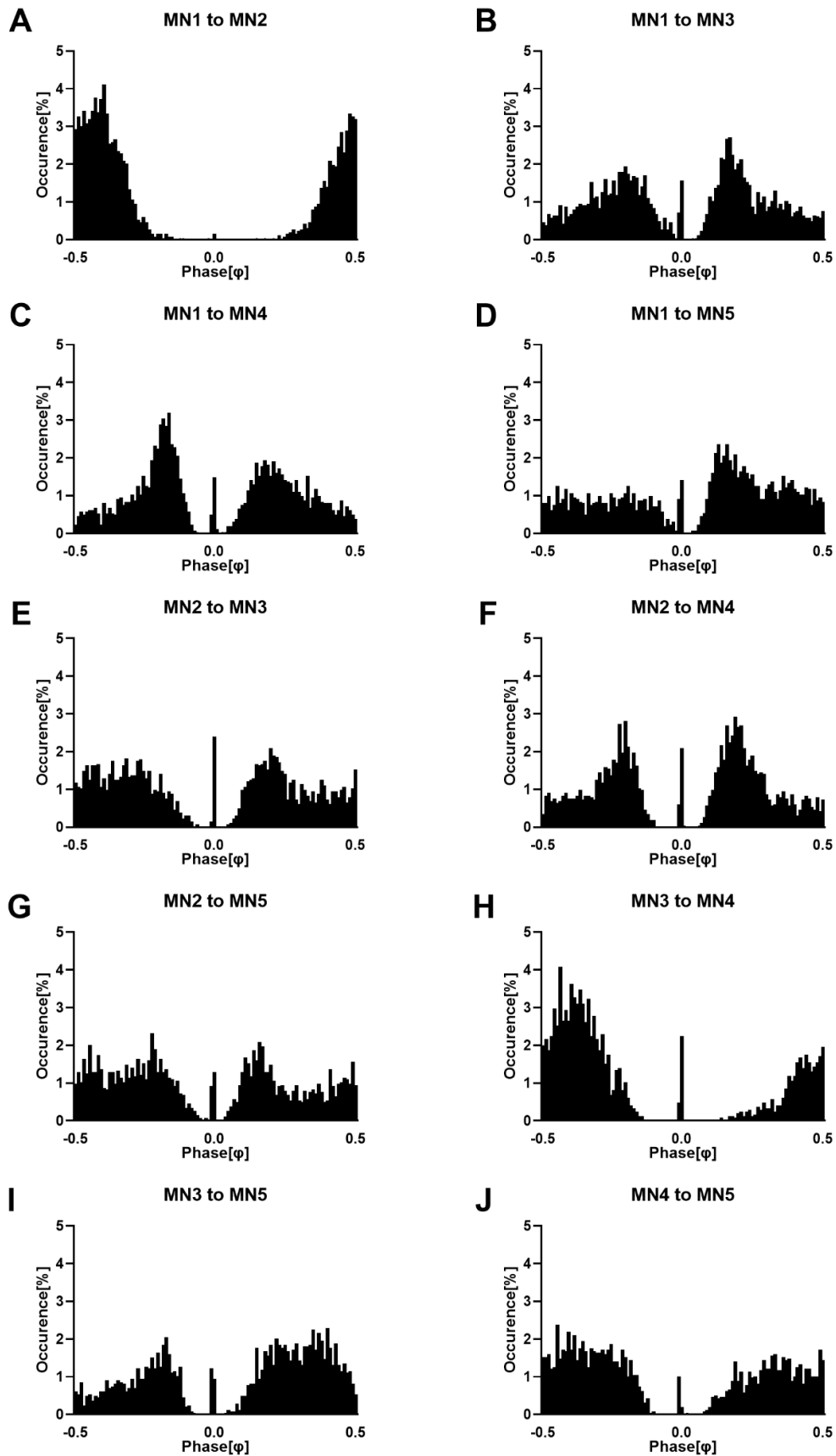
Figure 11: Representative phase histograms of all combinations of MN1 to MN5. The firing pattern of 10 min flight of a CantonS animal is used. In such a phase histogram around 3000 spikes per MN are recorded and sorted into !/100th of the ISI of another MN. All phase histograms show no near synchronous firing around phase 0. The widest exclusion bands of no firing are seen in the phase histogram of MN1 to MN2 (**A**) and of MN3 to MN4 (**H**). The smallest exclusion bands are seen between MN1 to MN3 (**B**) and MN1 to MN5 (**D**), here there is no firing after phase 0 but some directly before.

There are multiple ways to depict phase histograms, here we chose to display the synchronous spikes in the middle of the histogram for a more intuitive understanding. Commonly the x-axis in phase histograms starts with the phase 0 and ends with 1, consequently the synchronous spikes are in the first and last bin at 0 and 1. But both phase histogram forms can be transformed from one form to another (phase 0 to 0.5 also corresponds to phase 0 to 0.5, but phase 0.5 to 1 corresponds to -0.5 to 0). For comparison the phase histograms of MN1 to MN4 of Fig. 11C and Fig. 13C are combined in Fig. 12, exclusion bands are seen shortly before and after phase 0 (Fig. 12A) and shortly after 0 and before 1 (Fig. 12B). A phase histogram can also reflect how stable the firing relation between two MNs is. When the phase histogram depicts only spikes during 60 s of stable firing in pattern 1423, the distribution is narrower from phase 0.6 to 0.8 (Fig. 12C) as compared to spikes occurring during a 60 s period, where the sequence is changing frequently (Fig. 12D). There are no synchronous spikes when it is firing in the pattern 1423 (Fig. 12C).
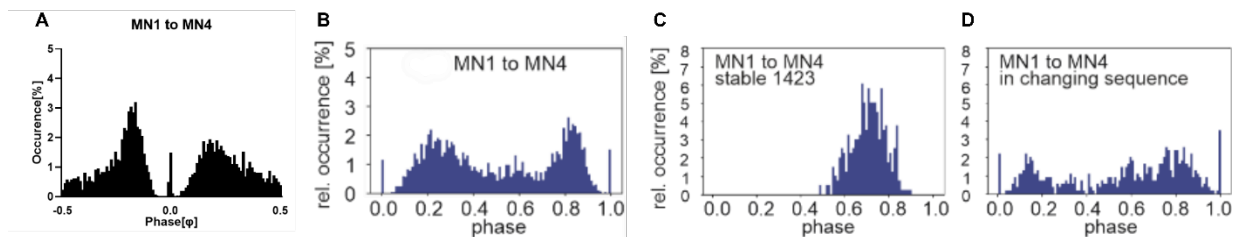

Figure 12: Phase histograms of the same MN pair MN1 and MN4 with different x-axis and stable and instable pattern. **A** Phase histogram with the synchronous spikes at phase 0. **B** Phase histogram with the synchronous spikes at phase 0 and 1. **C** Phase histogram of MN1 to MN4 where the network is firing stably in the pattern 1423 for 60 sec. **D** Phase histogram of MN1 to MN4 where the network is changing sequences for 60 sec.

When we compare phase histograms from three different animals, they show the same spike distribution for the different MN combinations as described previously with the synchronous spikes in the middle at phase 0 of the phase histograms (Fig. 13ABC). Since the MNs fire stable in the pattern 1423, the phase histograms of different MN combinations show a narrower distribution (1st, 3rd and 5th panel in Fig. 13D) compared to periods when they frequently change their firing pattern (2nd, 4th and 6th panel in Fig. 13D).
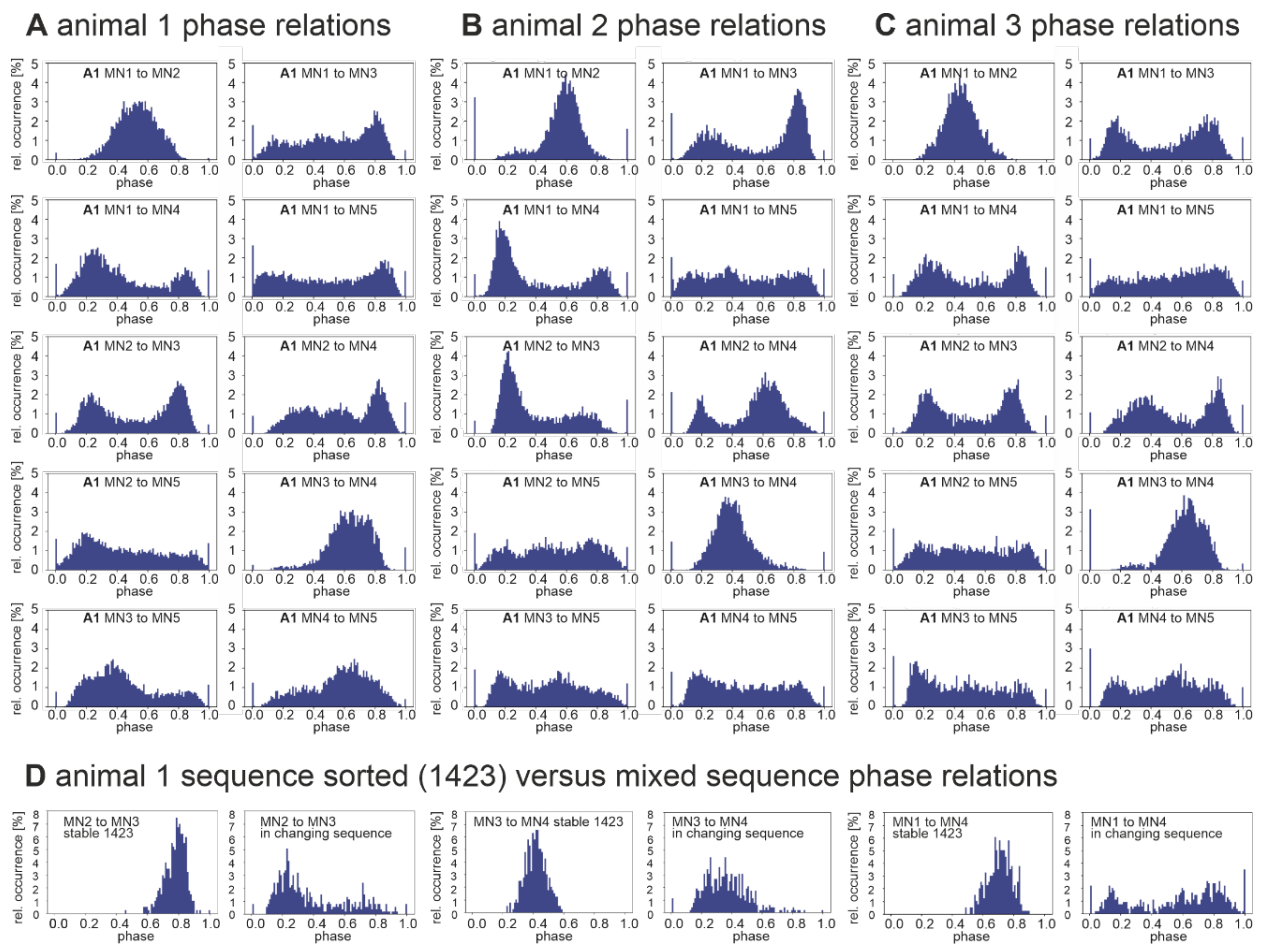
A animal 1 phase relations **B** animal 2 phase relations **C** animal 3 phase relations

D animal 1 sequence sorted (1423) versus mixed sequence phase relations

Figure 13: A-C Phase histograms of all MN combinations have equal distributions between three male animals. **D** Phase histograms when the network is stable in the pattern 1423 results in a narrow distribution of spikes in the phase. When the network is in a state of frequently changing patterns, spikes are distributed more broadly and also synchronous spikes occur (Hürkey et al., 2023).

3.1   Firing pattern of the power muscle of other insect species

Since we find the same spike distribution between animals, the question arises whether the firing pattern is also present in other insect species and represents a common means to control the power output of asynchronous muscles. Therefore, we recorded the DLM activity during tethered flight in multiple insect species of the Diptera order: *Drosophila hydei*, *Musca domestica* and the blow fly *Lucilia spec* and *Calliphora spec*., but also, *Apis mellifera* from the order Hymenoptera. In *Lucilica spec.* all units were recorded, and the phase histograms look like the phase histograms of *Drosophila melanogaster* (Fig. 14B). For the other species it was only possible to record MN4/5 and these phase histograms show the same distribution of MN5 firing around MN4 firing (Fig. 14C). For *Apis mellifera* there is no firing of MN5 shortly before synchronous firing of MN4 (Fig. 14C, bottom), but otherwise the MN4/5 phase histogram is reminiscent of those measured in several dipteran species.
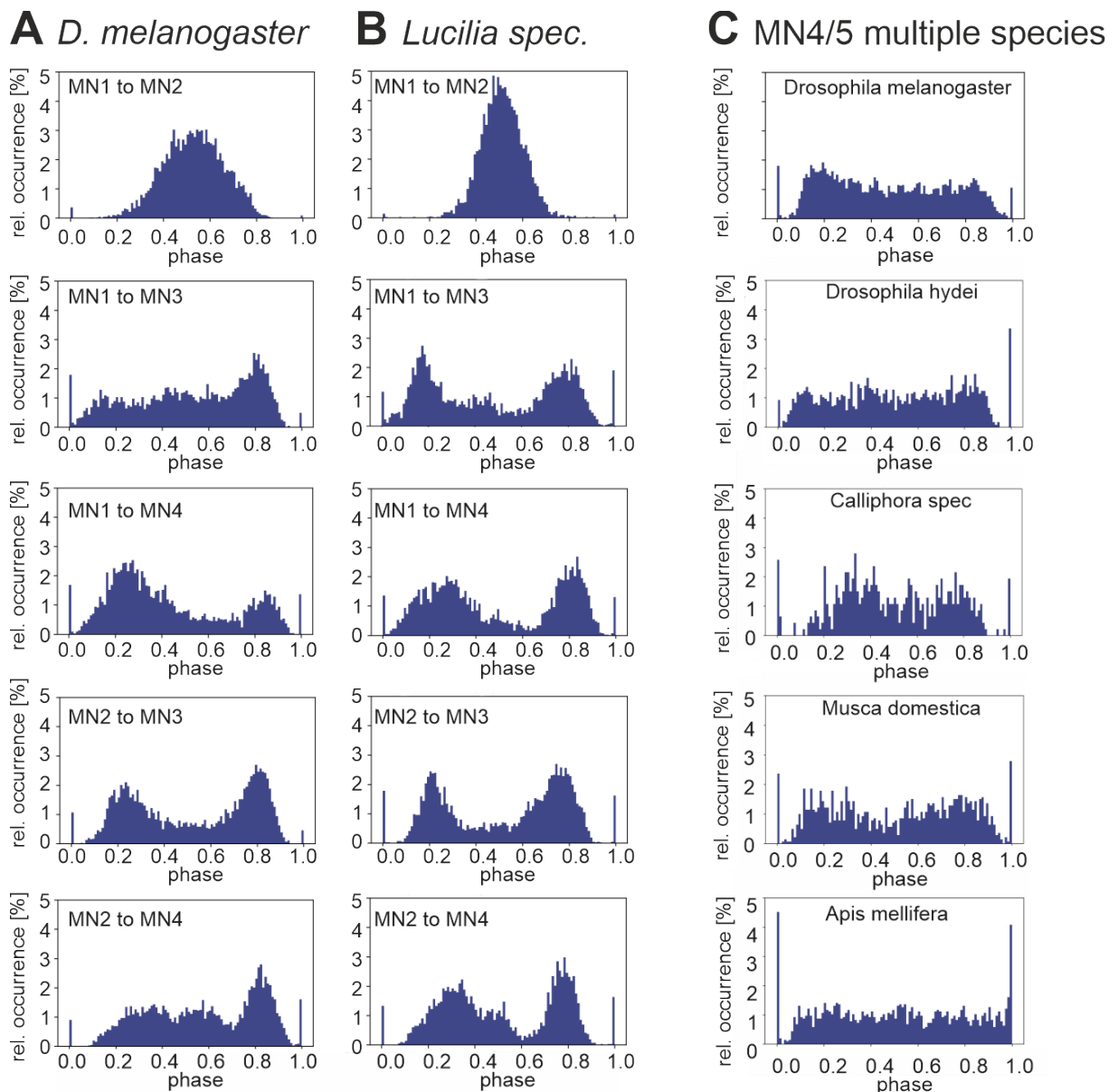
43

Figure 14: Phase histograms of different MN pairs of different insect species during tethered flight. **A** Typical phase histograms of *Drosophila melanogaster*. **B** Multiple phase histograms of *Lucilia spec*. **C** Phase histograms of MN4/5 of *Drosophila melanogaster*, *Drosophila hydei*, *Calliphora spec*, *Musca domestica* und *Apis mellifera* show all a similar distribution of no firing of MN5 firing shortly before and after MN4, except for *Apis mellifera*, where there is firing shortly before (phase ~0.9) synchronous firing (Hürkey et al., 2023).
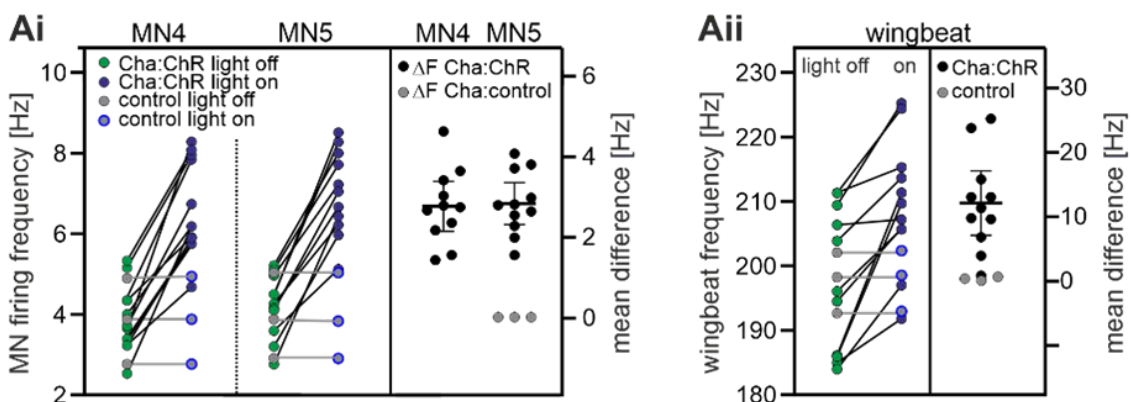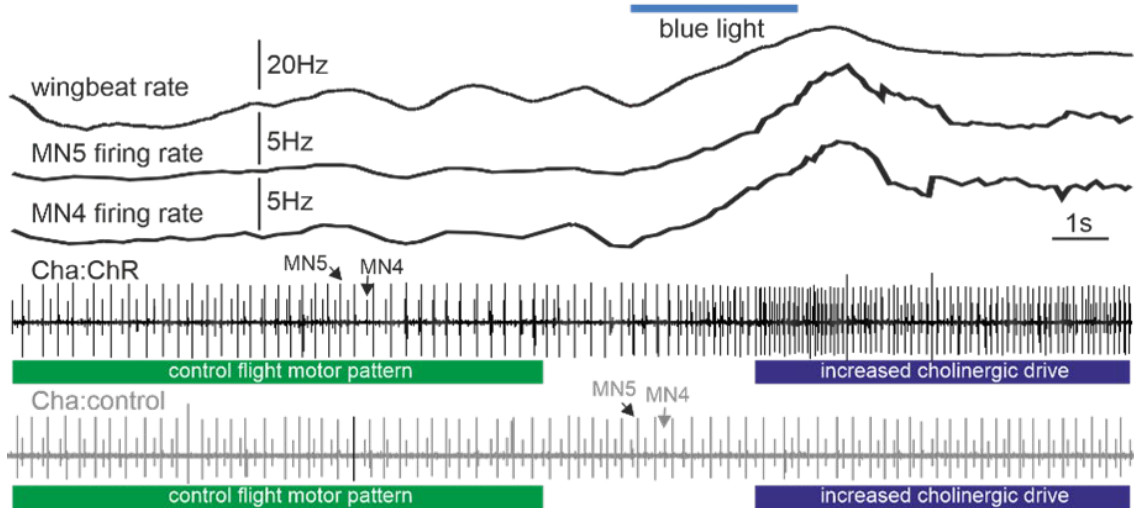
There are three possibilities for how the splayed state firing pattern could be generated. First, the MNs could receive an already patterned drive from upstream interneurons and are not directly involved. Second, the pattern is generated by the MNs themselves via reciprocal inhibitory chemical synapses. Third, instead of chemical synapses, electrical synapses between the MNs are responsible for the splayed-out firing pattern.

3.1 The motor program is generated by the MNs themselves

Motor patterns are commonly generated in CPGs, which consist of interneurons, but MNs can be involved in pattern generation. For *Drosophila* it is assumed the MNs receive the same presynaptic unpatterned drive since the MNs change their firing frequency in unison (Gordon & Dickinson, 2006; Harcombe & Wyman, 1977). But it was never directly shown that MNs generate the patterned motor output. By manipulating the presynaptic drive or the activation of the MNs themselves, one should be able to differentiate where the motor pattern is formed.

In the master thesis of Olaf Budin, which I supervised, Channelrhodopsins (ChR) were used to increase the drive generated by cholinergic interneurons to the MNs or within the MNs themselves. When the cholinergic interneurons express ChR-XXL and are activated with a blue light pulse (488 nm wavelength) the MN firing rate is elevated by 3 Hz on average (Fig. 15A, Ai). Simultaneously the wingbeat frequency is increased by 12 Hz on average (Fig. 15Aii). ChR-XXL is a variant with an increased light sensitivity and slower closing kinetics (~60 s) compared to the ChR variant. To investigate whether the firing relations and therefore the motor program is influenced by the cholinergic drive, phase histograms of MN4 and MN5 before and during stimulation can be compared. The control pattern before stimulation shows no firing shortly before and after synchronous firing in the phase histogram as we would expect (Fig. 15B, left panel). This is also the case for the phase histogram during and after stimulation with blue light (Fig. 15B, right panel). Considering that the optogenetic stimulation of the cholinergic neurons was unpatterned and ChR-XXL has an inactivation time constant of ~30 s, the input from cholinergic neurons to the MNs could not have been patterned. Therefore, the motor pattern should be generated downstream of the cholinergic interneurons.
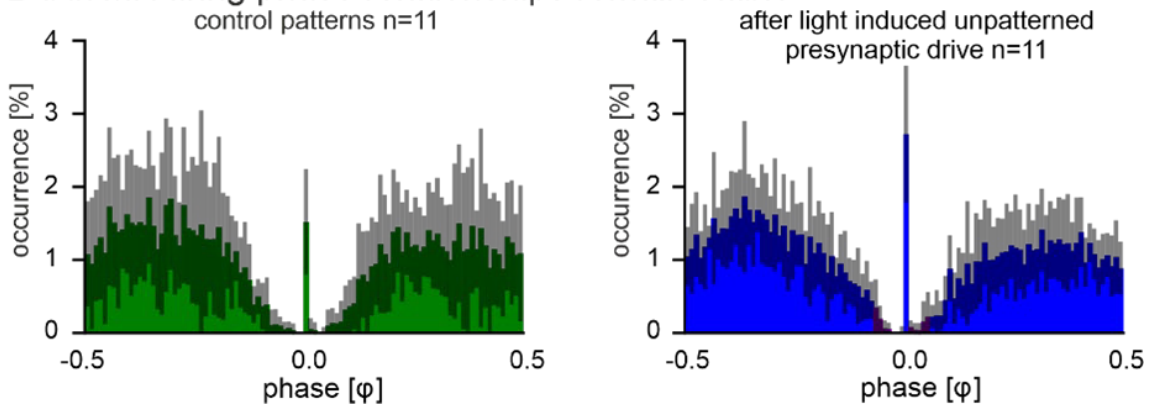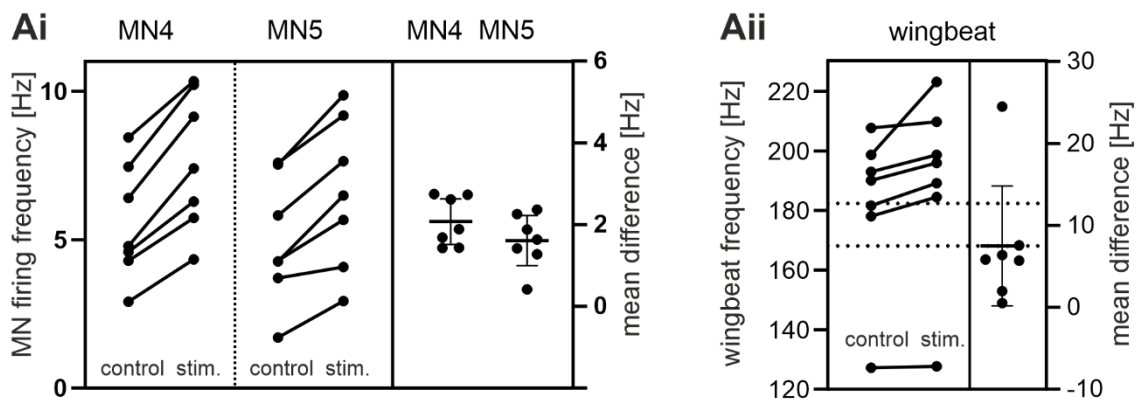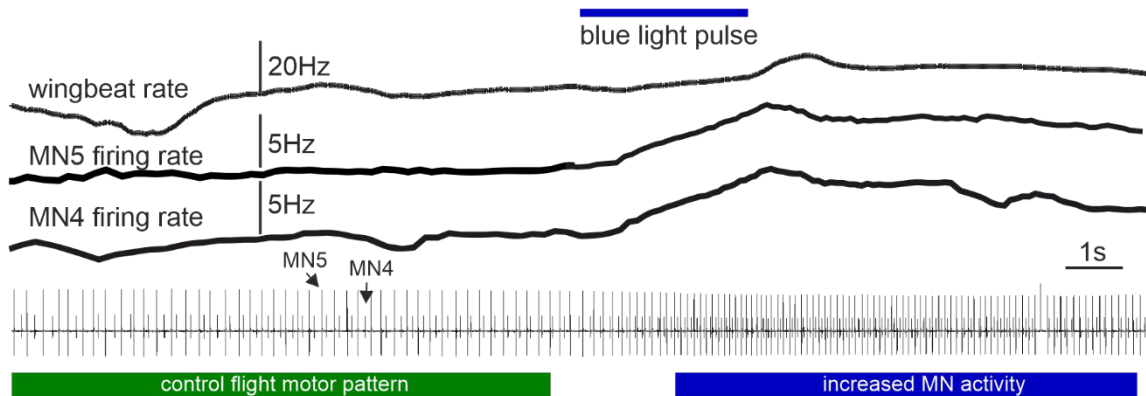
Figure 15: Optogenetic stimulation of the cholinergic interneurons increases the CPG output. A MN firing rate and wingbeat rate increase when the blue light is switched on and stays elevated, when the light is turned off (top row) in animals expressing the UAS-Channelrhodopsin XXL in cholinergic neurons. In control animals light has no influence on firing frequency (bottom row). **Ai** MN4 and MN5 increase their firing rate by 3 Hz when stimulated with light. **Aii** The wingbeat frequency is increased by 12 Hz. **B** The phase histogram as control before light stimulation shows no MN5 firing shortly before and after MN4 firing (left panel) and the phase histogram during elevated firing by light stimulation shows also no MN5 firing shortly before and after MN4 firing (Hürkey et al., 2023).

The expression of ChR-XXL in the MNs also results in an increase in MN firing rate and wingbeat rate, when stimulated with unpatterned continuous blue light. MN4 and MN5 firing rate increase by ~2 Hz (Fig. 16Ai) and the wingbeat frequency by 8 Hz (Fig.

16Aii). The phase histogram before light stimulation shows no firing shortly before and after synchronous firing, just as before and after stimulation (Fig. 16B), while firing frequency is increased (Fig. 16Ai). Consequently, the motor program is still intact even when the MNs themselves show increased activity without an increase in presynaptic drive.

A optogenetic stimulation of MNs increases CPG output

Ai

Aii

B but MN firing phase relationships remain stable
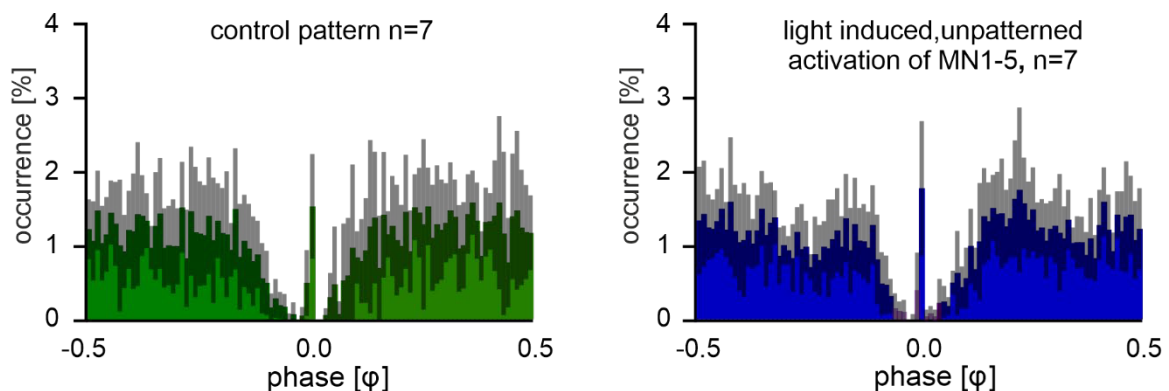
Figure 16: Optogenetic stimulation of the MNs increases the CPG output. A MN firing rate and wingbeat rate increase when the blue light is switched on and stays elevated, when the light is turned off. **Ai** MN4 and MN5 increase their firing rate by 2 Hz when stimulated. **Aii** The wingbeat frequency is increases by 8 Hz. **B** The phase histogram as control before light stimulation shows no MN5 firing shortly before and after MN4 firing (left panel) and the phase histogram during elevated firing by light stimulation shows also no MN5 firing shortly before and after MN4 firing (Hürkey et al., 2023).

47

Additionally, we checked if the MNs have output synapses in the central nervous system to other postsynaptic neurons which could be involved in pattern generation. For this trans-tango, a method to visualize synaptic partners was used (Talay et al., 2017). As a positive control to show synaptic partners a split GAL4 line for the LC4 visual neurons was crossed with the UAS-trans-tango line, resulting in a green label of the LC4 neurons (Fig. 17Ai) and a magenta label of postsynaptic partners (Fig. 17Aii). This is also true for period interneurons in the VNC with interneurons in green (Fig. 17Bi) and postsynaptic partners in magenta (Fig. 17Bii). However, when the DLM-MN split line was used, there is only labeling of the MNs and no postsynaptic labeling (Fig. 17Cii), indicating no postsynaptic partners to the MNs.

Moreover output synapses can be detected by a non-functional short Brp-protein (Brp-short), which has a strawberry tag (Fouquet et al., 2009). Brp-short localizes to the active zone in presynaptic terminals of chemical synapses. In the confocal images, MNs are stained green (Fig. 17D). Brp-short puncta in magenta are visible within the somata of the MNs, in the primary neurite (Fig. 17D), and in the axon terminals in the neuromuscular junction indicated by arrows (Fig. 17E). The Brp-short puncta are likely visible in the somata because the protein is translated there. Subsequently, the protein is transported along the primary neurite into the axon terminals, where it can also be seen. However, there are no Brp-short puncta in the dendrites, indicating no dendritic output synapses. Thus, neither method shows evidence for central output synapses of the DLM-MNs.
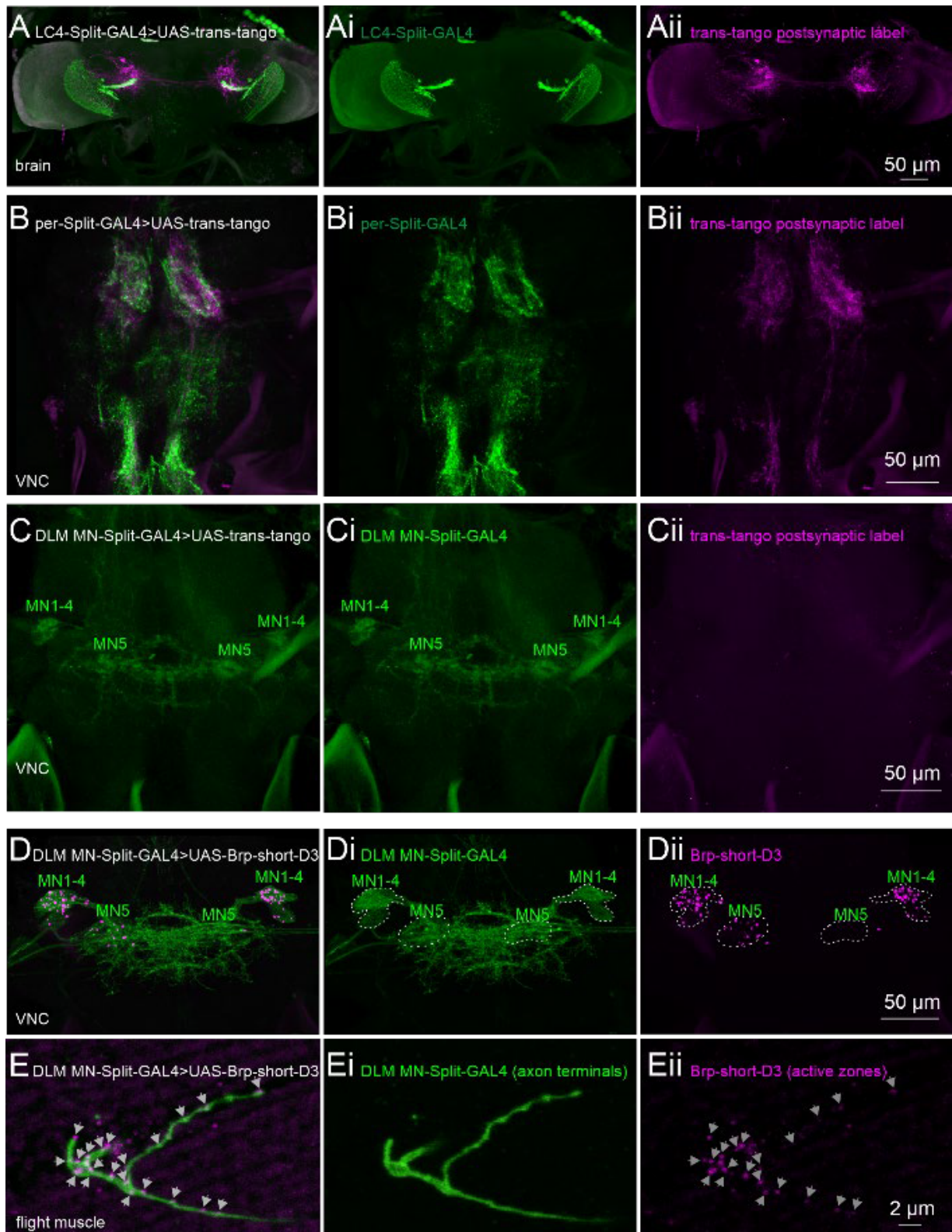
Figure 17: The DLM-MNs show no central output synapses. A LC4 neurons (green) in the optical lobe show postsynaptic partners (magenta). **B** period interneurons in the VNC (green) show postsynaptic partners (magenta). **C** The DLM-MNs (green) show no postsynaptic partners in the VNC. **D** The Brp-short (**DE** magenta) is only visible in the somata of the DLM-MNs (**D** green) and in the axonal terminals (**E** green) in the neuromuscular junction (Hürkey et al., 2023).

3.1 Lateral inhibition via chemical synapses is not responsible for the splayed-out firing pattern

The anatomical methods trans-tango and Brp-short indicate no central output synapses from the MNs, to further investigate whether chemical synapses are involved in the pattern generating process, different inhibitory receptors were targeted with RNAi. Reciprocal inhibitory chemical synapses are commonly found in central pattern generators to generate alternating activity. For glutamatergic MNs the glutamatergic chloride channel (GluCl) could be a possible candidate for mediating the inhibition (see introduction). Alternatively, the GABA receptor Rdl could be responsible if it would be assumed that MNs are also able to corelease GABA with glutamate, their native transmitter. However, the phase histograms of MN5 to MN4 with the expression of GluCl RNAi in DLM-MNs (Fig. 18B) or Rdl RNAi in DLM-MNs (Fig. 18C) show no change in the firing relation since both show no near synchronous firing. The variability just before near synchronous firing around phase -0.2 is increased in the Rdl RNAi knockdown (Fig. 18C). This increased variability just before the gap to synchronous firing could indicate that the firing of MN5 in the phase -0.5 to -0.3 of MN4 can be delayed. This should be caused by the other MNs 1-3 since they could be responsible for the inhibition before the synchronous spike.
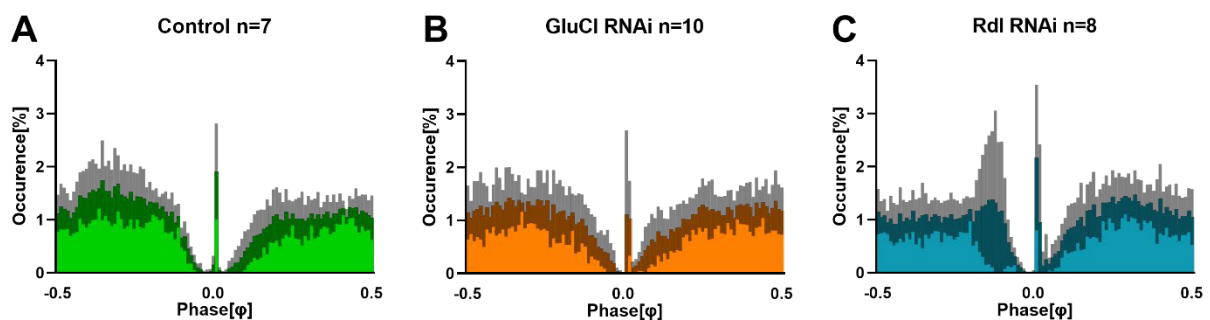
Figure 18: Phase histograms of control and RNAi knockdowns of inhibitory receptors GluCl and Rdl. SD in grey. **A** Control phase histogram with no near synchronous firing. **B** Phase histogram of GluCl RNAi knockdown with no near synchronous firing. **C** Phase histogram of Rdl RNAi knockdown with no near synchronous firing. Firing shortly before near synchronous firing at around phase -0.2 shows higher variability (Hürkey et al. 2023).

## 3.2 Electrical coupling desynchronizes the MN firing pattern

One possible explanation for the emergence of the firing pattern in a splayed state is weak electrical coupling, as proposed by Koenig and Ikeda in 1980 (Koenig & Ikeda, 1980b). To test this hypothesis, an RNAi knockdown of the ShakB gap junction protein was used, which targets all isoforms of ShakB. The RNAi construct is based on the Valium20 vector (Perkins et al., 2015) and produces short hair pin RNAs (shRNA), so no dcr2 is needed. The UAS-RNAi transgene was already shown effective in larvae (Matsunaga et al., 2017) as well as in adults (Pézier et al., 2016). MN5 and MN4 was recorded extracellularly over 10 min during tethered flight and in comparison to the control (Fig. 19Ai) a nearly inverse distribution of the MN5 spikes in the phase of MN4 for the *shakB* RNAi (Fig. 19 Bi) can be seen. The exclusion bands shortly before and after synchronous firing are absent and synchronous spikes have a higher probability (~3%) than spikes in the rest of the phase (~0.9%) (Fig. 19Bi red asterisk). Near synchronous firing is also manifested in the muscle spike recording by new spike forms of overlapping signals. In the control recordings, fully synchronous spikes, which are increasing the amplitude of the signal are rarely seen, whereas in the *shakB* knockdown spikes where the superposition of the two waveforms decreases the amplitude or is just very close to the spike of the other unit are visible (Fig. 19B, red asterisk). All phase histograms of all 10 possible combinations of MN pairs in the *shakB* knockdown of three individual animals show the synchronizing effect by near synchronous firing (Appendix, Fig. 59). Some phase histograms show less near synchronous firing like the MN pair MN1+2, while some show more near synchronous firing like the MN pair MN2+5. Consequently, the synchronizing effect is not only visible in the quantitative phase histogram of MN5+4 (Fig. 19B). The possibility that single ShakB isoforms have an effect on the firing pattern was also tested. Therefore, the available RNAi knockdowns of ShakB(N) and ShakB(L) were used. Under my supervision, Tamara Kaufmann could show in her bachelor thesis that these two knockdowns had no effect on the pattern generation, as phase histograms (Fig. 53GH), as well as wingbeat frequency and MN firing frequency were indistinguishable from the valium control (Fig. 54). For the isoform ShakB(N+16) no RNAi construct is readily available, but a UAS overexpression. When the shakB(N+16) variant is overexpressed in the DLM-MNs synchronous firing is significantly increased. It is likely that the proportion of synchronous spikes varies from 4% up to 99% of synchronous spikes depending on the strength of overexpression (Fig. 19C).

Firing pattern of MN5 and MN4

A Control
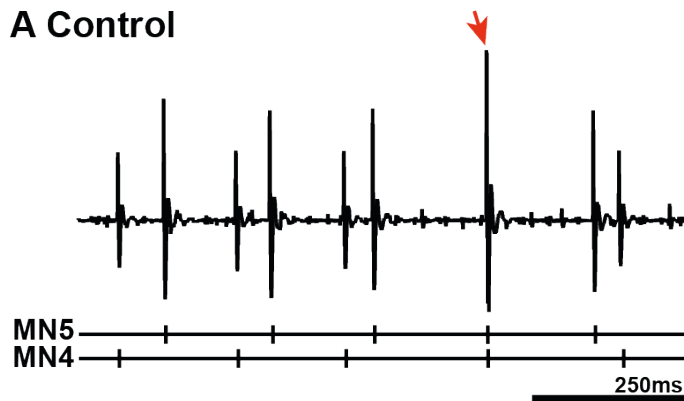
Ai   Phase histogram
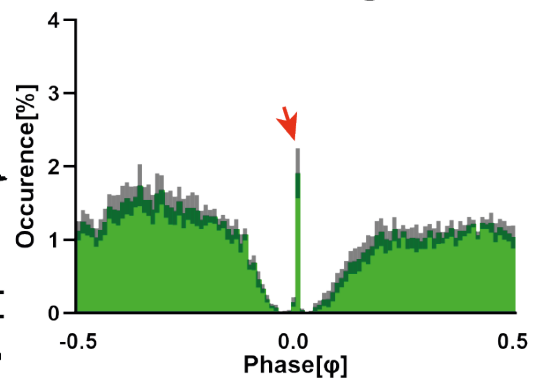
B ShakB RNAi
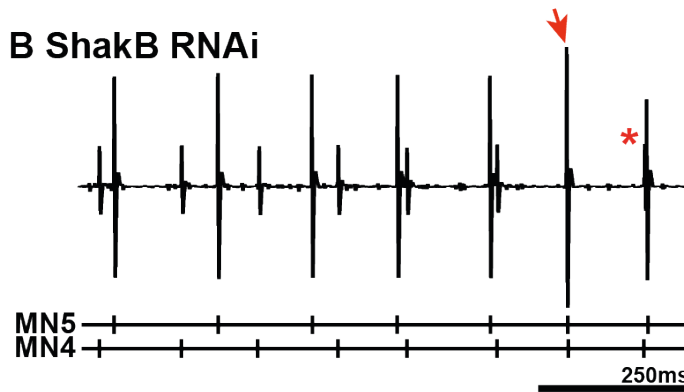
Bi   Phase histogram
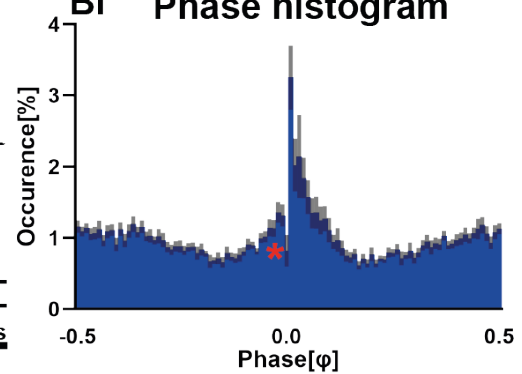
C UAS-ShakB(N+16)
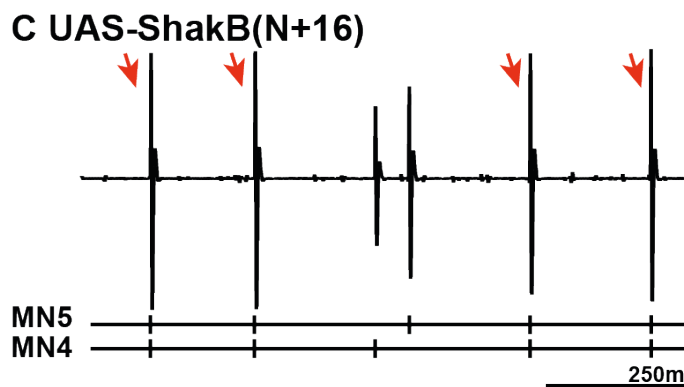
Ci   Phase histogram
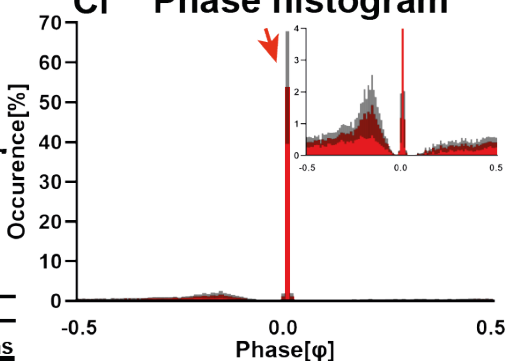
Figure 19: Firing relation of MN5 to MN4 in control, *shakB* RNAi knockdown and UAS ShakB overexpression. Synchronous firing is marked by a red arrow. **A** In a control DLM recording of MN4 and MN5, they fire not near synchronously. **Ai** The phase histogram of control animals (n=7) also shows no near synchronous firing. **B** In a *shakB* RNAi knockdown, MN5 is firing also shortly before and after MN4 (B red asterisk). **Bi** Therefore, there are no exclusion bands in the phase histogram (n=7, red asterisk). **C** In a UAS-ShakB(N+16) overexpression most spikes of MN5 and MN4 are synchronous (red arrow) but there are still no near synchronous spikes. **Ci** Most spikes in the phase histogram of the ShakB(N+16) overexpression are synchronous (n=7).

3.3 Wingbeat frequency and MN firing frequency are not affected by the genetic manipulations

Considering the change of the phase histograms, a change in overall MN firing frequency or wingbeat frequency could be expected, but this is not the case. The wingbeat frequency in control (VALIUM) and test animals (*shakB* RNAi knockdown, UAS ShakB(N+16) overexpression) is around 200 Hz and there is no significant difference (Fig. 20A). There is also no significant difference between the groups in firing frequency of MN5 or MN4 (Fig. 20BC). The ratio of wingbeats per MN5 firing is not affected (Fig. 20E), however the ratio of wingbeats per MN4 firing is affected in the *shakB* RNAi (Fig. 20F). The flies with the *shakB* RNAi knockdown have a significantly decreased ratio with ~28 wbs/MN4 firing instead of 38 wbs/MN4 firing (Fig. 20F). This is also reflected in the ratio of wingbeats to the mean of MN4 and MN5 (Fig. 20D).

If we take a further look on the distribution of the "efficiency" (wbs per MN firing) over the MN firing frequency of 100 control animals and compare it to the *shakB* RNAi animals, we can see the dots fit in the distribution (Fig. 21). The control animals in dark green are just on the upper part of the distribution and the *shakB* RNAi and overexpression on the lower part, which explains the tendency. Therefore, the animals, where *shakB* is manipulated are not more inefficient, but rather fire at a higher rate and higher rates are more inefficient.
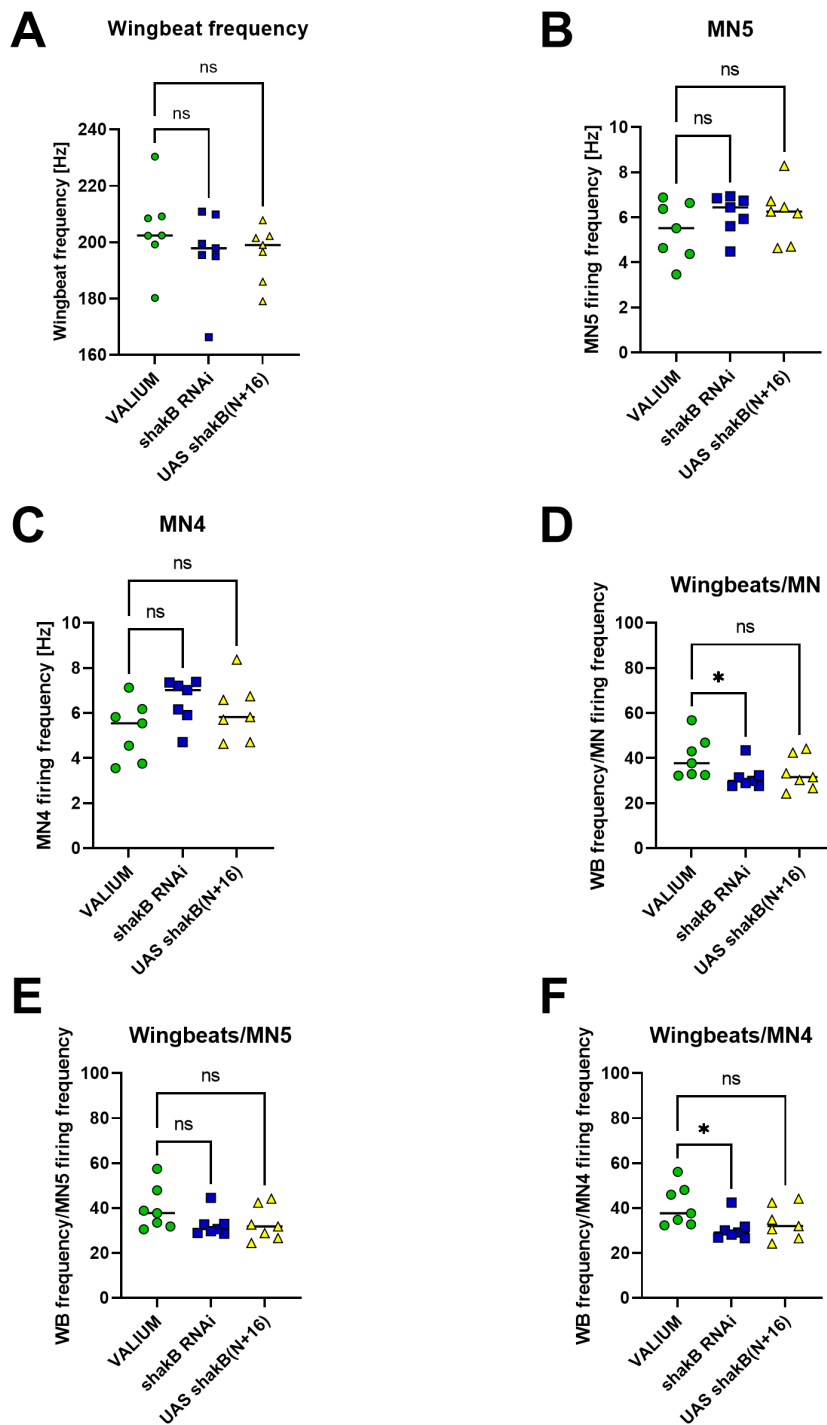
Figure 20: Scatter plots show the wingbeat frequency is around 200 Hz. **A** MN firing frequency **BC** and are unaffected by the knockdown of *shakB* as well as the overexpression of ShakB(N+16). **D** The relation of wingbeats to MN firing is significantly decreased for the *shakB* knockdown, but not for the ShakB(N+16) overexpression. **E** There is no significant difference in wingbeats per MN5 firing. **F** The ratio of wbs per MN4 firing is significantly decreased to 28 wbs/MN4 firing compared to the VALIUM control with 38 wbs/MN4 firing. N=7 for all genotypes.
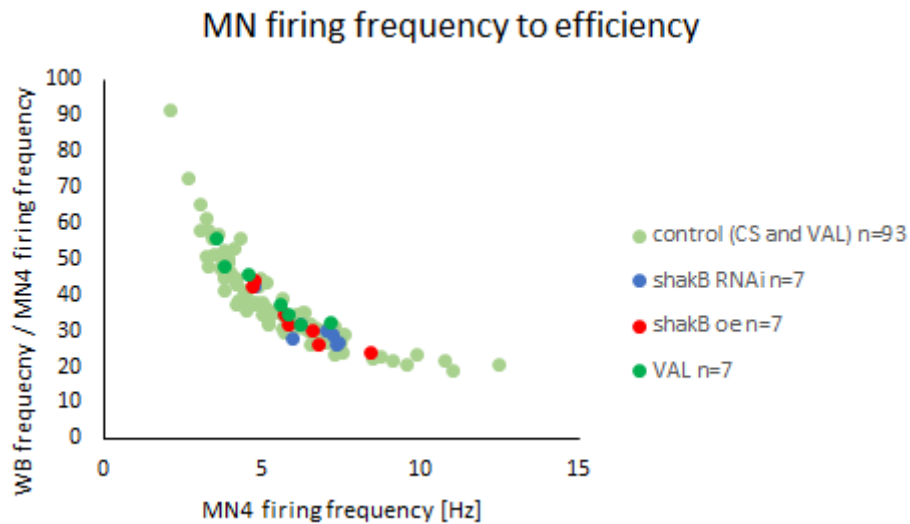
Figure 21: MN4 firing frequency to wb efficiency. With increasing MN4 firing frequency decreases the ratio of wingbeats per MN firing. The manipulations seem to have no effect, since they are visible in the distribution of the control animals (light green). The control animals in dark green are on the slower end of the firing frequency and the *shakB* RNAi (blue) and ShakB(N+16) overexpression (red) on the faster side of the MN4 firing frequency distribution.

3.4 MN firing and wingbeat frequency correlate negatively in the ShakB overexpression

In wildtype animals the MN4 and MN5 firing frequency correlates positively with the wingbeat frequency when the frequencies are averaged over 10 min of flight time. This is also true for the RNAi knockdown of *shakB* and the double knockdown of GluCl and ShakB (Fig. 22ABC). When the ShakB(N+16) isoform is overexpressed, the correlation becomes low with an r² of 0.0155 for MN5 to the wingbeat and 0.0502 for MN4 to the wingbeat (Fig. 22D).
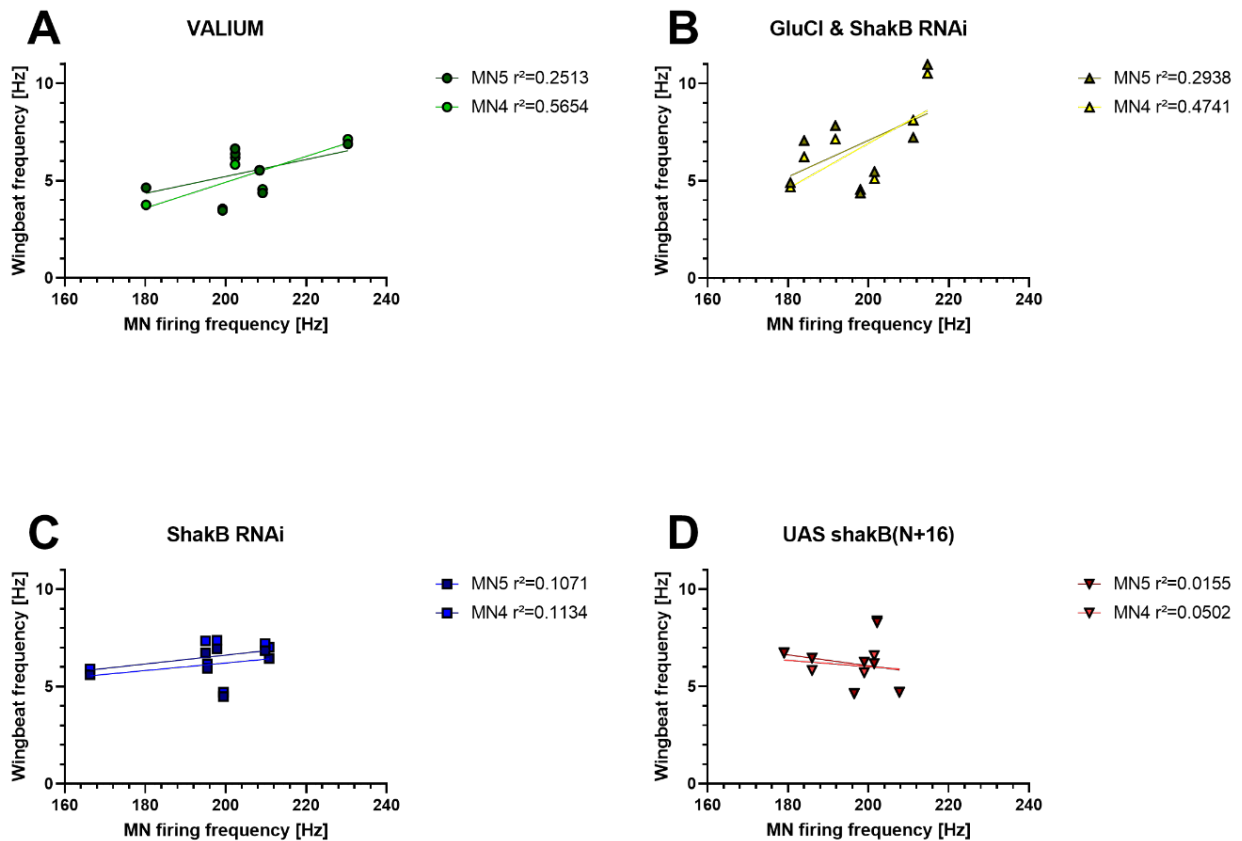
Figure 22: Correlation of MN firing frequency and wingbeat frequency. **AB** VALIUM Control and double knockdown of GluCl and ShakB show a strong positive correlation of MN firing frequency and wingbeat frequency. **C** In the *shakB* knockdown the positive correlation is weaker. **D** Overexpression of ShakB(N+16) leads to a slightly negative correlation, with a low r^2 value. MN firing frequency and wingbeat frequency are calculated over 10 min of flight for 7 animals of each genotype.

To get a better understanding of the correlation between the MN firing frequency and the wingbeat frequency we also analyzed the total firing frequency of all five MNs together in relation to the wingbeat frequency. In three VALIUM control animals the correlation is r=-0.18, 0.03 and 0.4 (Fig. 23ABC). This is similar to the values of the *shakB* knockdown, where r=-0.23, 0.17 and 0.43 (Fig. 23DEF). This shows the correlation is not as clear as one might assume.
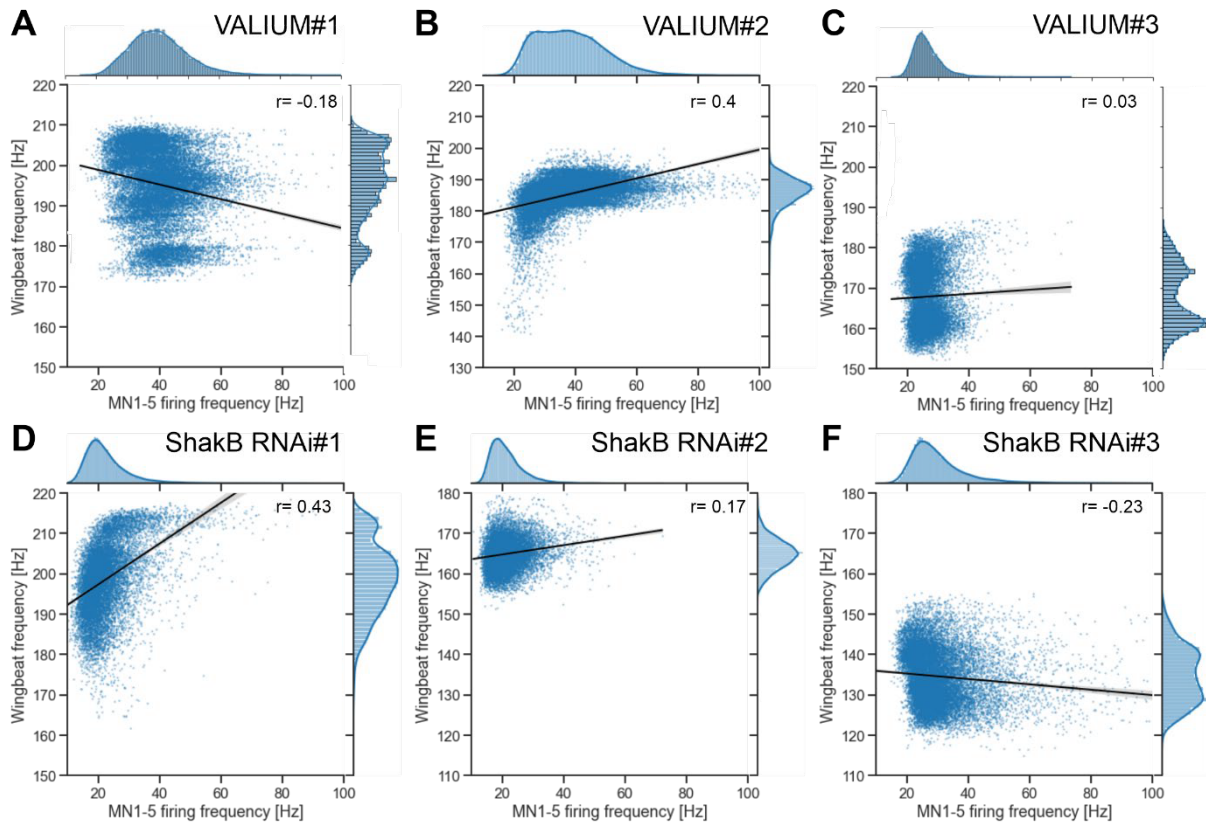
Figure 23: Wingbeat frequency to MN firing frequency of MN1-5 in control (**A-C**) and *shakB* RNAi (**D-F**). The Pearson correlation coefficient (r) varies for both genotypes between positive and negative. The firing frequency and wingbeat frequency was calculated for every single firing pattern, with the frequency calculated for the duration of the respective pattern. All six animals have 10 min of flight time.

The correlation between the total MN firing frequency and wingbeat frequency varies strongly and can even be negative as in Fig. 23A. This might be due to a fatiguing effect when the wingbeat frequency decreases over flight time, consequently the correlation between MN firing frequency and wingbeat frequency is decreased.

Another way to examine the relationship between MN firing frequency and the effect on the wingbeat frequency is to look at the change in frequency. Here, Nelson Niemeyer calculated the first derivative of both frequencies in 1 second bins and plotted the change in MN firing frequency against the change in wingbeat frequency. The correlation in this example indeed increases from 0.31 to 0.59 (Fig. 24AB). For other animals the correlation is not always increasing but is consistently positive (Fig. 24C). Therefore, there is a positive correlation between the change in MN firing frequency and change in wingbeat frequency, but not necessarily between the absolute frequencies.
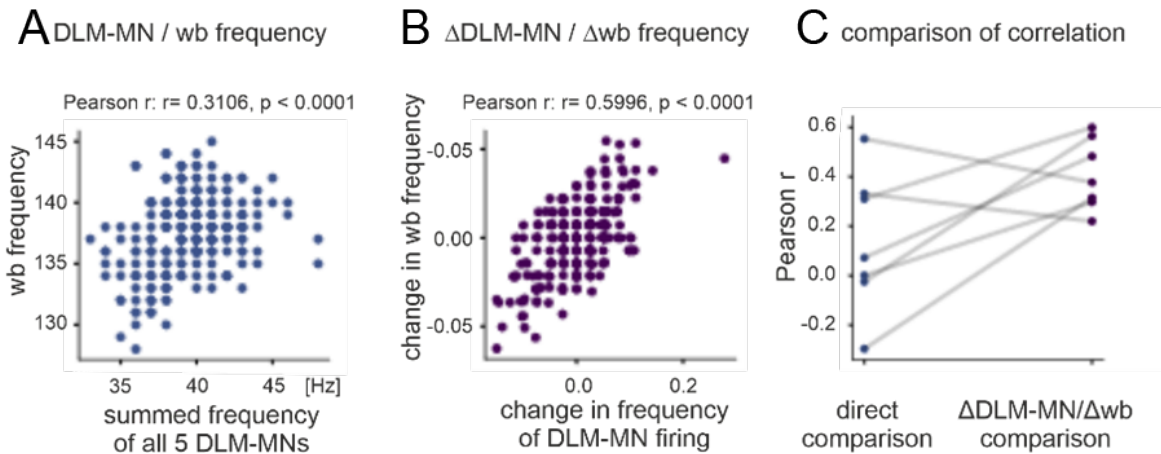
Figure 24: A The correlation between MN firing frequency and wingbeat frequency in one control animal with a broader point spread when compared to the change of both frequencies (**B**). The correlation between MN firing frequency and wingbeat frequency is mostly lower than the correlation between MN firing frequency and change of rate in the wingbeat frequency (C). Figure from Nelson Niemeyer.

3.5 DLM-MNs are dye coupled

Since the knockdown of the gap junction forming gene *shakB* had a strong effect on the firing relation of the MNs we want to investigate electrical coupling between MNs. One way to show electrical coupling between neurons is to demonstrate dye coupling. This can be done by dissecting a fly to reveal the ventral nerve cord (VNC) and load MN5 with a dye iontophoretically. Here, flies with a Drosophila FMR1 (*dfmr1*) RNAi knockdown were used, which was shown to increase the dye coupling effect in the giant fiber system (Kennedy & Broadie, 2017). After approximately 10 min minutes of dye (neurobiotin and Dextran-3000 1:1 mixture, see methods) filling by iontophoresis at the soma of MN5, the other somata of MN1 to MN4 become barely visible live under the microscope. However, according to the immunohistochemistry protocol using a Streptavidin Alexa 647 conjugate and imaging with the CLSM, MN1 to MN4 are visible, as well as the soma of MN5 of the other side of the body (Fig. 25). On top of MN1-4, small somata of probably four other unidentified cells are brightly visible (white arrows). The small motor network is weakly dye coupled in a FMR1 knockdown and probably even the networks of both body sides are interconnected.
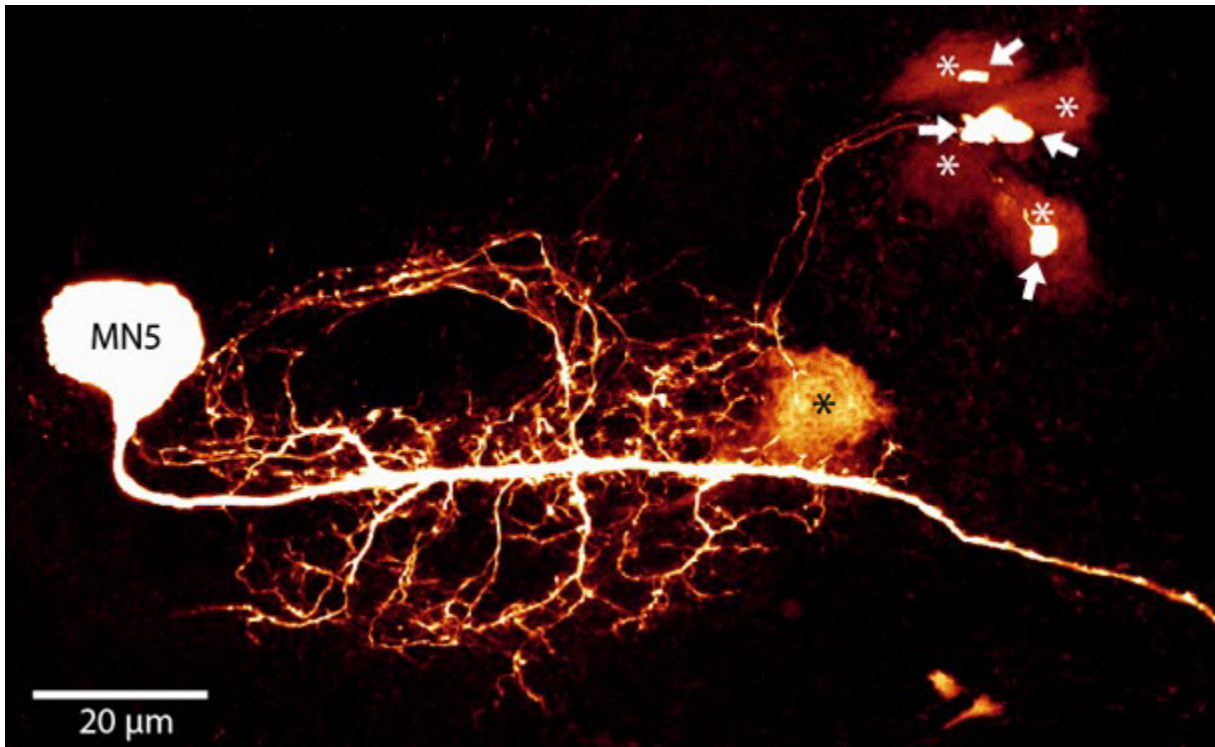
Figure 25: Dye coupling of DLM-MNs in a *dfmr1* RNAi knockdown in the DLM-MNs. The soma, dendrites, and primary neurite of MN5 are clearly visible after dye filling, but also the somata of MN1-4 on the contralateral side become visible (white asterisks). Even the soma of the right MN5 is faintly visible (black asterisk). On top of the somata of MN1-4 smaller bright somata of unidentified cells are visible (white arrows).

3.6 Synchronous spikes lead to strong fluctuations in the wingbeat frequency

We tested whether the gap junction manipulation has a functional consequence on the wingbeat. The wingbeat frequency of *Drosophila melanogaster* in stationary flight is around 200 Hz, but also fluctuates over time. These fluctuations are minor over several milliseconds but can be stronger over longer time periods and are likely triggered by visual or olfactory cues. In a fly overexpressing the ShakB(N+16) variant, where MN5 and MN4 fire synchronously stronger fluctuations immediately after the time point when the MNs fire (Fig. 26, red line in comparison to black line in the bottom panel). The wingbeat frequency increases by about 5 Hz over 50 ms and falls back to the frequency before the next synchronous spike within 50 ms.
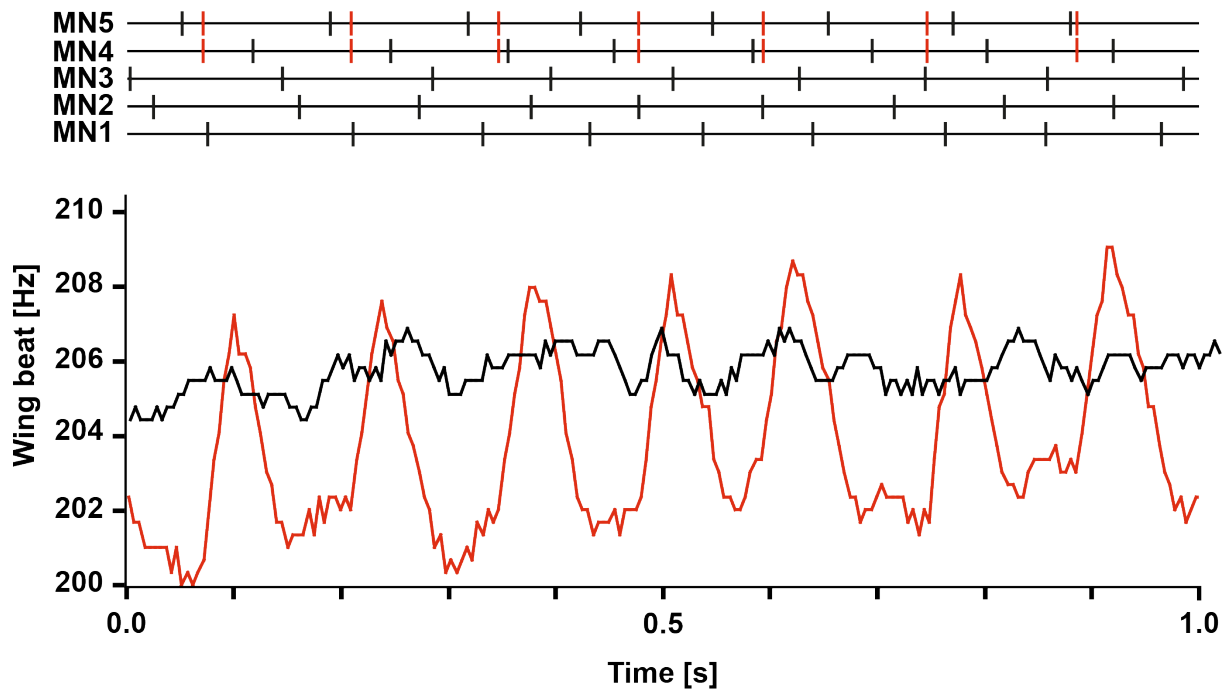
Figure 26: Wingbeat frequency over time in control (black) and ShakB(N+16) overexpression (red). In the control animal we have the firing pattern of all MNs in the splayed state and the accompanying wingbeat frequency over time with a stable frequency. The ShakB(N+16) overexpression leads to synchronous spikes of MN5 and MN4 seen in red, MN1 to MN3 are not recorded. In the red trace of the wingbeat frequency, we see a strong increase shortly after synchronous spikes, but also a strong decrease within 50 ms.

To quantify the effect of the MN firing on wingbeat frequency, the waveform average of the wingbeat frequency with a time frame around each MN firing can be calculated. Therefore, data of seven flies each with ten minutes flight time was used. In the control group, the waveform average drops by ~0.4 Hz before and during the triggering time point, increases by ~0.4 Hz within 5 ms, and then drops back to a stable local wingbeat frequency (Fig. 27A, green). Knocking down *shakB* leads to an increase of the waveform average of the wingbeat frequency by ~1 Hz which also persists for a longer period of time compared to the control (Fig. 27A, blue trace). Overexpression of ShakB(N+16) has an even stronger effect on the waveform and the wingbeat frequency increases by ~5 Hz (Fig. 27A, red trace). However, a broader spread of the wingbeat frequency change from 1 to 6 Hz can also be observed. To conclude that only the synchrony of the spikes is responsible for the intensity of the wingbeat frequency change, asynchronous and synchronous spikes of one animal with a ShakB(N+16) overexpression were sorted. The amplitude of the average waveform triggered by 939 asynchronous spikes (Fig. 27B, black trace) is about 60% smaller than the waveform amplitude triggered by 3601 synchronous spikes (Fig. 27B, red trace). Therefore, the synchronicity of the spike is responsible for the stronger wingbeat frequency fluctuations.

Figure 27: Waveform average of wingbeat frequency around MN firing. **(A)** MN firing increases the wingbeat frequency stronger in the ShakB overexpression (red), weaker in the *shakB* knockdown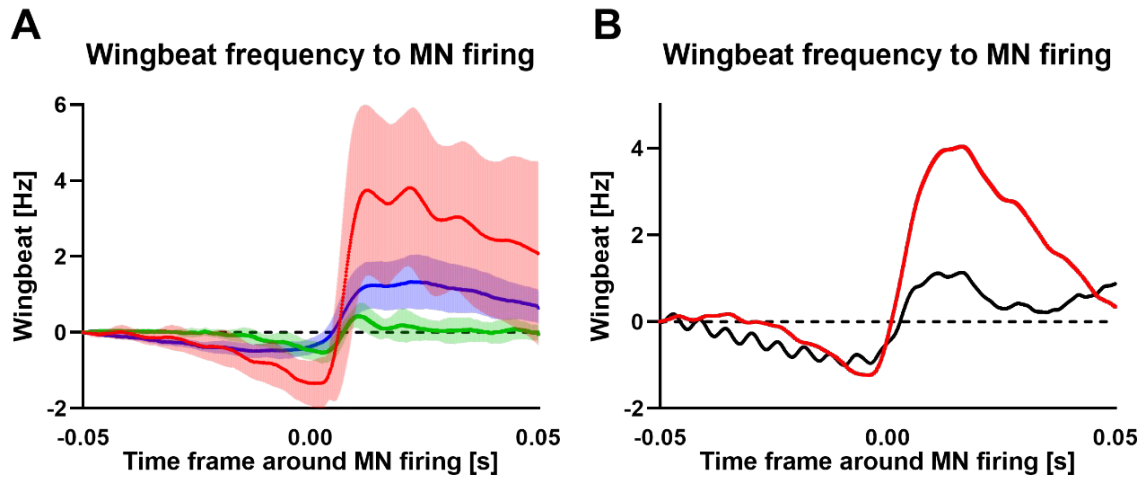 (blue) and weakest in the control (green). **(B)** Asynchronous and synchronous spikes of one animal were sorted to trigger a waveform average. The waveform average of the wingbeat frequency triggered by 939 synchronous spikes in red rises to 4 Hz, whereas the change in wingbeat frequency for 3601 asynchronous spikes is around 1 Hz.

3.7 The *shakB* knockdown influences the overall interspike interval stability

To quantify the effect of the *shakB* knockdown on the firing stability of the whole network, point caré plots are a useful tool. They depict the distribution of the change of the interspike interval (ISI) to the following ISI. A regular firing neuron would create a point caré plot with dots on a bisecting straight line, depending on the firing frequency. When the ISIs differ to one another, they deviate from this line and represent an irregular firing behavior. For a representative animal, the point cloud is spread approximately 0.05 s from the bisecting line for every single MN (Fig. 29A-E). Considering the scatter of the point cloud with all five MNs added to one timeline, the ISIs are accordingly shortened, and the scatter is around 0.025 s (Fig. 29F). There are nearly no ISIs shorter than 0.1 s, which is also true for the following ISI (ISI+1). For a *shakB* knockdown, the scatter for the individual MNs is indistinguishable from the control, but when we consider the timeline where all MNs are added, the ISIs are scattered over all time points <0.125, but especially near shorter ISIs (Fig. 30F). This is also evident in the interval histogram on the outer axes of the plots. Just to emphasize, this is true even though both animals fire at the same frequency of about 5 Hz (ISI 0.2s). The firing relationship to the other MNs is changed, but not the firing variability of single MNs. This is also reflected in the coefficient of variation (CV), there is no strong difference within each animal between the MNs and the value of the *shakB* RNAi animals are in the range of the control animals (Fig. 28).
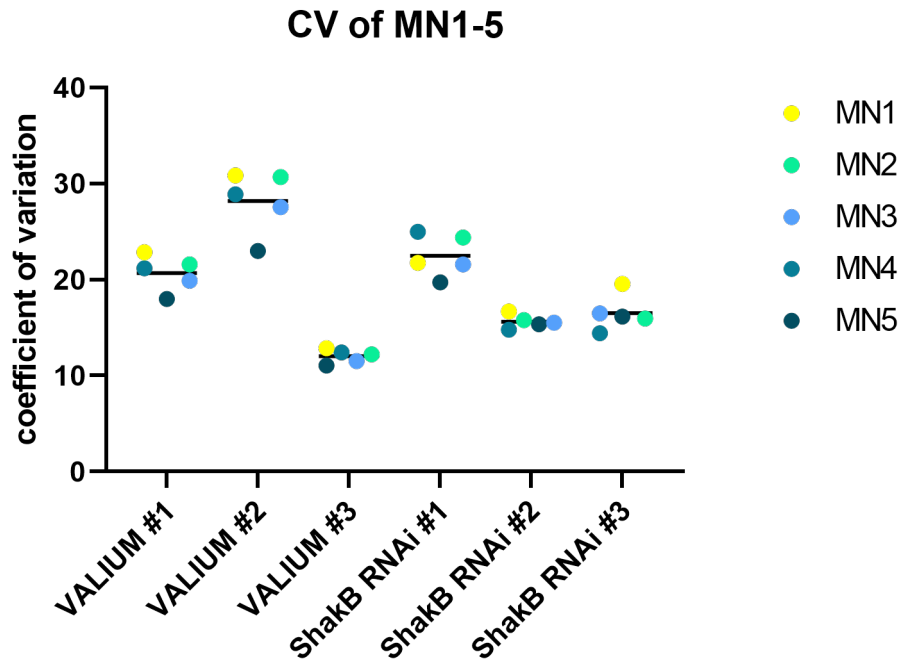
Figure 28: The coefficient of variation of MN1-5 is similar within each animal, but there seems to be no obvious difference between control and the *shakB* knockdown.
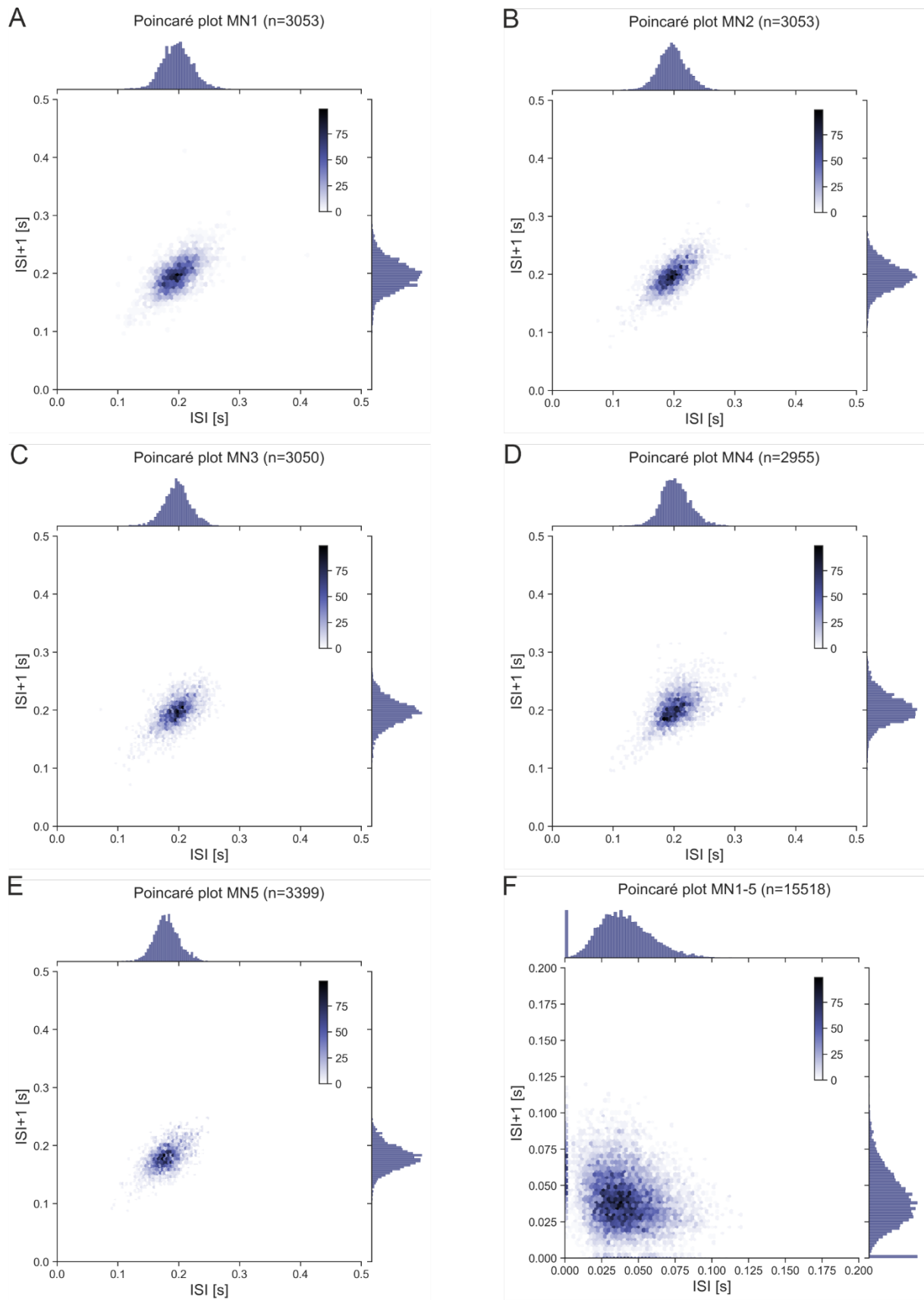
Figure 29: Point caré plots of MN1-5 in one VALIUM control animal. **A-E** ISI and following ISI are distributed over a time frame of approximately 0.2 ±0.1 s for all single five MNs. **F** MN1-5 and synchronous firing is visible on the x- and y-axis, but most MNs fire around 35ms after the previous MN firing.
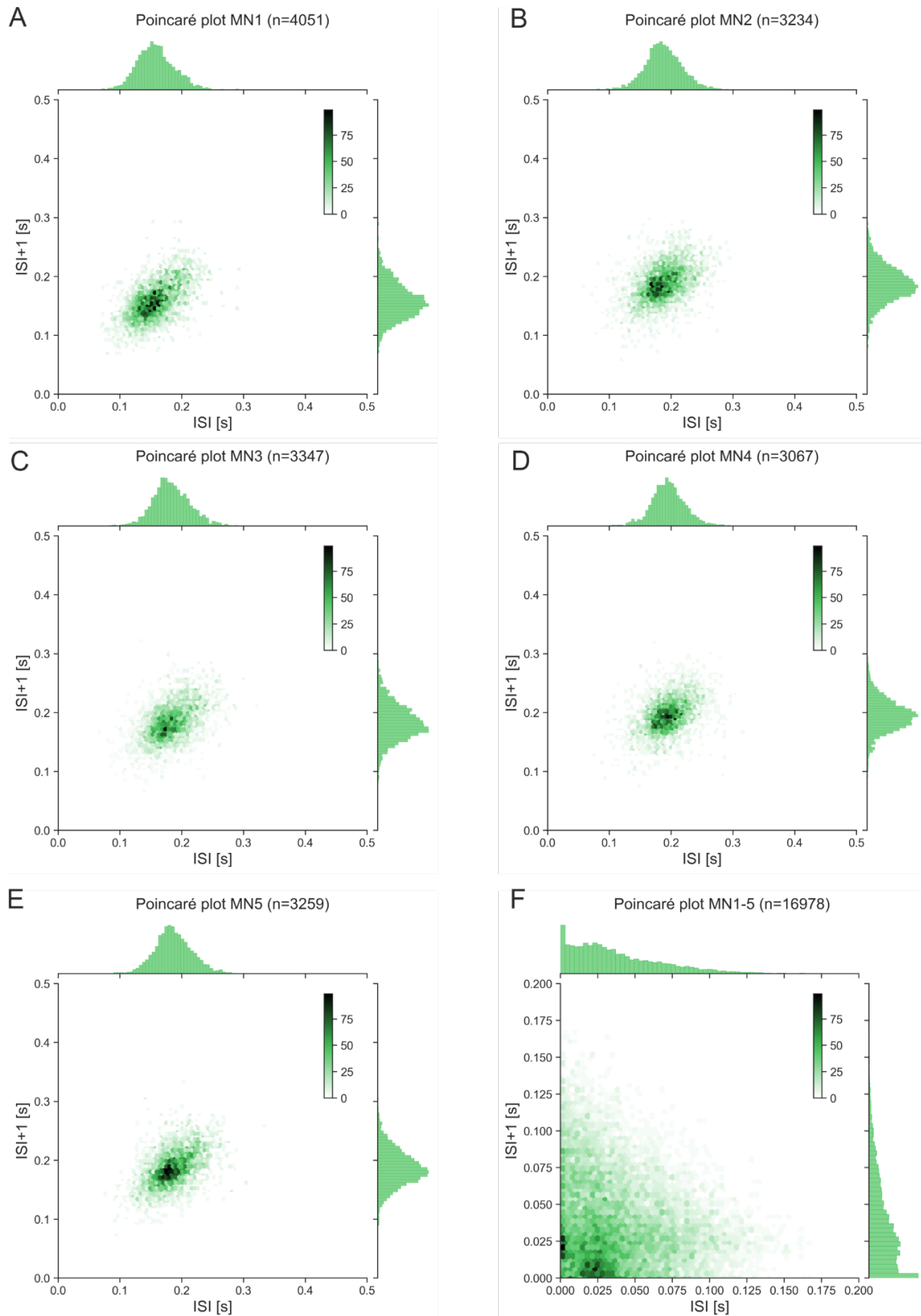
Figure 30: Point caré plots of MN1-5 in one *shakB* RNAi animal. **A-E** ISI and following ISI are distributed over a time frame of approximately 0.2 ±0.1 s for all single five MNs. **F** MN1-5 and synchronous firing is visible on the x- and y-axis, but most MNs fire around 35ms after the previous MN firing.

3.8 The *shakB* knockdown decreases firing pattern stability

When looking at the firing pattern of MN1-4, a preferred sequence can be found, which was already described by Wyman et al. in 1977. When starting with MN1 and only counting patterns without repetitions, there are six possible sequences (1234, 1243, 1324, 1342, 1423, 1432). The two most preferred sequences start with MN1 and are followed by MN3 or MN4. Then comes MN2, followed by MN3 or MN4, depending on which one fired before MN2.Thus, the pattern is 1423 or 1324. Now the cycle can start again. We already know that the firing relationship is changed in the *shakB* knockdown since ISIs of a timeline with all MNs have ISIs smaller than 0.015 sec, which is also reflected in the phase histograms as exclusion bands. Still the question remains if the MNs only fire closer together or if they also change their firing sequence. In all 8 control animals we can observe the most preferred sequence 1423 with the flight time ranging from 100 to 600 sec (Fig. 31A). In 3 *shakB* knockdown animals, the preferred sequence is always different and occurs less frequent, but the patterns that do not fit the six default patterns (rest) are also increased (Fig. 31B).
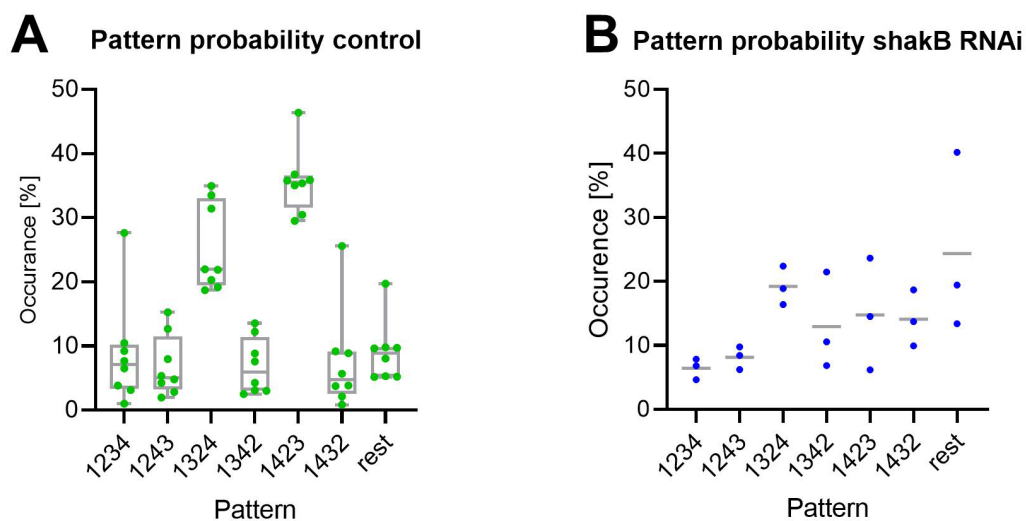
Figure 31: Probability of different firing patterns in control (n=8) and *shakB* RNAi knockdown (n=3). **A** In control, patterns 1423 and 1324 are preferred. **B** In the *shakB* knockdown, there are no preferred sequences and patterns not fitting the six standard patterns (rest) have a higher probability.

The further firing pattern analysis is based on three VALIUM control animals and three flies with a *shakB* RNAi knockdown with 600 sec of flight time. Except for animal VALIUM #1 (here the pattern 1432 is with 25%, 5% higher than 1324 with 20%) the second pattern is as expected 1324 (Fig. 32ABC). In three animals with the shakB knockdown the highest value for one pattern is 24% and is also the preferred sequence

1423 (Fig. 32D). Animals #2 and #3 have the patterns 1342 and 1324 with 21% and 22% occurrence respectively, neither of which is the preferred default pattern. Additionally, the probability for patterns with repetitions (rest) is higher ranging from 13% to 40%, whereas in control animals it ranges from 5% to 10%. Thus, the *shakB* RNAi knockdown affects the stability of the firing pattern.
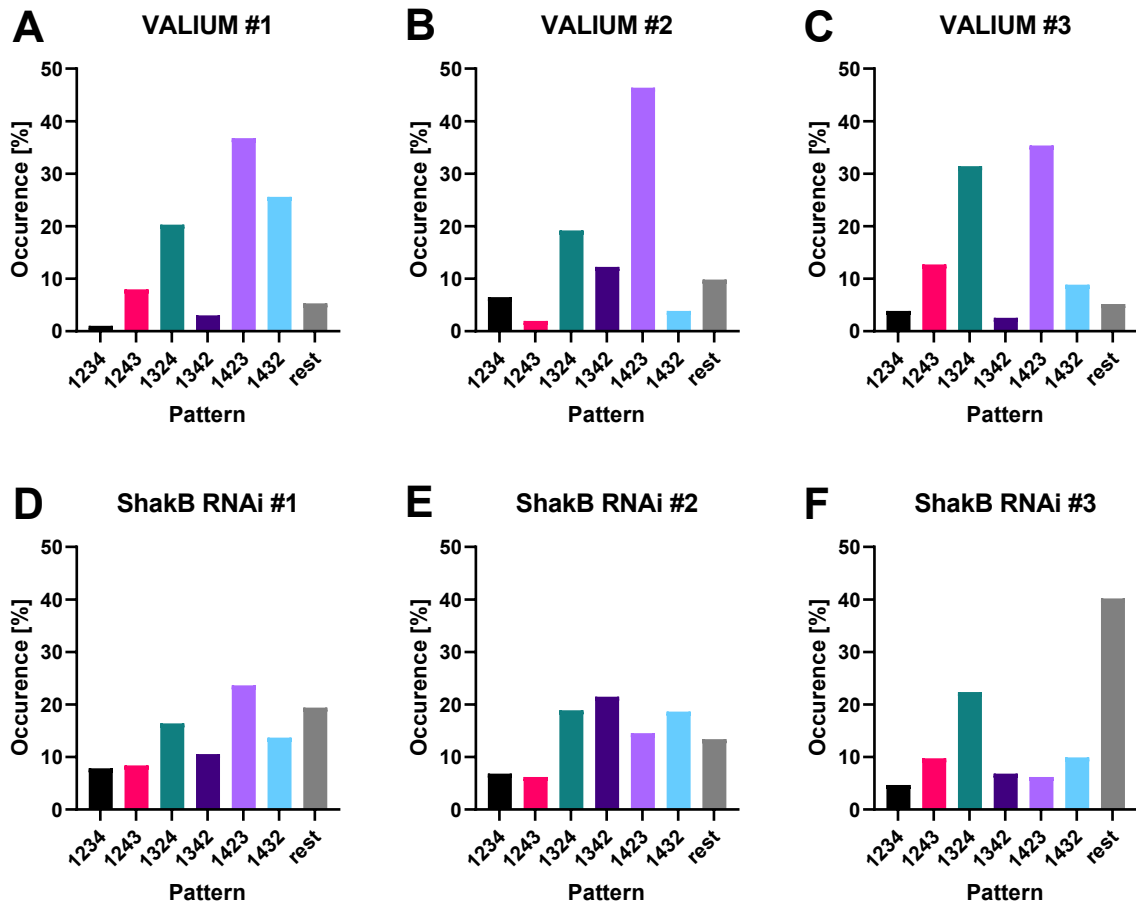
Figure 32: Occurrence of patterns in VALIUM control **A**-**C** and *shakB* RNAi knockdowns **D**-**F**. In control animals there is always the preferred sequence 1423 nearly 40% of the time, whereas in the *shakB* knockdown, all three animals have a different preferred sequence with around 20%. Also, the proportion of patterns not included in the six patterns without repetition is higher and reaches in animal #3 40%.

We can also calculate for each animal the probability of staying in the same pattern. For control animals it ranges from 42% to 85% whereas for the *shakB* knockdown it ranges from 32% to 33% (Fig. 33). On average with 63% the control has nearly double the probability to stay in the same pattern, whereas the *shakB* RNAi stays in the same pattern with a mean probability of 33%. Additionally, there is a difference in length of consecutive patterns of the same repeating pattern are. In control animals, one pattern repeated itself 109 times, equal to 0.5% of all patterns (Fig. 34). When the gap junctions are knocked down, the longest streak is 11 and 35% of all patterns. In the control only 11% are not repeating itself (Fig. 34A). On a logarithmic scale, the number of longer consecutive patterns compared to *shakB* RNAi is easier visible in the non-overlapping part in green (Fig. 34B).
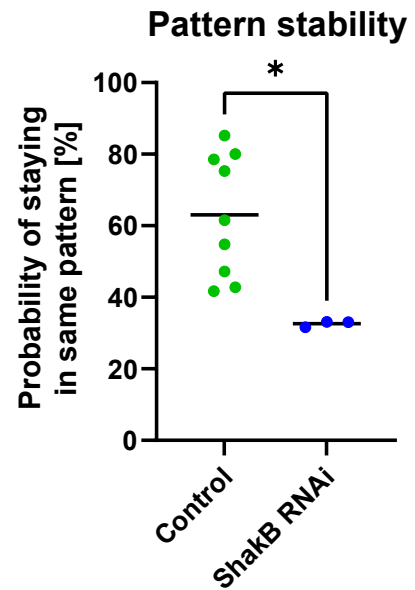
Figure 33: The probability of staying in the same pattern is in control significantly higher with 63% in the mean, compared to the *shakB* RNAi with 33%.
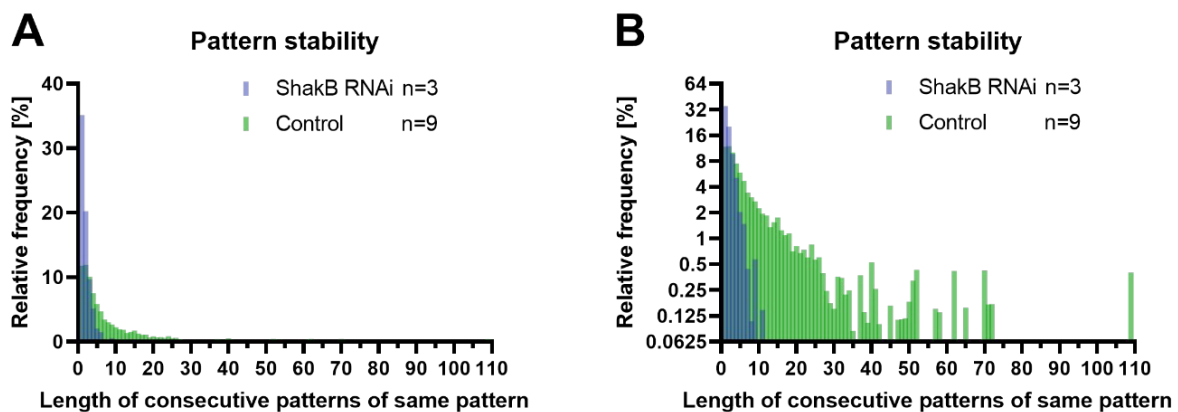
Figure 34: The length of consecutive patterns in the same pattern is higher in control compared to *shakB* RNAi. Linear x-Axis in **A** and Log 2 in **B**.

To investigate whether preferred sequences are necessary for specific firing frequencies, the firing frequency for each individual firing pattern was calculated. There are more significant differences between MN firing frequencies of different patterns in the control animals, than in the *shakB* RNAi (Fig. 55). A broader distribution of the frequencies in the *shakB* RNAi is also visible (Fig. 35DF). The preferred firing patterns in the three control animals tend to fire at lower frequencies (Fig. 35ABC violet). For

shakB knockdown animals there are 19 of 45 possible significant differences, whereas in the control animals 34 of 45 combinations are significantly different. Only between pattern 1342 and 1432 is no significant difference in all three control animals (Fig. 55). This suggests that the patterns fire at different frequencies, but this could also be a consequence of the more stable firing of the control animals and therefore a stronger correlation between local firing frequency and pattern.
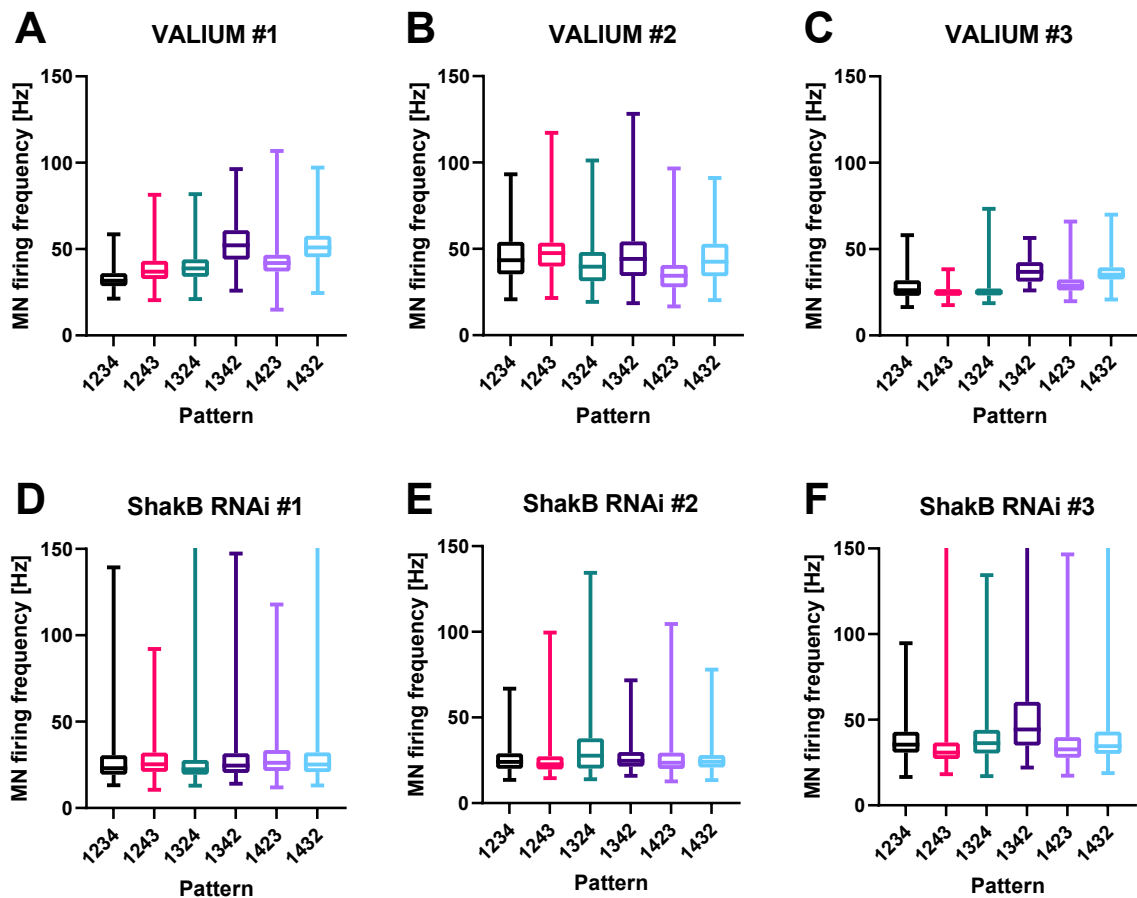
Figure 35: MN firing frequency during different firing patterns. **A-C** The MN firing frequency differs between MN firing patterns. **D-F** In the *shakB* RNAi knockdown the MN firing frequencies are closer together. For the statistical comparison see Fig. 55.

The firing sequence has no clear effect on the wingbeat frequency

Next, the dependence of the wingbeat frequency on the MN firing pattern was investigated. Therefore, all patterns were sorted into the six possible sequences, by a custom written python script, and all time points were stored, when a new sequence started. These time points were imported into Spike2 and the waveform of the wingbeat frequency was averaged at the time point of MN1 firing from each corresponding

pattern 0.5 sec before and after MN1 firing. For the first two control animals a straight line within a range of 4 Hz can be seen for all patterns. Only the patterns 1234 and 1243 have an about 2 Hz higher wingbeat frequency with about 197 Hz (Fig. 36A, black and pink line). For the third animal, the waveform average of all patterns fluctuates around 2 Hz at the triggering time point and the average frequency of the different patterns is spread out over 10 Hz. The preferred sequence 1423 shows the highest wingbeat frequency with 170 Hz and the "rest" (not attributed to the six defined patterns) the lowest frequency with ~162 Hz. For the *shakB* knockdown all waveform averages are fluctuating around the triggering time point with a short decrease immediately before the time point 0 and an immediate increase thereafter (Fig. 36DEF).
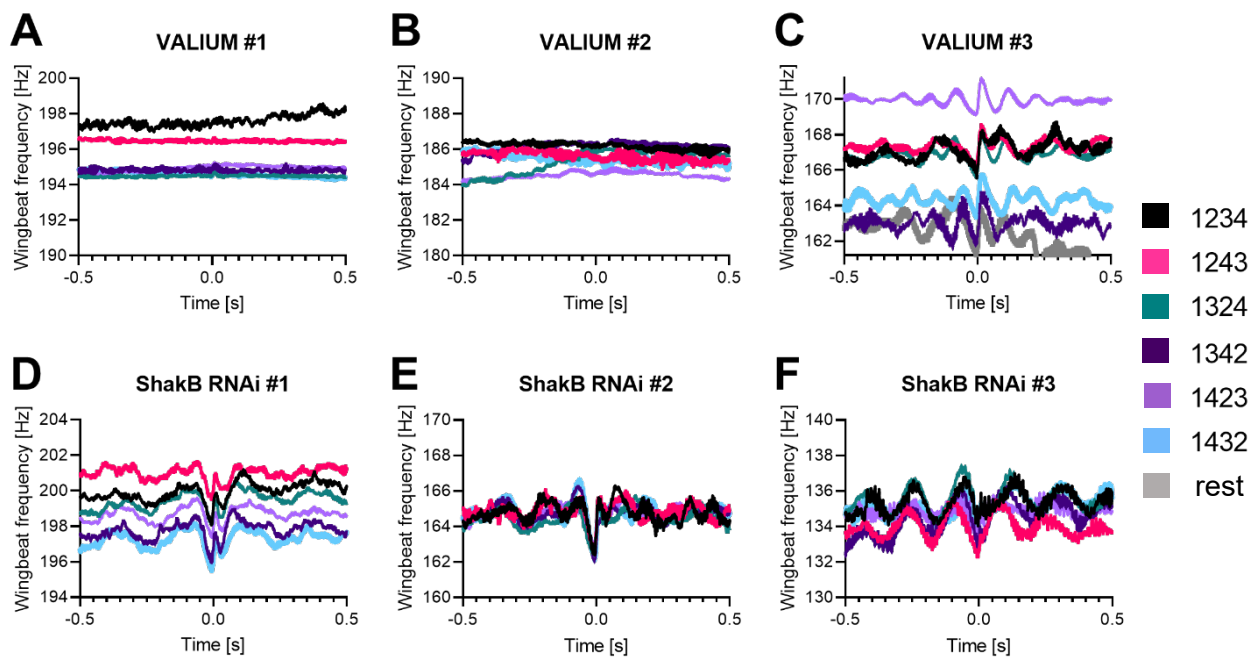
Figure 36: Waveform average of the wingbeat frequency during different MN firing patterns. **AB** In the first two control animals the wingbeat frequency is steady during MN firing (time 0.0), whereas in the third animal **(C)** the waveform average fluctuates around 2 Hz for 100 ms around the MN firing and also the average wb frequency is on different levels, where the preferred sequence 1423 has the highest wb frequency with 170 Hz. **D-F** In the *shakB* RNAi knockdowns all waveform averages of the wb frequency fluctuates around 2 Hz for approximately 100 ms shortly before and after MN firing.

Since in animal VALIUM #3 the patterns result in waveform averages with different mean frequencies, it could be interesting to correct for the frequency at which the pattern fired. This should clarify whether the higher average wingbeat is due to the higher MN firing frequency or the firing pattern itself. A python script was used to calculate the firing frequency of each pattern, binning the pattern frequency in two bins

ranging from 25 to 30 Hz and 30 to 35 Hz, and again, derived the waveform average for every pattern. The remaining frequencies are not considered for further analyses. In animal VALIUM #1 the waveform average of the preferred sequence of 1423 in light purple is lower than two other sequences (Fig. 37A), but it becomes the sequence with the highest average when it is sorted in the frequency bins (Fig. 37 BC). The increase of the average wingbeat frequency for the preferred sequence also applies to animal VALIUM #2, where it rises from lowest to highest average wingbeat frequency in the 30-35 Hz MN firing frequency bin (Fig. 37F) and second highest in the 25-30Hz bin (Fig. 37E). For animal #3, the preferred sequence shows always the highest average wingbeat frequency but shares it with the second most preferred sequence in the 30-35Hz frequency band.
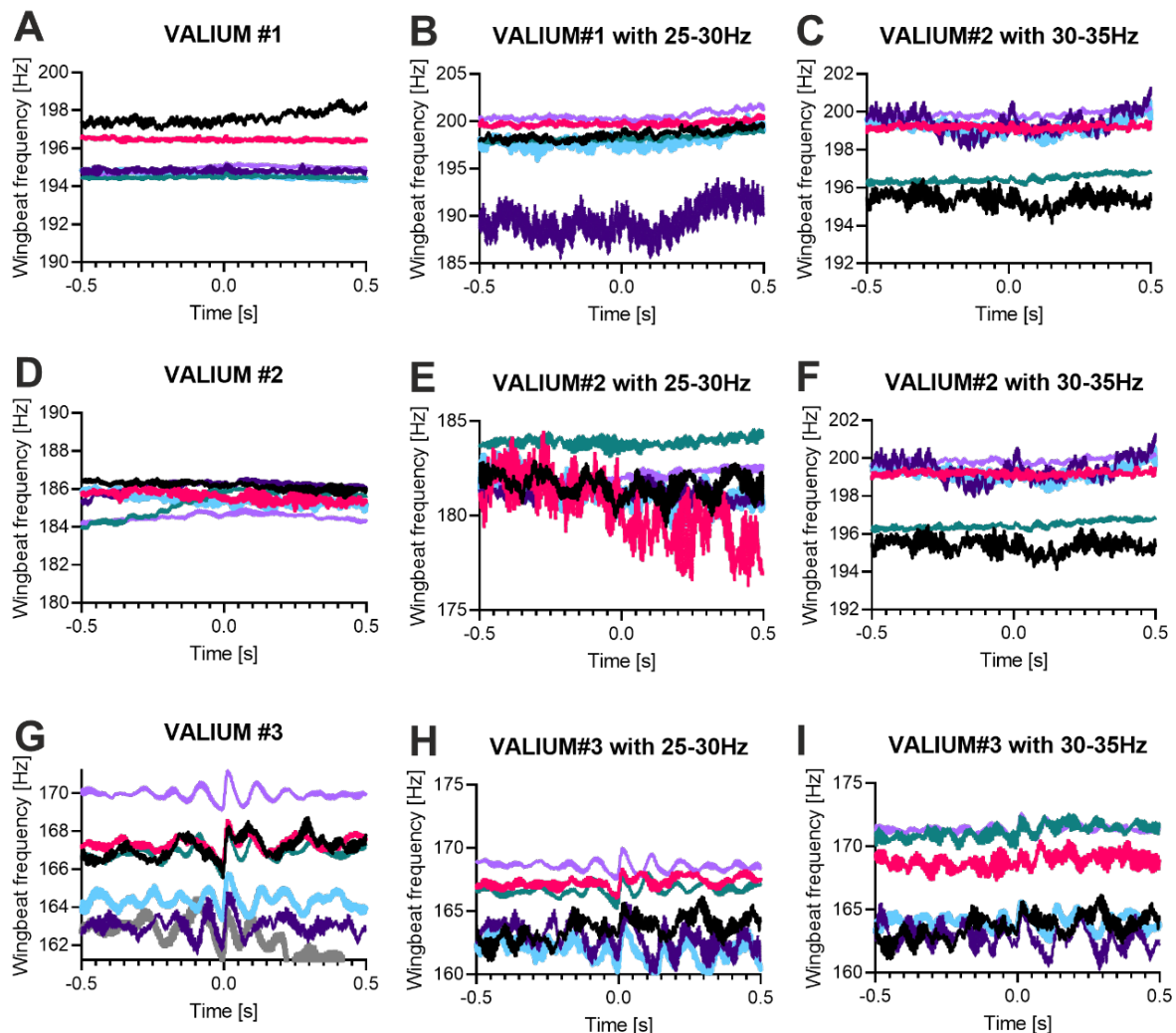
Figure 37: Waveform average of the wingbeat frequency during different MN firing patterns with all MN firing frequencies **(A,D,G)**, 25-30 Hz **(B,E,H)** and 30-35 Hz **(C,F,I),** recorded in three VALIUM control animals. In animal #1 the average wingbeat frequency for the preferred pattern 1423 (light purple) is increasing relative to the other patterns in the two MN firing frequency ranges, which is also true for the second animal. For the third animal the preferred sequence has the highest average wingbeat frequency in all frequencies, but shares it in the 30-35Hz bin with the second preferred sequence 1324.

To evaluate the influence of every MN firing on the wingbeat frequency the waveform average can be derived at every MN firing independent of the firing pattern. There is a clear difference in the size of the fluctuation around the MN firing time point. In the control, the fluctuation is almost invisible in animal #2 and is 1 Hz in animal #3 (Fig. 38ABC). In all *shakB* knockdowns, the fluctuation is at least 3 Hz. This shows that not only MN4 and MN5, as previously shown in Fig. 27, but the influence of the firing time point of all MNs destabilizes the wingbeat frequency over approximately 200 ms in a *shakB* knockdown (Fig. 38DEF).
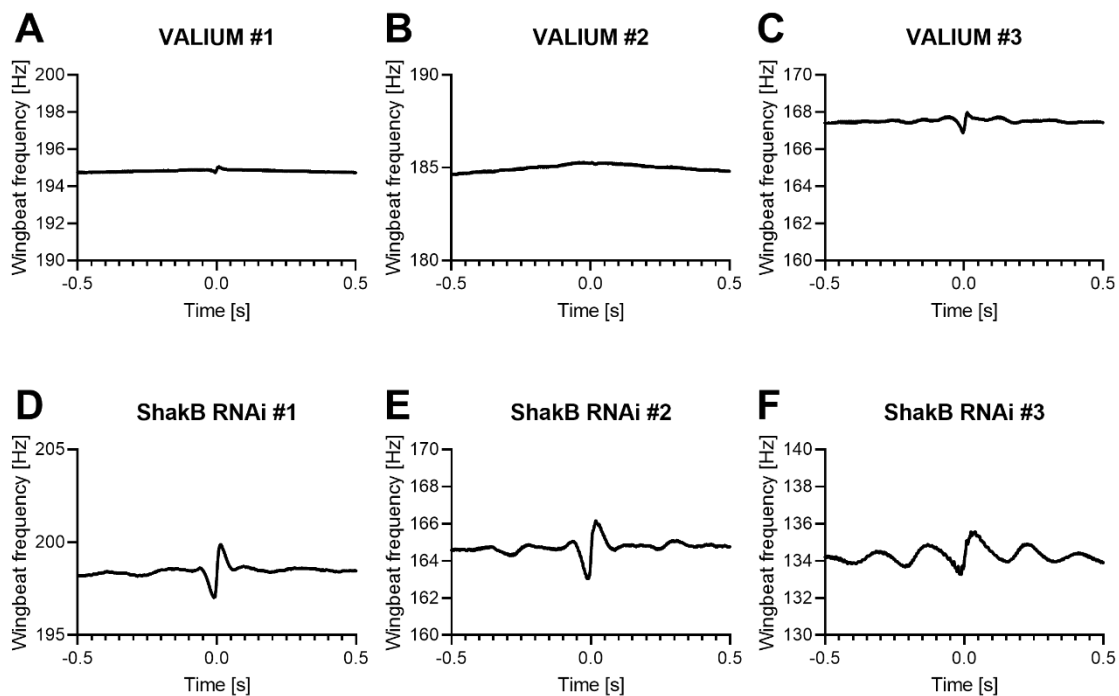
Figure 38: Waveform average of the wingbeat frequency during every MN firing. **A-C** The waveform average of the wingbeat frequency during every MN firing (MN fires at 0 s) is stable and only in **C** a short decrease of around 1 Hz is visible before MN firing and is returning to the starting level. **D-F** In the *shakB* RNAi knockdown the wingbeat frequency is fluctuating with a sudden decrease of 2 Hz within 10 ms before MN firing followed by an increase of around 3 Hz within 5 ms above a frequency before MN firing and is returning to the average wingbeat frequency.

The efficiency of the different patterns might be indicated by the wingbeats generated per MN firing within one pattern. In the three control and *shakB* RNAi animals the pattern 1342 is the least or second least efficient pattern in 5 out of 6 cases (Fig. 39). However, there is no statistically significant difference between all patterns with a 2-way ANOVA turkey's multiple comparison test (also with pooling both genotypes). A possible reason for no significance might be an insufficient sample size.
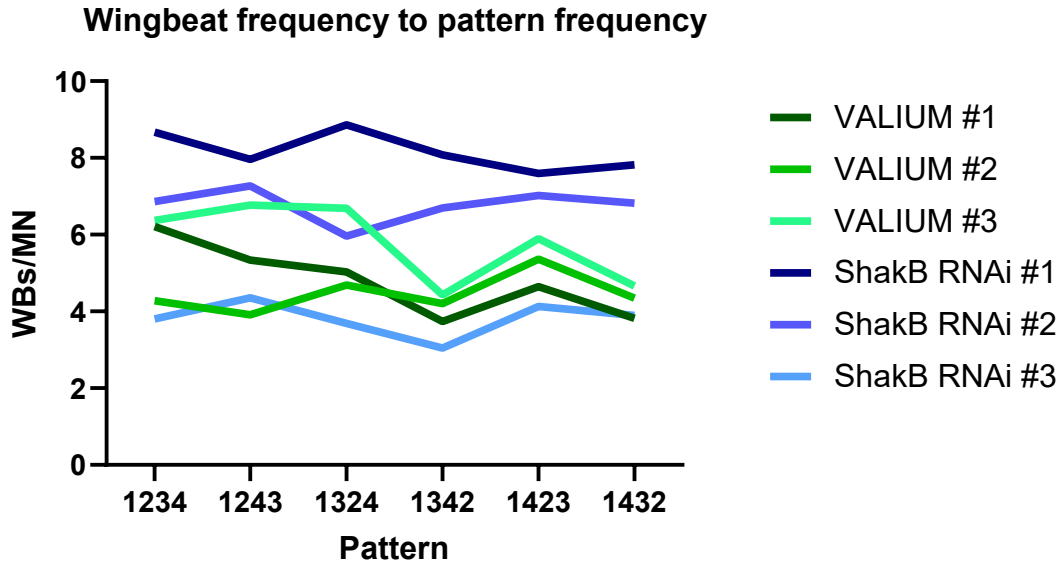
Figure 39: The wingbeat frequency to pattern frequency ratio during different firing patterns. The three animals with the *shakB* RNAi are distributed over a wider range. A 2-way ANOVA Tukey's multiple comparison test shows no significant difference between patterns if control and *shakB* RNAi animals are pooled.

Instead of taking the average firing frequency of each pattern and wingbeat frequency, the firing frequency of every single pattern to the corresponding wingbeat frequency can also be plotted. As a representative example one control animals was used, where a slight shift of the point cloud of the pattern 1432 to the higher MN firing frequencies can be observed. This does not necessarily imply an increase in the wingbeat frequency (Fig. 40F). This again shows that the correlation between MN firing frequency and wingbeat is very different even when sorted for the different patterns.
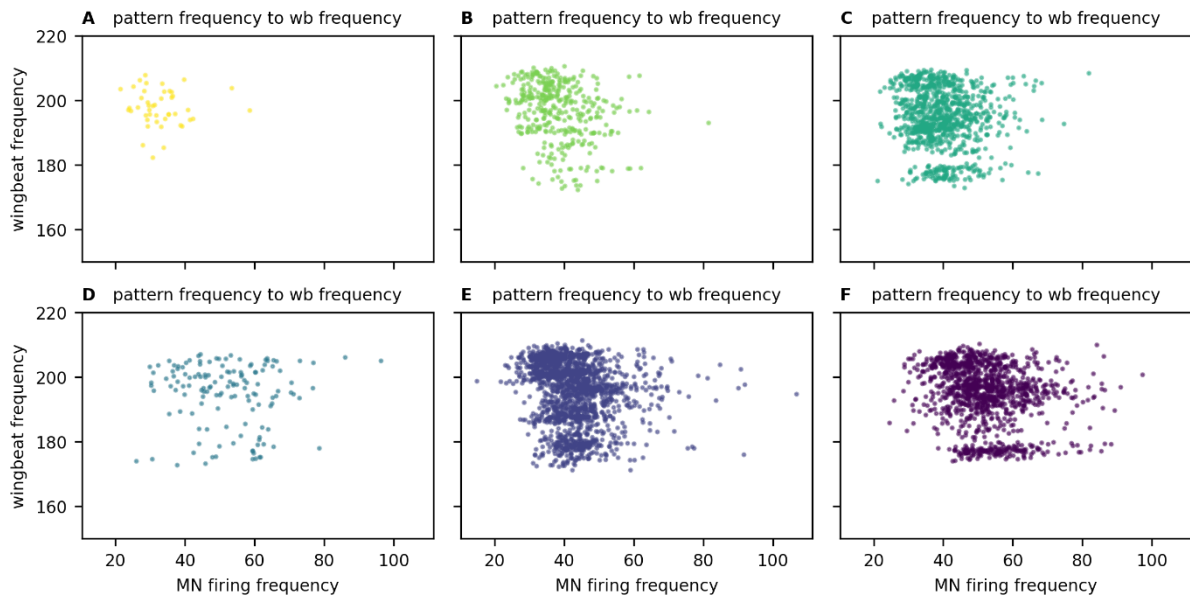
Figure 40: All possible firing patterns have a broad distribution of MN firing frequency to wingbeat frequency. **A** The pattern 1234 has only few points, since it is not a preferred sequence and is firing with a relative low frequency 20-40 Hz and is reaching 190-210 Hz in the wingbeat frequency. For the other patterns 1243 (**B**), 1324 (**C**), 1342 (**D**), 1423 (**E**) and 1432 (**F**) there are more points spread over a wider range.

The firing pattern preference is also visible in the phase histograms

The phase histograms previously shown have distributions with local maxima, indicating the preference of firing around the corresponding phase. As an example, in the phase histogram of MN1 to MN3 (animal Valium #1), there is a triphasic distribution, with local maxima at phase ~0.2, ~0.45 and 0.8 (Fig. 41A). When the firing of MN1 in the phase of MN3 is color-coded to different firing patterns the three maxima can be assigned to the patterns 1324, 1432 and 1423 respectively. The global maximum at phase 0.8 corresponds to the preferred pattern 1423. The third digit after 1 in the pattern 1423 is 3 and in the phase histogram it is the third local maximum at phase 0.8. All possible phase histograms of MN1 to the other MNs in the different patterns are shown in the appendix (Fig. 56-58). In the phase histogram of MN1 to MN5 the distribution is uniform, showing no local maxima (Fig. 58). This fits the idea, that the phase relationship is weaker between MN1 and MN5. Other MN combinations show the distribution with local to no local maxima in different degrees (Fig. 56+57).
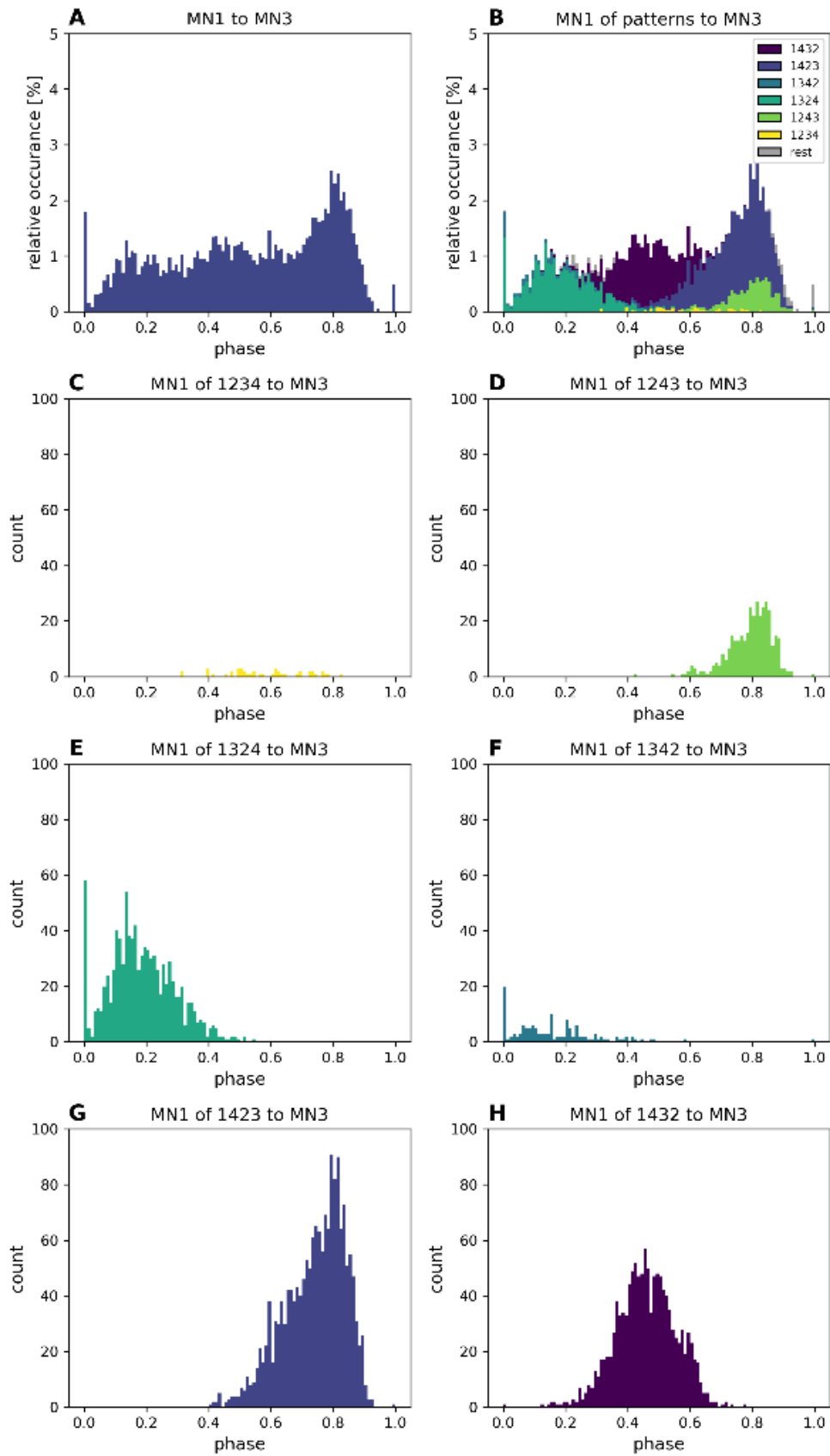
Figure 41: Phase histograms for MN1 in all patterns to MN3. **A** MN1 is firing nearly during the whole phase, but not shortly after 0 and before 1. **B** The same phase histogram as in A, but MN1 is color coded in the six possible patterns (legend). **C-H** Phase histograms of single patterns as in B, but with absolute numbers (count).

3.9 MNs are weakly, bi-directional and non-rectifying electrically coupled

To further investigate the characteristics of the electrical coupling of the MNs, Stefanie Ryglewski conducted *in situ* whole cell patch clamp recordings of two MNs simultaneously. MN1-4 are located ventrally in the VNC and accessible by a ventral dissection of the thorax. If a depolarizing or hyperpolarizing current is applied to one of the current-clamped cells (Fig. 42A, cell 1, left panel), a potential change in the other cell can be observed (Fig. 42A, cell 2, left panel). This proves electrical coupling of the two MNs. The ratio of evoked and coupled potential is ~0.019 and is also called the coupling coefficient (CC). Applying step currents in the other cell also results in a coupling potential with nearly the same CC. Suggesting that the electrical coupling is bi-directional. A linear increase in the current steps leads to a linear increase in the coupling potentials (Fig. 42B). The CC is 0.023 for 5 out of 15 measurements, about twice as large as 0.01 as in the other 10 (Fig. 42C). This ratio is consistent with the ratio of MN pairs in which stronger coupling to weaker coupling is expected (MN1/2 and MN3/4 with strong coupling to weak coupling in MN1/3, MN1/4, MN2/3 and MN2/4, which is 2/6 or 33%).
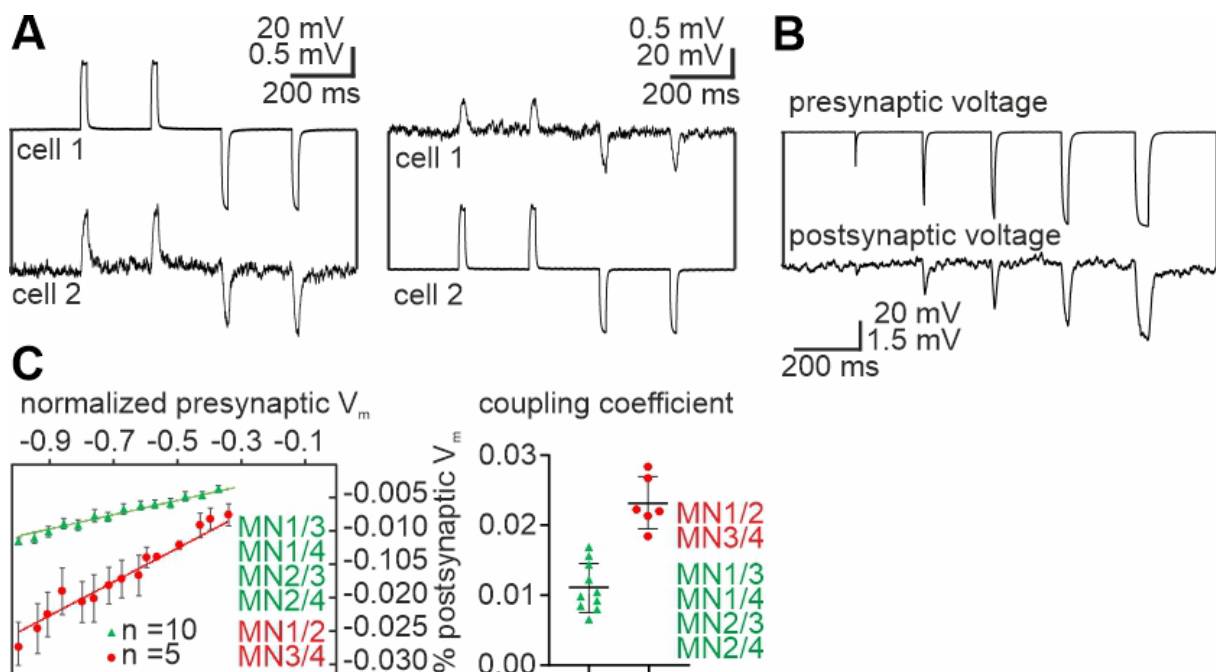
Figure 42: Different protocols in double patch recordings of two MNs show a linear, bi-directional and non-rectifying voltage transfer. **A** Two short depolarizations and hyperpolarizations in cell 1 have a weaker response of the same polarization in cell 2. Switching cell 1 and 2 in the protocol shows a similar response. The voltage transfer is bi-directional and non-rectifying. **B** Increasing the current steps linearly results in a linear increase of the postsynaptic response. **C** The presynaptic voltage transfers linearly to the postsynaptic voltage and shows stronger coupling between MN1+2 and MN3+4 and shows a weaker transfer in all other pairs. For the maximal presynaptic voltage divided by the maximal postsynaptic voltage, also called coupling coefficient, there is a significant difference between the MN1+2 and MN3+4 to all other MN pairs.

3.10 The electrical coupling preferentially transfers the AHP

When two MNs are firing freely during patch clamp in current clamp mode, they also tend to fire not shortly after one another (Fig. 43B), but there is no exclusion band before synchronous firing, as seen in the phase histograms during flight. The transmission of the AHP in the coupling potential is stronger with a CC of 0.042, whereas the depolarization has a CC of 0.01 (Fig. 43A).
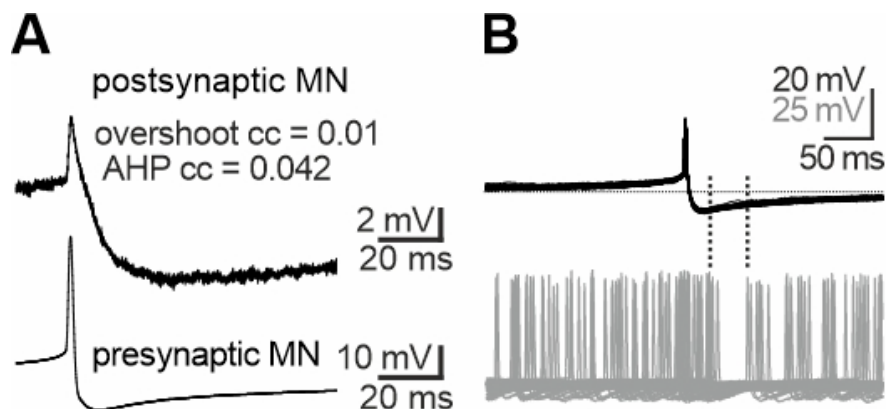
Figure 43: A The transmission of the AHP (CC=0.042) to the postsynaptic cell is stronger than the short depolarization (CC=0.01). **B** Spike trains in two MNs during patch clamp show interactions, where a lower probability of MN spikes shortly after the spikes of the presynaptic MN can be seen.

3.11 Applying the gap junction blocker Carbenoxolone into the thorax during tethered flight has no effect but blocks GJs during patch clamp

Carbenoxolone (CBX) is a gap junction antagonist, that has been shown to block gap junctions in *Drosophila* by bath application (Matsunaga et al., 2017; Wu et al., 2019). To better understand whether there may be developmental changes involved in the change of MN firing relationship upon *shakB* knockdown, we attempted to acutely block the gap junctions with CBX. Therefore, a picospritzer was used to inject CBX in solution into the thorax with a glass micropipette. To validate if the solution was distributed in the thorax, brilliant blue G was dissolved in the CBX solution, which resulted in a blue coloration of the hemolymph of the entire animal. Different concentrations, incubation durations and air pressures were tested, but the phase histograms before and after injection showed no difference. One possible explanation could be that the CBX is not able to pass the ganglionic sheath of the VNC. However, *in situ* patch clamp recordings of two MNs of MN1-5 performed by Stefanie Ryglewski showed that administering CBX does indeed block the coupling potential, which is also the case for the *shakB* RNAi

(Fig. 44). During preparation for patch clamping, the ganglionic sheath is enzymatically digested, likely allowing CBX to enter the VNC and block gap junctions.

A no voltage transfer from MN1 to MN2

MN1 | 30 mV

MN2 | 1 mV

B no voltage transfer from MN2 to MN1

MN1 | 1 mV

MN2 | 30 mV 100 ms

DLM-Split-GAL4>UAS-ShakB-RNAi
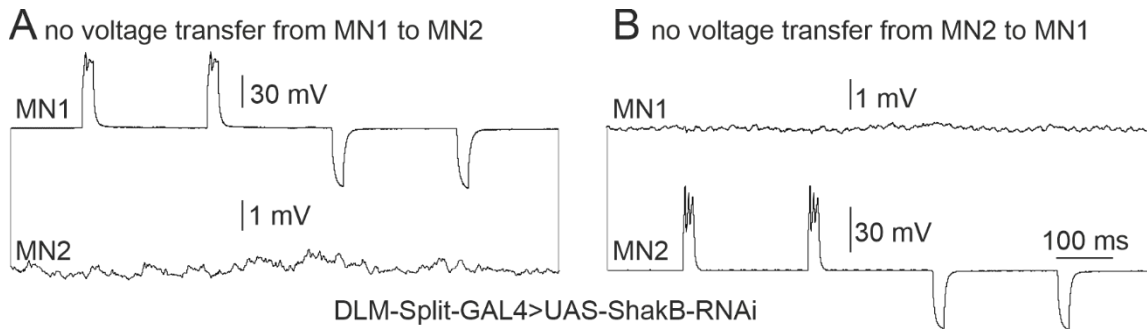
Figure 44: *ShakB* RNAi diminishes the coupling potential. **A** The membrane potential change by current injection in MN1 is not transferred to MN2, which can also be seen vice versa in **B**.

3.12 Using PARIS to measure electrical coupling strength between motoneurons was not feasible

The phase histograms of different MN pairs show different coupling strengths, with phase histograms with wider exclusion bands representing a stronger inhibition. MN pair 1 and 2 and MN pair 3 and 4 show stronger inhibition. We wanted to directly measure the coupling strength for multiple MN pairs to confirm the assumption the width of the exclusion band corresponds to the coupling strength. One way to measure coupling strength between cells is the method PARIS (**p**airing **a**ctuators and **r**eceivers to optically **is**olate gap junctions). For this genetic tool, a light gated proton pump (ArchT) and a pH sensitive GFP (pHluorin CAAX) is expressed cell specific via the UAS-GAL4 system. When ArchT is activated at its specific wavelength of 561 nm, protons are pumped into the actuator cell and diffuse through the gap junctions into coupled cells. In these receiver cells the pH changed and the fluorescence of pHluorin increases. Depending on the coupling strength, the fluorescence changes accordingly (Fig. 45A; Wu et al., 2019). Applied to our MN network, this would mean that if both ArchT and pHluorin are expressed in MN1-5 and stimulate one MN, the fluorescence should increase in all MNs, with one MN showing an even stronger increase. If MN1 is stimulated, MN2 should have a strong fluorescence change, and if MN3 is stimulated MN4 should have a strong fluorescence change (Fig. 45B). Unfortunately, it was not possible to elicit strong fluorescence changes in the coupled neurons and it was difficult to have the MNs in a common focal plane, so it was decided to not pursue this method further.
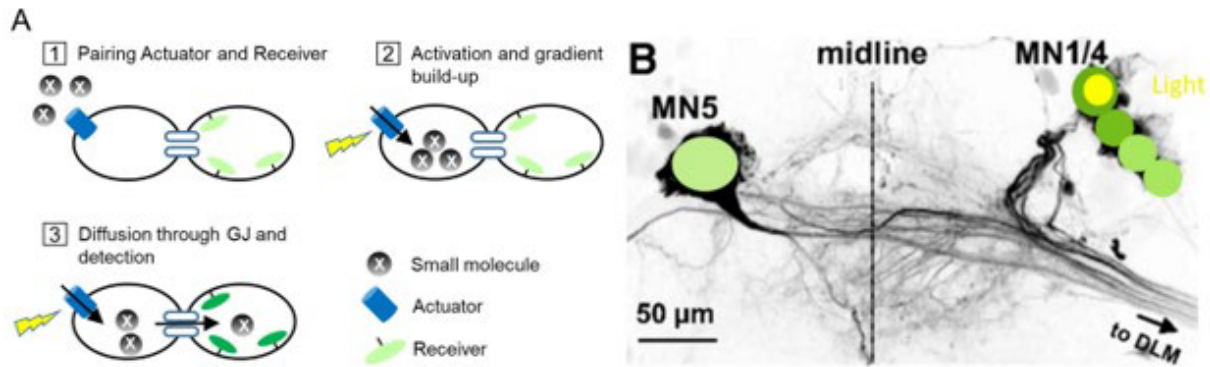
Figure 45: A One cell is expressing a light activated proton pump (ArchT in blue) and is coupled to another cell expressing a pH sensitive GFP (pHluorin in green) (1). When the pump is activated, it carries protons into the actuator cell (2) and the protons are diffusing into the coupled receiver cell (3). The GFP is changing its fluorescence (Wu et al. 2019). **B** If MN1-5 would express ArchT and pHluorin and one MN is stimulated with light (in yellow light), the other MNs should change their fluorescence (green) and one strong coupled MN should have a stronger fluorescence than the rest of the weaker coupled MNs. MN image from Stefanie Ryglewski.

3.13 Muscle spikes are largely calcium carried and explain the splayed state pattern

After having established how electrical coupling is responsible for the firing pattern, the Ca^{2+} dynamics in the muscle fiber can be investigated to determine its influence on the firing pattern. Muscle spikes, unlike neuronal Aps, are largely carried by calcium. Because of the striking influence of Ca^{2+} in an asynchronous muscle as described in the introduction, the $[Ca^{2+}]$ time constant in the DLM muscle should provide information about the resulting $[Ca^{2+}]$ over time during MN firing in the splayed state. Therefore, the $[Ca^{2+}]$ was measured via a synthetical Ca^{2+} indicator, GCaMP. GFP is combined with calmodulin, which alters the conformation of the protein complex upon Ca^{2+} binding, resulting in fluorescence.

The $[Ca^{2+}]$ decay time constant was derived by imaging the myoplasmic calcium signal in the DLM muscle fibers during electronical stimulation. When the GCaMP variant GCaMP7s or GCaMP7f were expressed in the DLM, the time constants were as fast as the time constants of GCaMP7s or GCaMP7f itself (Dana et al., 2019). The experiment was repeated with the latest variant to date, GCaMP8f (Zhang et al., 2023) and a time constant of 79 ±13 ms was measured, which again is corresponding to the time constant of GCaMP itself, (Fig. 46B).

The muscle potential in the DLM has two time constants, as shown by a representative muscle potential with a τ_{fast} of 1.2 ms and τ_{slow} of 14 ms (Fig. 46A, recorded by Christopher Bell). Additionally, the decay of the wingbeat frequency drop was

measured, that occurs in flies overexpressing ShakB. There, the MNs synchronize and the wingbeat fluctuates in phase with the firing of the MNs (Fig. 26). The time constant for the wingbeat is 83 ±27 ms and is therefore strikingly close to the $[Ca^{2+}]$ decay (Fig.46C).
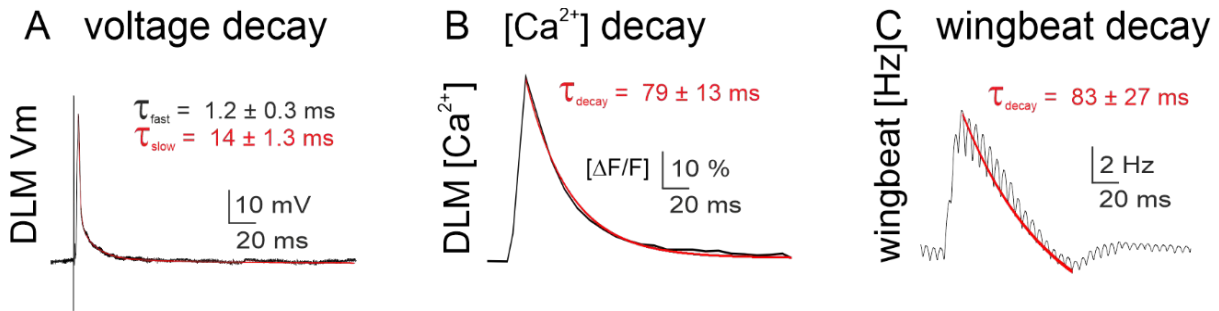
Figure 46: DLM **m**uscle voltage, DLM $[Ca^{2+}]$ and wingbeat frequency time constants. **A** The voltage decay during one evoked muscle potential in a DLM fiber in current clamp has two time constants with a τ_{fast} = 1.2 ms and τ_{slow} 14 ms. Recording from Christopher Bell. **B** The synthetic Calcium indicator GCaMP8f has a τ of 79 ms in the DLM muscle. **C** A wingbeat frequency spike in a ShakB overexpression has a τ of 83 ms.

To understand the relevance of myoplasmic Ca^{2+} dynamics in the DLM during different firing frequencies, the Ca^{2+} signal was recorded in an animal expressing the GCaMP8f variant in the asynchronous muscles. A tungsten electrode was inserted into the DLM fiber 6 of an animal pinned down in a sylgard dish. Then the muscle fiber is stimulated with an increasing frequency (Fig. 47A). Ising stimulation frequencies of 0.5 and 1 Hz, every single stimulation is visible and the fluorescence is returning to a common baseline. From 2 Hz, the signals no longer return to baseline, and the new steady state of minimal fluorescence during tonic stimulation continues to increase further. In the following, the Ca^{2+} signal is extrapolated to derive the average $[Ca^{2+}]$ over the muscle fibers. In a splayed state with five MNs, the average $[Ca^{2+}]$ shows five peaks per cycle (Fig. 47B, blue). In contrast, in a synchronous state,
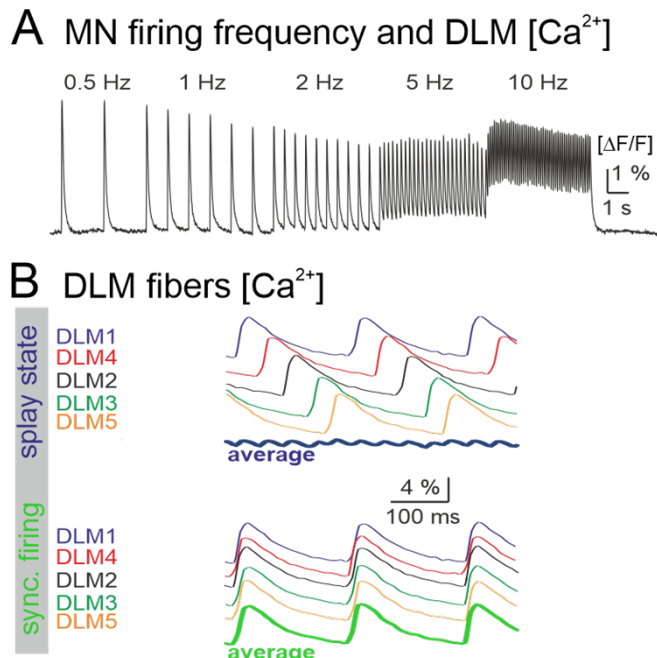
Figure 47: The myoplasmic Ca^{2+} dynamics explain firing frequency and splay state. **A** The Ca^{2+} signal within DLM 6 when stimulated with increasing frequency with a tungsten electrode in an animal expressing the GCaMP8f variant in the DLM. With 5 Hz the Ca^{2+} signal is reaching a new minimal steady state and is increasing further at 10 Hz. **B** An extrapolation of the Ca signal in a splayed state creates a far less fluctuating average Ca^{2+} level over all muscle fibers in comparison to firing during synchronous firing. (Hürkey et al.,2023)

there is only one peak per cycle, and the average amplitude across the fibers shows a fivefold increase in amplitude (Fig. 47B, green) as compared to the splayed state (Fig. 47B, blue).

3.14 Weak electrically coupled neurons of the saddle homoclinic orbit (HOM) excitability class lead to a desynchronized firing pattern

To gain a deeper mechanistic understanding of how electrical synapses desynchronize MN firing in the minimal CPG we collaborated with the computational neurophysiology group of Susanne Schreiber to combine our experimental data with their mathematical models and theory. A previous work already incorporated experimental data from Stefanie Ryglewski into a conductance based single MN model (Berger & Crook, 2015). This model was used as a starting point. This model was used as a starting point. Nelson Niemeyer and Jan-Hendrik Schleimer coupled five of these motoneuron models to create a network model simulating the behavior of the whole MN network. The original model was defined over a range of Shab channel densities. Analyzing the single neuron model revealed for a part of this Shab channel density range, the model showed a specific excitability class named HOM (saddle homoclinic orbit). Based on the theory of phase oscillators Jan-Hendrik Schleimer and Nelson Niemeyer hypothesized HOM excitability to be suitable for creating splay states in the MN network. As explained in the introduction, according to their onset bifurcation neurons fall into three excitability classes: the subcritical Hopf (Hopf), the saddle-node-on-an-invariant cycle (SNIC) and the saddle homoclinic orbit (HOM). One major distinguishing criterion between these excitability classes is the phase response curve of these neurons (Fig. 48, PRCs with blue, purple and green background). Ideally one would confirm the HOM excitability class by PRC estimation *in vivo*. This is typically done repeatedly delivering a small excitatory perturbation in different phases to a regularly firing neuron and the resulting time shift of the following spike. However, this is not possible for the DLM-MNs because they can only be recorded from their somata, and somatic current injection causes prominent spike frequency adaptation, so that it is not possible to keep the neurons firing at a constant rate. Therefore, we cannot be sure that the PRC is really of the HOM type in vivo, but all data presented below favor the idea that the MNs are of this excitability class.
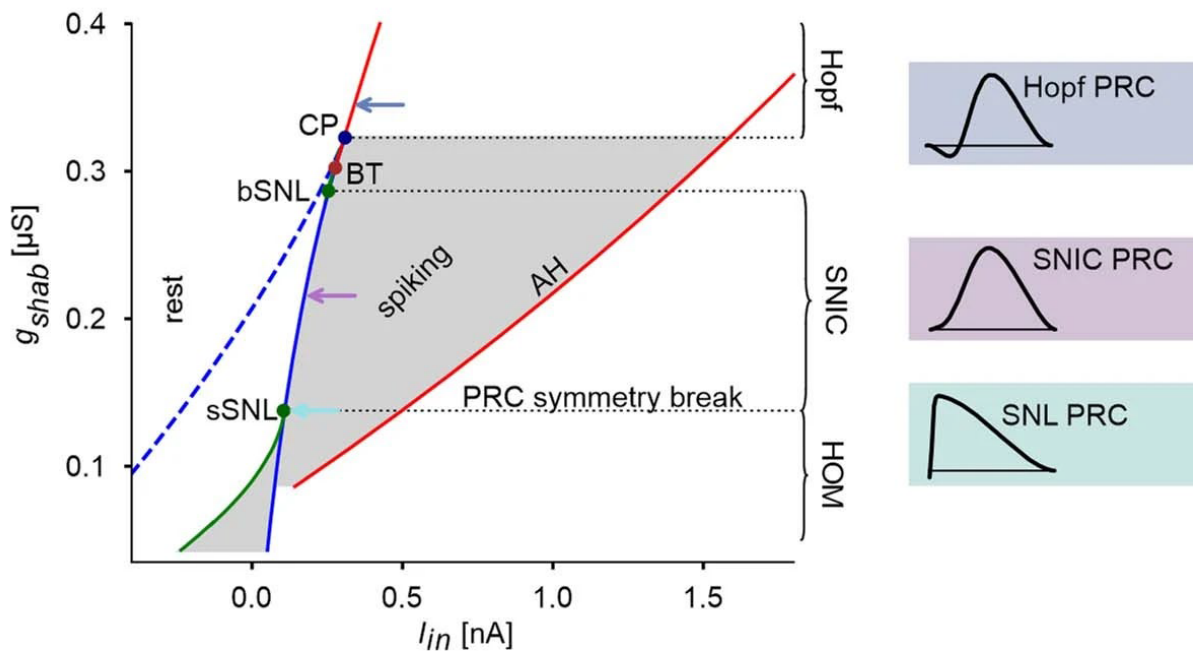
Figure 48: Bifurcation diagram of the MN model showing bifurcations and changing PRCs (SNL, SNIC and Hopf) with different Shab conductance levels (y-axis). The grey area indicates where the neuron is spiking and the colored lines the different bifurcations. The green line for the saddle homoclinic loop (HOM) meets the blue line for the saddle-node loop at the small saddle node loop point (sSNL). With increasing g_{shab} the blue line ends in the big saddle node loop (bSNL) and this section between sSNL and bSNL is the saddle node loop on invariant cycle (SNIC) interval. In this interval the model neuron has a SNIC PRC (PRC with purple background). The red line shows the Adronov-Hopf (AH) bifurcation and ends in the Bogdanov-Takens (BT) point. The red line above the cusp (CP) has a Hopf PRC (PRC with blue background) attributed. The model neuron has a SNL PRC (PRC with green background) in the HOM area near the sSNL point, which favors desynchronized firing states and changes to synchronized firing at the PRC symmetry break, where the SNIC interval begins. (Hürkey et al., 2023).

Next, 5 single MN models were connected by gap junctions based on our *in vivo* recordings (see Fig. 49). For this, a neuron model at the edge of the HOM region, near the so-called saddle-node loop point (SNL) was chosen, where the neuron model combines the characteristic asymmetric HOM PRC shape with other favorable properties (e.g., monostability, shape of fI curve). This network model was then used to test whether a minimal CPG of electrically coupled MNs can produce splayed-out motor patterns. Bidirectional, non-rectifying gap junctions with linear charge transfer were used as found *in vivo* (Fig. 42), but coupling strength was systematically varied in the model.

When isoform weak electrical coupling (CC=0.05) is added to the model the network is firing in a splayed state as found *in vivo* (Fig. 49AB). In a parameter sweep with increasing CCs the splayness index (a quantitative measure for how splayed-out the five MNs fire, see methods) of the network changes drastically. For an uncoupled network (CC=0), a wide variety of splayness indices can occur with a mean of slightly above 0.5. Therefore, in the model, gap junctions even weaker than found *in vivo* do

not produce full network splayness. When the CC is increased from 0.01 to 0.05 (still weak, but as found *in vivo*, see Fig.42) a fully splayed-out state is achieved (splayness index=1). Intermediate coupling with 0.05 to 0.21 leads to increasing synchronization on average. Dependent on the initiation state of the network strong synchronization can already occur. Above a CC of 0.21 the strong coupling synchronizes the network robustly, independent of initiation state (Fig. 49C). Therefore, in the model weak electrical coupling is sufficient to produce full splayness.

To compare the firing pattern of the model and the experimental data from genetic manipulations where only two MNs were recorded, the splayness index cannot be calculated (see methods). Therefore, we defined the synchronization index (see methods) to be able to compare simulations to *in vivo* data with recordings from two neurons only. We calculated a synchronization index, which is a value between 0 and 1; with 0 representing maximal splayness, whereas 1 represents complete synchronization. Weak electrical coupling (CC=0.05 to 0.21) that caused full network splayness in the model (see above) yields a synchronization index of slightly above 0.5 (Fig. 48, green), which is also true for the *in vivo* recordings in control flies (Fig. 48, purple). Please note that for full network splayness the synchronization index cannot be 0, because in a network of 5 electrically coupled neurons not all pairs can be in full antiphase. In the knockdown of *shakB* the synchronization index as measured from *in vivo* data is slightly above the control. However, as shown above, *in vivo*, the overexpression of ShakB leads to a significant increase of the synchronization index (median=0.84, range from ~0.55-1). Similarly, in the model a strong CC leads to robust synchronization. Therefore, the modeling data show that weak electrical coupling between all 5 motoneurons is sufficient to produce network desynchronization, and model predictions for altered CCs are confirmed by *in vivo* measurements. This raises the questions for the mechanism by which electrical synapses desynchronize a small network of coupled neurons?

For the desynchronizing effect of weak electrical coupling the neurons the membrane dynamics of the individual neurons are crucial. In particular, the combination of weak electrical coupling and HOM excitability (near the SNL point) is sufficient to produce splay states. This class has an asymmetric PRC which favors antiphase firing in pairs of electrically coupled of neurons, visible by the fixpoint (black dot) in the odd part of coupling graph (Fig. 49E, bottom right). In networks of more than two neurons, not all

pairs can fire in antiphase, which creates a so-called frustrated system. Here, the splay state represents a low-frustration solution that determines the most probable network state. The excitability class depends among other parameters on the conductance level of the Shab channel (depicted by the gray triangle). The increase of Shab levels in the model transforms spike shape, PRC and odd part of coupling, resulting in the SNIC (saddle node on an invariant cycle) excitability class. This class has a symmetric PRC leading to a fixpoint at phase zero during tonic firing in a network and therefore synchronous firing (Fig. 49E middle column). An even further increase of the Shab level leads to the Hopf class with a nearly symmetric PRC around phase 0.5 resulting again in a fixpoint at 0 and synchronous firing (Fig. 49E left column). This theoretical causality of the increase of Shab level to increased synchronicity motivates the prediction that an overexpression of the Shab level *in vivo* would generate more synchronous spikes. To test this prediction from theory Stefanie Ryglewski generated a fly line with a UAS-Shab construct, by inserting the *Shab* cDNA (gifted by F. Sigworth) into the pJFRC81 vector (for further detail see Hürkey et al., 2023). When the UAS-Shab fly line is crossed with the DLM-MN driver line and record the MNs we have an increased synchronization as predicted. For an example a short section of a recording of MN3+4 is shown, where 8 consecutive synchronous spikes occur with a control on top for comparison (Fig. 49G).

The quantification reveals this difference in the synchronization index is significant (p-value=0.0434 with a two-sided Mann-Whitney U-test), where the median of the control is 0.43 and higher for the Shab overexpression with 0.52 (Fig. 49H). In the model the difference between the SNL and SNIC class is highly significant different with a value of ~0.25 to 1 respectively (Fig. 49H). To test whether the Shab channel is indeed overexpressed patch clamp recordings were made and indeed they show about twice the Shab current in comparison to control (Fig. 49F). Therefore, we can confirm the prediction made by the network model that the increase of g_{shab} also increases the synchronization index and changes the excitability class from HOM through the SNL point into the SNIC or even Hopf class, where weak electrical coupling leads to a synchronized firing state (Fig. 49E). Another crucial test for the model was to investigate if heterogenous coupling of the MNs lead to preferred splay-states. Relative increase of the CC between MN1+2 and MN3+4 (Fig. 49I) generates the two preferred firing patterns, which are also seen in the experimental data (Fig 49J, right). Homogenous electrical coupling causes no preferred sequence (Fig. 49J, left).

In summary the computational modeling allowed us to find a mechanism where weak electrical coupling with bidirectional and non-rectifying gap junctions have a desynchronizing effect. This is the case when neurons of the HOM excitability class are coupled. Additionally increasing the coupling strength of some MN pairs leads to preferred firing patterns.
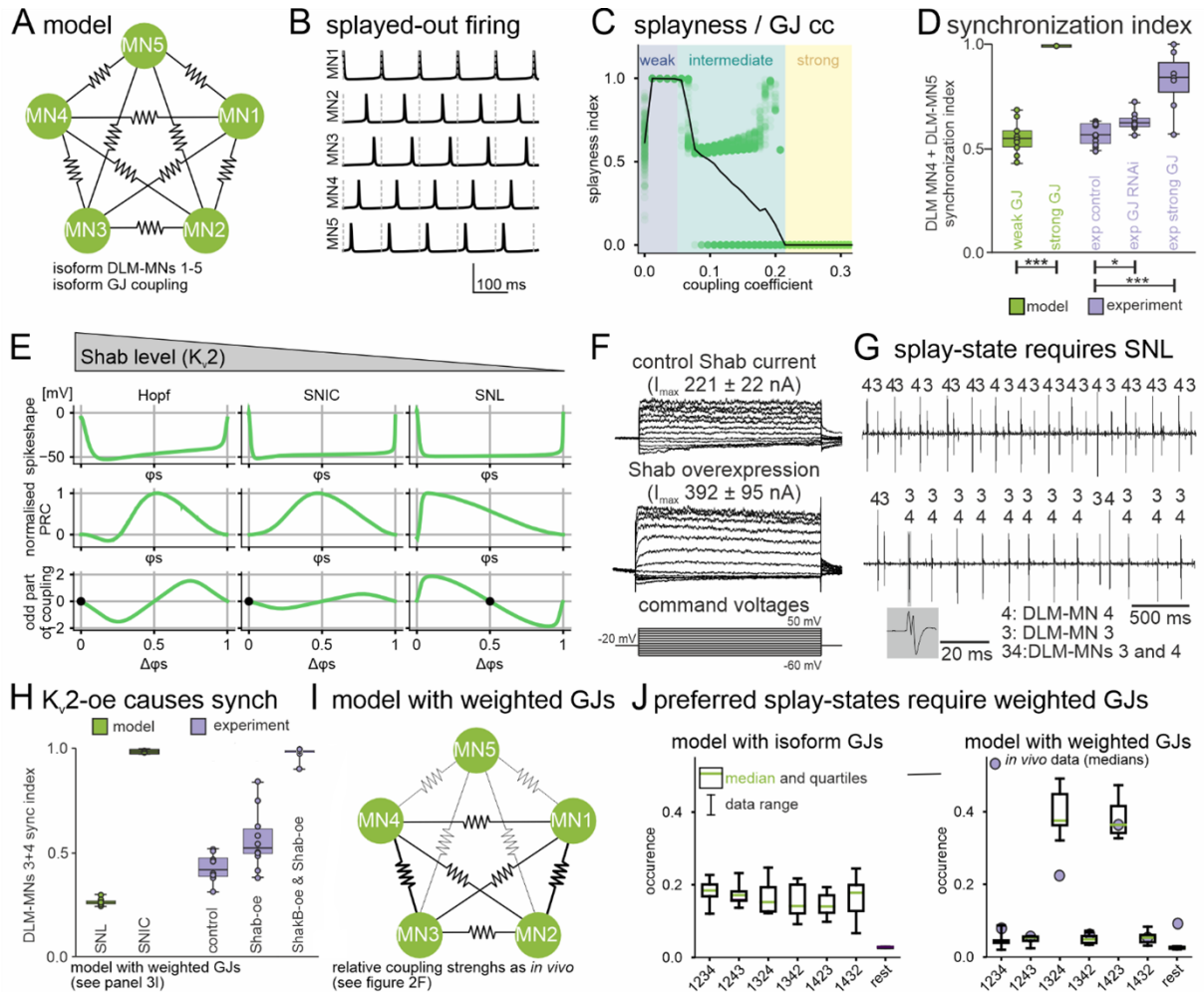
Figure 49: A 3D conductance based computational model of a network of five weakly coupled SNL neurons produces splay state firing. **A** Isoform weak electrical coupling of 5 neurons generate a frustrated network with desynchronized firing (**B**). **C** A CC of 0 generates a wide variety of splayness indices slightly above 0.5 in average, when increased from 0.01 to 0.05 the index increases to 1 meaning desynchronized firing. Intermediate coupling 0.05 to 0.21 leads to increasing synchronized firing and strong coupling above 0.21 to robust synchronized firing with a splayness index of 0. **D** Quantification of the synchronization index of MN4 and MN5 shows a significant increase from weak (CC=0.005) to strong (CC=0.258) coupling in the model (green). For experimental data the synchronization index is significantly increased for the *shakB* knockdown in comparison to the control (Mann-Whitney test p) and highly significant increased for the ShakB(N+16) overexpression. **E** Three excitability classes are possible for this model, which show distinct spike shapes (top row), PRCs (middle) and odd parts of coupling with different fixpoints. The fixpoint (black dot) in the SNL class at phase 0.5 leads to desynchronized firing, owed to the asymmetric PRC. An increase of Shab levels shifts the excitability class form SNL to SNIC to Hopf. **F** A Shab overexpression has nearly twice the Shab current amplitude. **G** The Shab overexpression leads to increased synchronized firing for MN3 and 4. **H** Quantification shows a highly significant increase of the synchronization index (1) for the SNIC class compared to SNL (~0.25) in the model, but also for the experimental data the index is increased for the Shab overexpression (oe) (Median=0.52) and ShakB and Shab oe (Median=0.998) compared to control (Median=0.43). **I** When the relative coupling strength of MN3+ 4 and MN1+2 is increased as the measured CCs suggest, the SNL neurons generate the same preferred firing patterns as *in vivo* (**J**, right), which is not the case for isoform coupling (**J**, left) (Hürkey et al., 2023).

Furthermore, we pursued to verify the prediction of the computational model by combining the overexpression of the potassium channel Shab with the overexpression of ShakB. Both overexpressions have a synchronizing effect as explained above and could potentiate each other if combined. This would reflect in the phase histogram as a synchronization of the network would be expected and accordingly an increase of synchronous spikes. I supervised the Bachelor thesis of Annemarie Krauß, where she recorded MN3 and MN4 in flies with the overexpression of ShakB and Shab. And indeed, in the recordings 90 to 100% (mean=98.3%) of the spikes synchronize which can be seen in the phase histogram, where spikes only occur in the two bins around 0 (Fig. 50). The median of the synchronization index of MN3+4 for the ShakB and Shab overexpression is 0.998 and only one value is with 0.90 under 0.987 (Fig. 49 H).
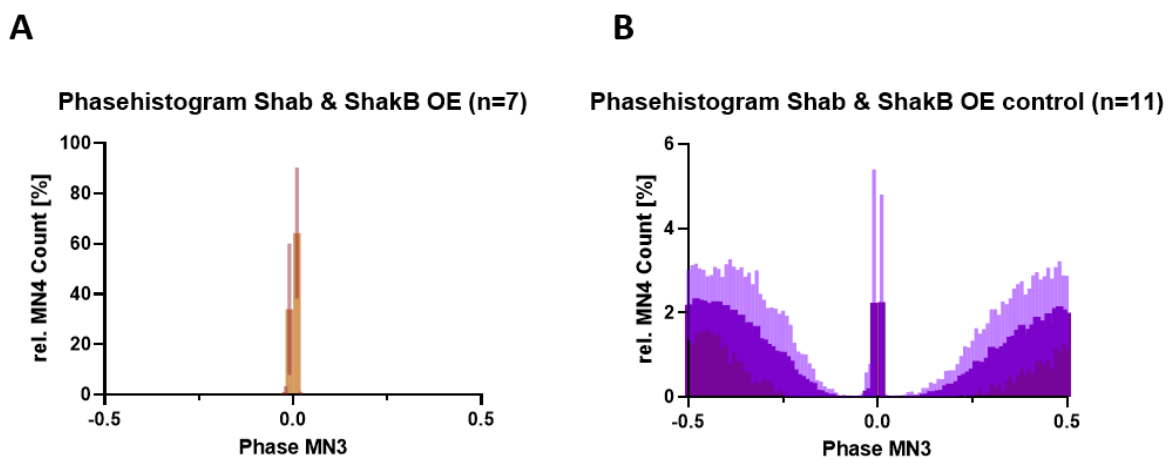
Figure 50: Phase histograms of MN4 to MN3 in an UAS-Shab & UAS-ShakB overexpression and control. **A** In the phase histogram of the double overexpression of Shab and ShakB nearly all spikes are synchronous, since only the two bins around 0 show spikes. **B** The control phase histogram shows 4% of synchronous spikes in the two bins around 0 and a clear band of no near synchronous spikes between the synchronous spikes and ±0.2 in the phase (Bachelor thesis by Annemarie Krauß).

The strong synchronization influences the wingbeat frequency stability, while the overall MN firing frequency and wingbeat frequency is not significantly different (Bachelor thesis Annemarie Krauß). The wingbeat frequency fluctuates ~18 Hz around the firing time point when a MN fires (Fig. 51, brown line) while the control changes only ~1 Hz (Fig. 51, purple line). Therefore, the double overexpression of Shab and ShakB has a stronger effect on the splay state and the wingbeat frequency stabilization, than the two overexpressions on its own. This finding fits into the model since both manipulations push the MN network firing to a synchronized state.
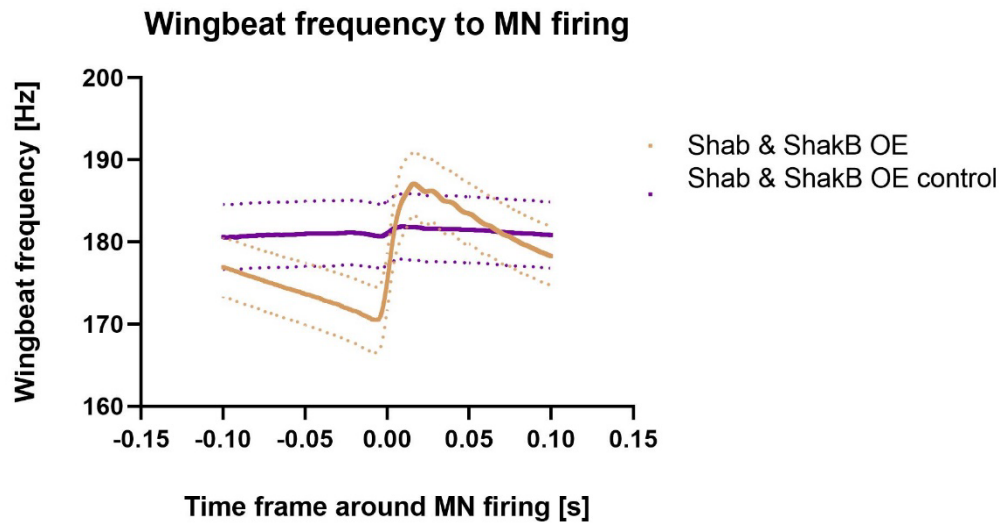
Figure 51: The wingbeat frequency fluctuates ~18 Hz in a double overexpression of Shab and ShakB (brown) around the firing time point of a MN. In control (purple) the wingbeat frequency fluctuates ~1 Hz. (Bachelor thesis by Annemarie Krauß).

4 Discussion

4.1 The DLM-MNs are electrically coupled by gap junctions encoded by the *shakB* gene

Koenig and Ikeda first proposed the idea of electrical coupling to be the reason for the splayed-out firing pattern of the MNs (Koenig & Ikeda, 1980b). A concurrent interval correlation analysis showed some spikes appear sooner than predicted. This pointed to an excitatory effect, which was not in line with the hypothesis of chemical inhibitory synapses to set the phase relationships between MNs. Based on this observation they hypothesized electrical synapses to shape the splay state, but out-of-phase firing was difficult to reconcile with electrical coupling. Our first approach to show electrical coupling between the MNs was to test for dye coupling, which we normally do not find (personal communication Stefanie Ryglewski). Upon the expression of dfmrp1 RNAi in the MNs the dye coupling effect is increased. In *dfmrp1* null mutants the uptake of small tracer dyes is strongly elevated. "Neuronal coupling" via *shakB* encoded electrical synapses is apparently not the reason for an increase in dye coupling, since the dye transfer persists in a *shakB*[2]-null mutant (Kennedy & Broadie, 2017). We can show dye coupling between the five MNs of *Drosophila melanogaster*, which was previously demonstrated for the MNs in *Calliphora erythrocephala* (Schlurmann & Hausen, 2007). We could detect dye coupling of the two MNs5 across both hemiganglia. Schlurmann and Hausen could also show dye coupling between DLM-MNs to their homologues of the other side, but also from the DVM-MNs to the DLM-MNs, but not in the other direction. This indicates not only the 10 DLM-MNs are coupled but also the DVM-MNs (Schlurmann & Hausen, 2007). An attractive hypothesis is electrical coupling across the two hemiganglia and between DLM and DVM-MNs could serve to coordinate the firing frequencies and patterns for both wings and antagonistic flight power muscles. Schlurmann and Hausen also announced intracellular recordings of the MNs in *Calliphora*, which was never published.

By electrophysiological characterization of the coupling between MN pairs via *in situ* patch clamp recordings, we can confirm and characterize the electrical coupling. The electrical synapses are bidirectional non-rectifying and abolished when *shakB* is knocked down with RNAi. In *Xenopus* oocytes expressing single ShakB isoforms, homotypic channels of ShakB(N+16) are non-rectifying, whereas heterotypic channels of ShakB(N+16) and ShakB(L) and homotypic ShakB(L) showed a voltage dependent

conductance (Phelan et al., 2008). Taken together with our finding that the overexpression of the ShakB(N+16) variant had an effect on the phase relation of the firing pattern, but not the knockdown of ShakB(N) or ShakB(L), the gap junctions are mostly formed by homotypic ShakB(N+16) channels.

Although the coupling coefficients (CCs) between MN pairs are weak (0.01-0.02) compared to what is typically found for electrical synapses (0.02-0.2, Alcami, Pereda, 2019) specific pairs of MNs show a twice as strong CC (~ 0.02) than the other pairs (~ 0.01). This fits the coupling strength that can be deducted from phase histograms, where MN1+2 and MN3+4 are stronger coupled than the remaining combinations. MN5 is excluded since it was not included for patch clamp recordings, because of its contralateral location. The stronger interactions between the stronger coupled MN pairs could be an artifact of the anatomical circumstances, because the axons of MN1 and MN2 as well as MN3 and MN4 share a longer distance directly in contact to one another, where interactions could take place, as suggested by Koenig and Ikeda (Koenig & Ikeda, 1980b). Consequently, there would be axonal gap junctions, but these are commonly used for synchronization (Alcamí & Pereda, 2019). We do not know where the gap junctions are localized. A protein trap fly line with a tagged ShakB was nonfunctional. In sum, we can confirm the prediction of Koenig and Ikeda that the MNs are coupled by weak electrical synapses with different weights.

4.2 Gap junctions control the MN firing pattern and relationships and consequently stabilize the wingbeat frequency

In control animals the DLM-MNs fire in a splayed-out state with no near synchronous firing to one another. RNAi knockdown of *shakB* in DLM-MNs causes a change in the firing relationship between the MNs and near synchronous firing occurs, visible in phase histograms. Additionally, firing patterns no longer have preferred sequences and change more frequently. When the ShakB(N+16) isoform is overexpressed in the DLM-MNs, far more synchronous spikes occur, but near synchronous firing is not visible. In time periods with synchronized spikes the wingbeat frequency is fluctuating concurrently. This becomes more pronounced with genetic manipulations that cause synchronous firing throughout long parts of a flight bout (Fig. 26) and demonstrates the stabilizing function of the desynchronized firing pattern on the wingbeat frequency and

thus power output. The wingbeat fluctuations can be further increased, when ShakB(N+16) and Shab are both overexpressed and the MN firing synchronization is stronger (Fig. 51). The consequences of these strong wingbeat fluctuations on flight performance, especially during free flight, are still to be investigated. It could be expected that flies with these wingbeat fluctuations have difficulties to fly precise maneuvers or fast saccades. Flies make saccades by small differences between the inside and the outside wing of only ~5° in wingbeat amplitude (Fry et al., 2003). Also pitch torque could be impaired, which is achieved by changing the upstroke-to-downstroke duration ratio during a wingbeat cycle (Fry et al., 2005). This ratio could be changed, because only the DLM-MNs (downstroke) are synchronized, but not the DVM-MNs (upstroke).

4.3 Desynchronized firing pattern as a common feature of asynchronous insect flight

We can show that electrical coupling is responsible for the desynchronization of the MN network to produce a motor program for an even wingbeat power output in *Drosophila melanogaster*. Similar phase histograms of the firing relationships of DLM-MNs for other species indicate that this motor program is likely a common feature. This desynchronized firing pattern of the DLM-MNs was already described in 1963 in *Musca domestica* and *Eucaliphora lilae* (D. M. Wilson & Wyman, 1963), 1965 in *Calliphora terraenovae* (Wyman, (R. Wyman, 1965) and in 1968 in *Apis mellifera* (Esch & Bastian, 1968). In *Drosophila melanogaster* it was first characterized in 1973 by Levine and Wyman (J. Levine, 1973). We can confirm the desynchronized firing pattern for *Apis mellifera*, *Calliphora spec., Drosophila hydei* and *Musca domestica*. Histograms of MN5 and MN4 show a dip around zero, which correlates with the splayness of a network and is therefore an indicator for splayed-out firing (Hürkey et al., 2023). Our tested insect species are part of the order Diptera (*Calliphora terraenovae*, *Drosophila melanogaster*, *Drosophila hydei, Eucaliphora lilae*, *Musca domestica*) and Hymenoptera (*Apis mellifera*). Both orders are part of the superorder Holometabola. In total there are at least 7 orders where asynchronous flight should have developed independently (Cullen, 1974; Deora et al., 2017). The orders Coleoptera and Strepsiptera are also part of the superorder Holometabola. Thysanoptera, Hemiptera and Psocodea are insect orders of the superorder Hemipterodea and are also

asynchronous flyers. It would be interesting to record the MN activity in insect species of the superorder Hemipterodea to test whether the MN activity is also desynchronized. I tried to record multiple other species, but most insect species could not be convinced to fly when tethered.

For *Drosophila* the firing pattern of the five MNs is described in further detail, where we know there is a preferred sequence, which is also the case for our findings. We have one recording of all five MNs in *Calliphora spec*, but also for this species the same phase histograms and preferred firing sequence 1432 as in *Drosophila melanogaster* can be observed. This could indicate the preferred firing sequence as a more common feature of asynchronous muscles in insect flight.

4.4   The preferred firing pattern could be advantageous for an efficient translation of MN firing to wingbeat frequency

The analysis for the different patterns shows no obvious indication as to whether the preferred sequence 1432 is functionally important, in the sense of providing a clear advantage over the other possible sequences. The preferred firing sequence could grant the ideal Ca^{2+} gradient over the muscle group to induce the best possible power output, thus resulting in a high wingbeat frequency. In three animals with 10 min recordings only one animal shows the highest wingbeat frequency during the preferred sequence 1432. However, when we compensate for the firing frequency and sort the patterns into two frequency bins within a 5 Hz range (25-30 Hz and 30-35 Hz) the preferred firing sequence has the highest wingbeat frequency 5 out of 6 times. And in the one case where it is not, the second most preferred firing sequence has the highest wingbeat frequency (Fig. 37). This may indicate that indeed the preferred firing sequence allows for the most effective translation of MN firing into wingbeat frequency and is thus energetically optimal. One interesting aspect of the two preferred sequences is that the pattern is always jumping between the pair NN1/2 and MN3/4, which should be caused by stronger coupling between these MN pairs. But how could electrical synapses cause desynchronization?

4.5 Desynchronization of the MN activity by weak electrical coupling and the HOM excitability class

Electrical synapses are commonly used to synchronize neural networks (Alcamí & Pereda, 2019; Connors, 2017). However electrical synapses have previously been described in other CPGs, where neurons are desynchronized, but they are not the reason for the desynchronization. One prominent mechanism to desynchronize neuronal activity of electrically coupled neurons are inhibitory chemical synapses. Therefore, when these chemical synapses are pharmacologically blocked the activity synchronizes. In the pyloric network of the STG, the PD, AB and VD neurons are electrically coupled and the AB neuron is inhibiting the VD neuron via chemical synapses. Consequently, the PD and AB neuron fire synchronously while VD is inhibited and fires asynchronously. When the AB neuron with the inhibitory chemical synapses is removed the VD neuron begins to fire in synchrony with the PD (Marder, 1984). By changing the strength of the two opposing characteristics of synchronizing electrical synapses and desynchronizing inhibitory chemical synapses through neuromodulation, different degrees of synchronization can be achieved (Johnson et al., 1993; Marder, 1984; Marder et al., 2017).

However, there is one example in the literature, where electrical synapses cause a transient desynchronization of network activity. In goldfish short out-of-phase stimulation of mossy fibers presynaptic to the golgi cells causes a transient desynchronization of a previously synchronous active network. Dendritic gap junctions cause the inhibition by the stronger CC of the presynaptic slow AHP as compared to the short spike overshoot (Vervaeke et al., 2010). We also find an increased CC for the AHP and have the same CC of 0.2 between the stronger coupled MN pairs 1+2 and 3+4. However, the GJ mediated desynchronization of the golgi cell network requires a short, out-of-phase patterned input and results only in transient desynchronization. These are fundamental differences to our network. In the flight CPG the input can be unpatterned, since the optogenetic manipulation of the cholinergic input as well as in the MNs themselves had no influence on the synchronicity. Consequently, it has to be generated by the MNs themselves. Second, the flight CPG shows permanent desynchronization during splay state firing. Therefore, the mechanism described in golgi cells cannot explain the input independent and tonic desynchronization in the flight CPG.

Theoretical work has previously pointed to the possibility of desynchronization through weak electrical coupling (Sherman & Rinzel, 1992), but experimental evidence and mechanistic biological insight has been lacking (Connors, 2017).

Another mechanism by which electrical synapse could mediate an inhibiting effect is rectifying gap junctions. Following heterologous expression of different ShakB isoform combinations pre- and postsynaptically can result in both heterotypic and homotypic channels. Heterotypic channels with ShakB(L) and ShakB(N+16) create rectifying channels, while homotypic ShakB(N+16) create non-rectifying channels (Phelan et al., 2008). Similar to rectification, electrical synapses could be asymmetric meaning the conductance from one cell to another is dependent on the direction of current (Sevetson & Haas, 2015). However, dual patch clamp recordings of electrically coupled DLM-MNs reveal no rectification and no asymmetry in coupling. Instead, *shakB* mediated electrical synapses between DLM-MNs are non-rectifying, bidirectional, and weak with linear charge transfer. Experimental evidence for desynchronization by non-rectifying, bi-directional electrical synapses alone is not present to our knowledge as is also stated by Connors, 2017.

Instead, we find that weak non-rectifying, bi-directional electrical synapses can be desynchronizing if the coupled neurons exhibit a specific membrane excitability profile, namely a homoclinic (HOM) spike-onset near the saddle-node loop (SNL) bifurcation. The phase response curves of our conductance-based DLM-MN model with fast sodium currents and delayed rectifier potassium currents, based on *in situ* current and voltage clamp recordings, reveal a HOM excitability. Connecting these HOM type DLM-MN single neuron models into a network model with reciprocal electrical synapses demonstrates weak electrical coupling is sufficient to produce a splay state. A parameter sweep for the CC showed that the synchronization state indeed depends on the coupling strength and only weak coupling is able to produce desynchronization, which is in line with our in vivo experiments, where overexpression of ShakB in DLM-MNs significantly increases firing synchrony. Please note that the DLM-MN models do not show a pronounced AHP, ruling out a requirement for the AHP for desynchronization. Nonetheless, it must be considered that the electrophysiological recordings showing the low pass filtering characteristics, enabling a stronger transmission of the AHP should result in an inhibitory effect. But this finding is not in contradiction to the model and could stabilize the splay state even further (personal

communication Nelson Niemeyer and Jan-Hendrik Schleimer). In conclusion, in small networks of electrically coupled neurons in the HOM excitability class, weak electrical synapses are sufficient to produce a splay state. Mathematical analysis provides an analytical solution that explains this desynchronization mechanism. For a specific network state (synchronized or desynchronized) the so-called coupling function is decisive because it combines the PRC and the electrical coupling. Stable fix points of the odd part of the coupling function at phase 0.5 resemble desynchronized network states and result only from weak electrical coupling of neurons with a HOM PRC (Fig. 49E). By contrast, more symmetric PRCs (SNIC and Hopf) yield stable fixpoints at phase 0, resembling synchronized network states. Therefore, our theoretical approaches yield a generic mechanism for small network desynchronization by weak electrical synapses. Since this theory predicts that the same electrical synapses must yield network synchronization in the case of coupled neurons with symmetric PRCs, such as SNIC, this implies the same electrical synapses can cause network desynchronization or synchronization, depending on the dynamic excitability profile of the coupled neurons. We test this theoretical prediction experimentally *in vivo*.

PRC analyses of the single DLM-MN model led us to the prediction that an overexpression of the Shab channel should transform the neurons from HOM type to SNIC type excitability profiles. Unfortunately, the PRC of the single DLM-MNs *in vivo* cannot be measured, because this requires measuring the impact of small membrane potential perturbation at different phases of the interspike interval on the timing of the subsequent spike. Experimentally, this requires inducing tonic firing at a given rate for prolonged periods of time and testing the effects of small and brief current injections at random times. However, *in situ*, tonic firing can only be induced by somatic current injection, but DLM-MNs show spike frequency adaptation in this experiment, thus not allowing for rigorous PRC measurements. Nonetheless, the model clearly predicts that increases in Shab conductance must transform the neurons to SNIC types and thus yield network synchronization. This prediction was tested by overexpression of Shab in DLM-MNs. This indeed confirmed the model prediction and caused significantly increased network synchronization, as reflected in the phase histogram and synchronization index of MN3+4. This is the first experimental demonstration that the same gap junctions can cause network synchronization or desynchronization depending on the membrane excitability profile of the coupled neurons. Moreover, combining the Shab overexpression with the overexpression of the ShakB(N+16)

isoform synchronizes the network nearly completely with 98% of synchronous spikes. Therefore, both manipulations fit the predictions of the model, since both push the network in to a more synchronous firing state, and the combination of both manipulations creates highly robust network synchrony.

4.6 Advantages of electrically coupled neurons

Why are the DLM-MNs using electrical synapses instead of chemical synapses?

Since we find electrical synapses instead of chemical synapses, which are commonly used for desynchronization in CPGs the question arises, do electrical synapses provide an advantage in such a network. While it is highly speculative to address this question, I would like to present some ideas. One possible explanation may derive from small body size. While the surface reduces squared, the volume reduces cubed, therefore the smaller an insect is, the less internal volume is available. Thus, it could be advantageous to minimize the number of neurons in a network. In this case the MNs adopt the function of pattern generating interneurons. It was previously shown that in small insects neurons are indeed multifunctional to reduce the cost of space and energy (Niven & Farris, 2012). At the same time, flight is part of the lifesaving escape response and is elicited by the giant fiber pathway to maximize the speed by which visual cues initiate flight. Reducing the number of chemical synapses within this pathway and a fast motor pattern establishment increases the survivability. Additionally synaptic input is more evenly distributed over the network and noisy input is filtered, establishing a fast steady neuronal activity and therefore power output. For nervous systems a reduction in size increases the signal to noise ratio, since molecular components are not getting smaller, only neurons with less membrane and cellular compartments as synapses (Niven & Farris, 2012). Stochastic events as spontaneous activity have a bigger impact and electrical coupling could counteract this, by increasing the signal to noise ratio (Connors, 2017). At the moment, however, I do not have any conclusive evidence to back up these hypotheses.

4.7 Myoplasmic Ca^{2+} dynamics dictate the splay state

We can show that the time constant of myoplasmic Ca^{2+} decay in the DLM muscle matches that of wingbeat frequency decay after synchronized spikes (~80 ms).

Stimulating the DLM tonically with an increasing frequency leads to a summation of the myoplasmic Ca^{2+} when 2 Hz are reached. Accelerating the frequency further to 10 Hz also increases the minimal Ca^{2+} level, while single Ca^{2+} signals per stimulation remain visible (Fig. 47A). The summation of the myoplasmic Ca^{2+} signal occurs in the working range of the MN firing frequency during flight with 2-15 Hz (Fig. 10C). Since we already know the Ca^{2+} concentration in the DLM has a linear correlation with power output (Gordon & Dickinson, 2006) and an increasing Ca^{2+} concentration is increasing the stretch activatable force in a muscle preparation (Wang et al., 2011), this summation of the myoplasmic Ca^{2+} should be the regulating factor in the power production. Taken together with the fact that synchronous firing of the MNs in flies with the ShakB overexpression leads to stronger fluctuations in the wingbeat frequency, this emphasizes the importance of the MN firing in a splay state to ensure a uniform Ca^{2+} concentration. But we have to acknowledge the sometimes weak or even negative correlation between the MN firing frequency to wingbeat frequency. The use of change of rate instead of the rate increased the correlation but was still low in some cases. The reason could be that we do not take the wingbeat amplitude into account. In Gordon 2006 the wingbeat amplitude seems to correlate stronger with the MN firing rate than the wingbeat frequency. Wingbeat frequency and amplitude are linked, which reflects in the maximal power output of the system. With increasing wingbeat amplitude the wingbeat frequency decreases (Fig. 60, from F.-O. F. Lehmann, 2004). Additionally it could be shown, the wingbeat amplitude correlates with Ca^{2+} concentration in the asynchronous muscle during maneuvering flight (F.-O. Lehmann et al., 2013). These findings lead to the conclusion MN firing frequency influences both wingbeat frequency and amplitude. But only a certain maximal power output is possible and when the wingbeat frequency increases the amplitude has to decrease or vice versa. Accordingly, when only one parameter of wingbeat frequency or amplitude is measured, the correlation to the MN firing frequency is weakened. To have a better read out of the system it would be beneficial to measure the wingbeat amplitude as well. This would allow a better understanding of the splay state and would probably increase the correlation between DLM-MN firing frequency and power output. When the MN firing frequency of the different patterns are compared to the corresponding wingbeat frequency, there was no clear effect. Therefore, one would also have to compensate for the firing frequency, as it was done for the whole pattern, but then there are not enough spikes for a quantification.

The inclusion of the wingbeat amplitude may show different firing pattern having a correlation to the power output. For now, there could be an effect of the sequence on the wingbeat frequency, since the preferred sequence has a higher wingbeat frequency when it is compensated for the firing frequency within a 5 Hz range (25-30 Hz and 30-35 Hz). Another approach could be the reduction of the frequency window. Leading to less spikes per frequency which in turn requires longer recordings.

4.8   The outside role of MN5

It was previously described that MN5 is firing around 10% faster than MN1-4 (Harcombe & Wyman, 1977). In some data sets (Bachelor theses: Andrij Bujnenko, Lea Deneke) we also find a higher firing rate for MN5, but when the firing frequency of 41 control animals is compared, there is no statistical significance (p=0.47, Fig. 52), but a tendency is visible with a mean of 4.9 Hz for MN5 and 4.7 Hz for MN4. However, since it is often a topic of discussion, I want to make a few remarks. MN5 innervates the two most dorsal fibers of the DLM. One explanation could be the volume of these two fibers, assuming every fiber should exert the same force, it should also have the same volume for myofibrils. MicroCT of the DLM reveals, that the DLM5 and 6 have half the volume than every single DLM1-4 (Chaturvedi et al., 2019). So, by linking DLM5+6 with MN5 might allow to compensate for the smaller volume, which might be owed to the dorsal location in the thoracic shell. Another possible explanation for the faster firing rate might be a temperature effect. In hawkmoth there is a temperature gradient within the DLM, where the outer muscle fibers dissipate heat faster and have a lower temperature. A higher temperature allows more force production in muscle and the neuronal activity is compensating for this efficiency loss (George et al., 2012). Maybe this is also the case in *Drosophila* and the higher firing frequency of MN5 compensates for the temperature loss in the outer DLM fibers.

4.9   The desynchronization of a neural network by gap junctions adds a fundamental new function for electrical synapses

This thesis answers the two main questions (originating in the 1960s): How is the motor pattern of the asynchronous flight muscle generated and what is the function of the splay state? Both are answered in a short sentence: "Gap junctions desynchronize a neural circuit to stabilize insect flight" which is also the title of the publication in *Nature*

integrate the main findings of this thesis (Hürkey et al., 2023). By answering these specific biological questions, we were able to find a general novel function for gap junctions with a broader significance for neuroscience.

To process a vast amount of information the brain relies on stable data transfer between neurons via chemical and electrical synapses. The human brain holds about 86 billion neurons, each having chemical synapses in the order of a thousand (Azevedo et al., 2009). Morphological and functional differences, but also the plasticity of chemical synapses are further increasing the complexity and ability to process information (Abbott & Nelson, 2000; Nusser, 2018). Electrical synapses however are often neglected, and functions and prevalence underrated. However, as previously described they are also able to be modified with a diverse functionality and are ubiquitously expressed in the nervous system (Alcamí & Pereda, 2019; Trenholm et al., 2019). The ability of gap junctions to desynchronize a network without the need of inhibitory chemical synapses adds a fundamental new function for electrical synapses. This has broad implications for neural networks in general. The synchronicity of larger networks, as in the brain, might also make use of this function. Whole states of consciousness emerging by different states of synchronicity in brain waves can be influenced.

Additionally, the knowledge of how the flight power is controlled can also help to design better interfaces for radio controlled insects (Sato & Maharbiz, 2010) or inspire biomimetic robots as micro air vehicles (MAVs) or nano air vehicles (NAVs) (Tanaka et al., 2022).

Still, there are countless remaining questions on how the small MN circuit is controlling asynchronous flight. The project is also integrated in the Robust Circuit Research Unit with the leading question how imprecision in dendritic development or ion channel expression in the MN circuit leads to robust flight output.

5 References

Abbott, L. F., & Nelson, S. B. (2000). Synaptic plasticity: Taming the beast. *Nature Neuroscience*, *3*(11s), 1178–1183. https://doi.org/10.1038/81453

Alcamí, P., & Pereda, A. E. (2019). Beyond plasticity: the dynamic impact of electrical synapses on neural circuits. *Nature Reviews Neuroscience*, *20*(5), 253–271. https://doi.org/10.1038/s41583-019-0133-5

Ammer, G., Vieira, R. M., Fendl, S., & Borst, A. (2022). Anatomical distribution and functional roles of electrical synapses in Drosophila. *Current Biology*, 1–15. https://doi.org/10.1016/j.cub.2022.03.040

Azevedo, F. A. C., Carvalho, L. R. B., Grinberg, L. T., Farfel, J. M., Ferretti, R. E. L., Leite, R. E. P., Filho, W. J., Lent, R., & Herculano-Houzel, S. (2009). Equal numbers of neuronal and nonneuronal cells make the human brain an isometrically scaled-up primate brain. *Journal of Comparative Neurology*, *513*(5), 532–541. https://doi.org/10.1002/cne.21974

Barthmaier, P., & Fyrberg, E. (1995). Monitoring Development and Pathology of Drosophila Indirect Flight Muscles Using Green Fluorescent Protein. *Developmental Biology*, *169*(2), 770–774. https://doi.org/10.1006/dbio.1995.1186

Bauer, R., Löer, B., Ostrowski, K., Martini, J., Weimbs, A., Lechner, H., & Hoch, M. (2005). Intercellular communication: The Drosophila innexin multiprotein family of gap junction proteins. In *Chemistry and Biology* (Vol. 12, Issue 5, pp. 515–526). https://doi.org/10.1016/j.chembiol.2005.02.013

Belanger, J. H. (2005). Contrasting Tactics in Motor Control by Vertebrates and Arthropods. *Integrative and Comparative Biology*, *45*(4), 672–678. https://doi.org/10.1093/icb/45.4.672

Berger, S. D., & Crook, S. M. (2015). Modeling the Influence of Ion Channels on Neuron Dynamics in Drosophila. *Frontiers in Computational Neuroscience*, *9*(November), 1–20. https://doi.org/10.3389/fncom.2015.00139

Bloomfield, S. A., & Völgyi, B. (2009). The diverse functional roles and regulation of neuronal gap junctions in the retina. *Nature Reviews Neuroscience*, *10*(7), 495–506. https://doi.org/10.1038/nrn2636

Boerner, J., & Godenschwege, T. A. (2010). Application for the Drosophila Ventral Nerve Cord Standard in Neuronal Circuit Reconstruction and In-Depth Analysis of Mutant Morphology. *Journal of Neurogenetics*, *24*(3), 158–167. https://doi.org/10.3109/01677063.2010.489624

Brodfuehrer, P. D., Debski, E. A., O'Gara, B. A., & Friesen, W. O. (1995). Neuronal control of leech swimming. *Journal of Neurobiology*, *27*(3), 403–418. https://doi.org/10.1002/neu.480270312

Brown, T. G. (1911). The intrinsic factors in the act of progression in the mammal. *Proceedings of the Royal Society of London. Series B, Containing Papers of a Biological Character*, *84*(572), 308–319. https://doi.org/10.1098/rspb.1911.0077

Bussel, B., Roby-brami, A., Azouvi, P. H., Biraben, A., Yakovleff, A., & Held, J. P. (1988). Myoclonus in a patient with spinal cord transection: Possible involvement of the spinal stepping generator. *Brain*, *111*(5), 1235–1245.

https://doi.org/10.1093/brain/111.5.1235

Cao, T., & Jin, J.-P. (2020). Evolution of Flight Muscle Contractility and Energetic Efficiency. *Frontiers in Physiology*, *11*(October), 1–14. https://doi.org/10.3389/fphys.2020.01038

Chaturvedi, D., Prabhakar, S., Aggarwal, A., Atreya, K. B., & VijayRaghavan, K. (2019). Adult Drosophila muscle morphometry through microCT reveals dynamics during ageing. *Open Biology*, *9*(6), 190087. https://doi.org/10.1098/rsob.190087

Coggshall, J. C. (1978). Neurons associated with the dorsal longitudinal flight muscles of Drosophila melanogaster. *Journal of Comparative Neurology*, *177*(4), 707–720. https://doi.org/10.1002/cne.901770410

Connors, B. W. (2017). Synchrony and so much more: Diverse roles for electrical synapses in neural circuits. *Developmental Neurobiology*, *77*(5), 610–624. https://doi.org/10.1002/dneu.22493

Cullen, M. J. (1974). The distribution of asynchronous muscle in insects with particular reference to the Hemiptera: an electron microscope study. *Journal of Entomology Series A, General Entomology*, *49*(1), 17–41. https://doi.org/10.1111/j.1365-3032.1974.tb00064.x

Dana, H., Sun, Y., Mohar, B., Hulse, B. K., Kerlin, A. M., Hasseman, J. P., Tsegaye, G., Tsang, A., Wong, A., Patel, R., Macklin, J. J., Chen, Y., Konnerth, A., Jayaraman, V., Looger, L. L., Schreiter, E. R., Svoboda, K., & Kim, D. S. (2019). High-performance calcium sensors for imaging activity in neuronal populations and microcompartments. *Nature Methods*, *16*(7), 649–657. https://doi.org/10.1038/s41592-019-0435-6

David, C. T. (1978). The relationship between body angle and flight speed in free-flying Drosophila. *Physiological Entomology*, *3*(3), 191–195. https://doi.org/10.1111/j.1365-3032.1978.tb00148.x

Dawydow, A., Gueta, R., Ljaschenko, D., Ullrich, S., Hermann, M., Ehmann, N., Gao, S., Fiala, A., Langenhan, T., Nagel, G., & Kittel, R. J. (2014). Channelrhodopsin-2-XXL, a powerful optogenetic tool for low-light applications. *Proceedings of the National Academy of Sciences*, *111*(38), 13972–13977. https://doi.org/10.1073/pnas.1408269111

Delcomyn, F. (1980). Neural Basis of Rhythmic Behavior in Animals. *Science*, *210*(4469), 492–498. https://doi.org/10.1126/science.7423199

Deora, T., Gundiah, N., & Sane, S. P. (2017). Mechanics of the thorax in flies. *The Journal of Experimental Biology*, *220*(8), 1382–1395. https://doi.org/10.1242/jeb.128363

DeVries, S. H., Qi, X., Smith, R., Makous, W., & Sterling, P. (2002). Electrical coupling between mammalian cones. *Current Biology*, *12*(22), 1900–1907. https://doi.org/10.1016/S0960-9822(02)01261-7

Dickinson, M. H., Lehmann, F.-O., & Chan, W. A. I. P. (2016). The Control of Mechanical Power in Insect Flight. *American Zoologist*, *38*(4), 718–728. http://www.jstor.org/stable/4620197

Dickinson, M. H., & Muijres, F. T. (2016). The aerodynamics and control of free flight

manoeuvres in Drosophila. *Philosophical Transactions of the Royal Society B: Biological Sciences*, *371*(1704), 20150388. https://doi.org/10.1098/rstb.2015.0388

Dudley, R. (2000). The Evolutionary Physiology of Animal Flight: Paleobiological and Present Perspectives. *Annual Review of Physiology*, *62*(1), 135–155. https://doi.org/10.1146/annurev.physiol.62.1.135

Enoka, R. M., & Duchateau, J. (2017). Rate coding and the control of muscle force. *Cold Spring Harbor Perspectives in Medicine*, *7*(10), 1–12. https://doi.org/10.1101/cshperspect.a029702

Esch, H., & Bastian, J. (1968). Mechanical and electrical activity in the indirect flight muscles of the honey bee. *Zeitschrift Für Vergleichende Physiologie*, *58*(4), 429–440. https://doi.org/10.1007/BF00343515

Fabian-Fine, R., Meisner, S., Torkkeli, P. H., & Meinertzhagen, I. A. (2015). Co-localization of Gamma-Aminobutyric Acid and Glutamate in Neurons of the Spider Central Nervous System. *Cell and Tissue Research*, *362*(3), 461–479. https://doi.org/10.1007/s00441-015-2241-5

Flamm, R. E., & Harris-Warrick, R. M. (1986a). Aminergic modulation in lobster stomatogastric ganglion. I. Effects on motor pattern and activity of neurons within the pyloric circuit. *Journal of Neurophysiology*, *55*(5), 847–865. https://doi.org/10.1152/jn.1986.55.5.847

Flamm, R. E., & Harris-Warrick, R. M. (1986b). Aminergic modulation in lobster stomatogastric ganglion. II. Target neurons of dopamine, octopamine, and serotonin within the pyloric circuit. *Journal of Neurophysiology*, *55*(5), 866–881. https://doi.org/10.1152/jn.1986.55.5.866

Fouquet, W., Owald, D., Wichmann, C., Mertel, S., Depner, H., Dyba, M., Hallermann, S., Kittel, R. J., Eimer, S., & Sigrist, S. J. (2009). Maturation of active zone assembly by Drosophila Bruchpilot. *Journal of Cell Biology*, *186*(1), 129–145. https://doi.org/10.1083/jcb.200812150

Fry, S. N., Sayaman, R., & Dickinson, M. H. (2003). The Aerodynamics of Free-Flight Maneuvers in Drosophila. *Science*, *300*(5618), 495–498. https://doi.org/10.1126/science.1081944

Fry, S. N., Sayaman, R., & Dickinson, M. H. (2005). The aerodynamics of hovering flight in Drosophila. *Journal of Experimental Biology*, *208*(12), 2303–2318. https://doi.org/10.1242/jeb.01612

George, N. T., Sponberg, S., & Daniel, T. L. (2012). Temperature gradients drive mechanical energy gradients in the flight muscle of Manduca sexta. *Journal of Experimental Biology*, *215*(3), 471–479. https://doi.org/10.1242/jeb.062901

Gordon, S., & Dickinson, M. H. (2006). Role of calcium in the regulation of mechanical power in insect flight. *Proceedings of the National Academy of Sciences of the United States of America*, *103*(11), 4311–4315. https://doi.org/10.1073/pnas.0510109103

Guertin, P. A. (2009). The mammalian central pattern generator for locomotion. *Brain Research Reviews*, *62*(1), 45–56. https://doi.org/10.1016/j.brainresrev.2009.08.002

Harcombe, E. S., & Wyman, R. J. (1977). Output pattern generation by Drosophila flight motoneurons. *Journal of Neurophysiology*, *40*(5), 1066–1077. https://doi.org/10.1152/jn.1977.40.5.1066

Harcombe, E. S., & Wyman, R. J. (1978). The cyclically repetitive firing sequencess of identified Drosophila flight motoneurons. *Journal of Comparative Physiology*, *123*(3), 271–279. https://doi.org/10.1007/BF00656881

Holmes Bullock, T. (1961). The Origins of Patterned Nervous Discharge. *Behaviour*, *17*(1), 48–58. https://doi.org/10.1163/156853961X00358

Holtzman, S., Kaufman, T. (2013). *Large-scale imaging of Drosophila melanogaster mutations.*

Hürkey, S., Niemeyer, N., Schleimer, J., Ryglewski, S., Schreiber, S., & Duch, C. (2023). Gap junctions desynchronize a neural circuit to stabilize insect flight. *Nature*, *618*(7963), 118–125. https://doi.org/10.1038/s41586-023-06099-0

Izhikevich, E. (2007). *Dynamical systems in neuroscience*. MIT Press.

Jankowska, E., Jukes, M. G. M., Lund, S., & Lundberg, A. (1967). The Effect of DOPA on the Spinal Cord 6. Half-centre organization of interneurones transmitting effects from the flexor reflex afferents. *Acta Physiologica Scandinavica*, *70*(3–4), 389–402. https://doi.org/10.1111/j.1748-1716.1967.tb03637.x

Jenett, A., Rubin, G. M., Ngo, T. T. B., Shepherd, D., Murphy, C., Dionne, H., Pfeiffer, B. D., Cavallaro, A., Hall, D., Jeter, J., Iyer, N., Fetter, D., Hausenfluck, J. H., Peng, H., Trautman, E. T., Svirskas, R. R., Myers, E. W., Iwinski, Z. R., Aso, Y., … Zugates, C. T. (2012). A GAL4-Driver Line Resource for Drosophila Neurobiology. *Cell Reports*, *2*(4), 991–1001. https://doi.org/10.1016/j.celrep.2012.09.011

Johnson, B. R., Peck, J. H., & Harris-Warrick, R. M. (1993). Amine modulation of electrical coupling in the pyloric network of the lobster stomatogastric ganglion. *Journal of Comparative Physiology A*, *172*(6), 715–732. https://doi.org/10.1007/BF00195397

Josephson, R. K., Malamud, J. G., & Stokes, D. R. (2000). Asynchronous muscle: a primer. *The Journal of Experimental Biology*, *203*(Pt 18), 2713–2722. http://www.ncbi.nlm.nih.gov/pubmed/10952872

Katz, P. S. (2016). *Evolution of central pattern generators and rhythmic behaviours*. https://doi.org/10.1098/rstb.2015.0057

Kennedy, T., & Broadie, K. (2017). Fragile X Mental Retardation Protein Restricts Small Dye Iontophoresis Entry into Central Neurons. *The Journal of Neuroscience*, *37*(41), 9844–9858. https://doi.org/10.1523/JNEUROSCI.0723-17.2017

Koenig, J. H., & Ikeda, K. (1980a). Interspike interval relationship among flight muscle fibres in Drosophila. *The Journal of Experimental Biology*, *87*(1), 137–147. http://jeb.biologists.org/content/jexbio/87/1/137.full.pdf

Koenig, J. H., & Ikeda, K. (1980b). Neural interactions controlling timing of flight muscle activity in Drosophila. *Journal of Experimental Biology*, *87*(1), 121–136. https://doi.org/10.1242/jeb.87.1.121

Koenig, J. H., & Ikeda, K. (1983). Reciprocal excitation between identified flight motor

neurons in Drosophila and its effect on pattern generation. *Journal of Comparative Physiology*, *150*(3), 305–317. https://doi.org/10.1007/BF00605020

Kondo, S., & Ueda, R. (2013). Highly Improved gene targeting by germline-specific Cas9 expression in Drosophila. *Genetics*, *195*(3), 715–721. https://doi.org/10.1534/genetics.113.156737

Kristan, W. B., Calabrese, R. L., & Friesen, W. O. (2005). Neuronal control of leech behavior. *Progress in Neurobiology*, *76*(5), 279–327. https://doi.org/10.1016/j.pneurobio.2005.09.004

Kuehn, C., & Duch, C. (2013). Putative excitatory and putative inhibitory inputs are localised in different dendritic domains in a Drosophila flight motoneuron. *European Journal of Neuroscience*, *37*(6), 860–875. https://doi.org/10.1111/ejn.12104

Lawson, K. K. K., & Srinivasan, M. V. (2017). Flight control of fruit flies: dynamic response to optic flow and headwind. *The Journal of Experimental Biology*, *220*(11), 2005–2016. https://doi.org/10.1242/jeb.153056

Lehmann, F.-O. F. (2004). Muscle Systems Design and Integration. *Nature's Versatile Engine: Insect Flight Muscle Inside and Out*, 1–12. http://www.springerlink.com/index/p1832w6788478713.pdf

Lehmann, F.-O., Skandalis, D. A., & Berthé, R. (2013). Calcium signalling indicates bilateral power balancing in the Drosophila flight muscle during manoeuvring flight. *Journal of the Royal Society, Interface / the Royal Society*, *10*(82), 20121050. https://doi.org/10.1098/rsif.2012.1050

Levine, J. (1973). Properties of the nervous system controlling flight in Drosophila melanogaster. *Journal of Comparative Physiology*, *84*(2), 129–166. https://doi.org/10.1007/BF00697603

Levine, J. D., & Hughes, M. (1973). Stereotaxic map of the muscle fibers in the indirect flight muscles ofDrosophila melanogaster. *Journal of Morphology*, *140*(2), 153–158. https://doi.org/10.1002/jmor.1051400203

Lindsay, T., Sustar, A., & Dickinson, M. (2017). The Function and Organization of the Motor System Controlling Flight Maneuvers in Flies. *Current Biology*, *27*(3), 345–358. https://doi.org/10.1016/j.cub.2016.12.018

Lundberg, A. (1965). Interaction between the spinal reflex pathways. *Actualites Neurophysiologiques*, *6*. https://pubmed.ncbi.nlm.nih.gov/5857824/

Marder, E. (1984). Roles for electrical coupling in neural circuits as revealed by selective neuronal deletions. *The Journal of Experimental Biology*, *112*, 147–167. http://jeb.biologists.org/content/jexbio/112/1/147.full.pdf

Marder, E., & Bucher, D. (2007). Understanding Circuit Dynamics Using the Stomatogastric Nervous System of Lobsters and Crabs. *Annual Review of Physiology*, *69*(1), 291–316. https://doi.org/10.1146/annurev.physiol.69.031905.161516

Marder, E., & Calabrese, R. L. (1996). Principles of rhythmic motor pattern generation. *Physiological Reviews*, *76*(3), 687–717. https://doi.org/10.1152/physrev.1996.76.3.687

Marder, E., Gutierrez, G. J., & Nusbaum, M. P. (2017). Complicating connectomes: Electrical coupling creates parallel pathways and degenerate circuit mechanisms. *Developmental Neurobiology*, *77*(5), 597–609. https://doi.org/10.1002/dneu.22410

Matsunaga, T., Kohsaka, H., & Nose, A. (2017). Gap Junction–Mediated Signaling from Motor Neurons Regulates Motor Generation in the Central Circuits of Larval Drosophila. *The Journal of Neuroscience*, *37*(8), 2045–2060. https://doi.org/10.1523/JNEUROSCI.1453-16.2017

Medici, V., & Fry, S. N. (2012). Embodied linearity of speed control in Drosophila melanogaster. *Journal of The Royal Society Interface*, *9*(77), 3260–3267. https://doi.org/10.1098/rsif.2012.0527

Minassian, K., Hofstoetter, U. S., Dzeladini, F., Guertin, P. A., & Ijspeert, A. (2017). The Human Central Pattern Generator for Locomotion: Does It Exist and Contribute to Walking? *Neuroscientist*, *23*(6), 649–663. https://doi.org/10.1177/1073858417699790

Mizrahi, A., Dickinson, P. S., Kloppenburg, P., Fénelon, V., Baro, D. J., Harris-Warrick, R. M., Meyrand, P., & Simmers, J. (2001). Long-Term Maintenance of Channel Distribution in a Central Pattern Generator Neuron by Neuromodulatory Inputs Revealed by Decentralization in Organ Culture. *The Journal of Neuroscience*, *21*(18), 7331–7339. https://doi.org/10.1523/JNEUROSCI.21-18-07331.2001

Nagarkar-Jaiswal, S., DeLuca, S. Z., Lee, P.-T., Lin, W.-W., Pan, H., Zuo, Z., Lv, J., Spradling, A. C., & Bellen, H. J. (2015). A genetic toolkit for tagging intronic MiMIC containing genes. *ELife*, *4*(8), 085201. https://doi.org/10.7554/eLife.08469

Niven, J. E., & Farris, S. M. (2012). Miniaturization of nervous systems and neurons. *Current Biology*, *22*(9), R323–R329. https://doi.org/10.1016/j.cub.2012.04.002

Nusser, Z. (2018). Creating diverse synapses from the same molecules. *Current Opinion in Neurobiology*, *51*, 8–15. https://doi.org/10.1016/j.conb.2018.01.001

Otopalik, A. G., Lane, B., Schulz, D. J., & Marder, E. (2019). Innexin expression in electrically coupled motor circuits. *Neuroscience Letters*, *695*, 19–24. https://doi.org/10.1016/j.neulet.2017.07.016

Pereda, A. E. (2014). Electrical synapses and their functional interactions with chemical synapses. *Nature Reviews Neuroscience*, *15*(4), 250–263. https://doi.org/10.1038/nrn3708

Perkins, L. A., Holderbaum, L., Tao, R., Hu, Y., Sopko, R., McCall, K., Yang-Zhou, D., Flockhart, I., Binari, R., Shim, H. S., Miller, A., Housden, A., Foos, M., Randkelv, S., Kelley, C., Namgyal, P., Villalta, C., Liu, L. P., Jiang, X., … Perrimon, N. (2015). The transgenic RNAi project at Harvard medical school: Resources and validation. *Genetics*, *201*(3), 843–852. https://doi.org/10.1534/genetics.115.180208

Pézier, A. P., Jezzini, S. H., Bacon, J. P., & Blagburn, J. M. (2016). Shaking B Mediates Synaptic Coupling between Auditory Sensory Neurons and the Giant Fiber of Drosophila melanogaster. *PLOS ONE*, *11*(4), e0152211. https://doi.org/10.1371/journal.pone.0152211

Phelan, P., Bacon, J. P., Davies, J. A., Stebbings, L. A., & Todman, M. G. (1998). Innexins: A family of invertebrate gap-junction proteins. In *Trends in Genetics* (Vol.

14, Issue 9, pp. 348–349). https://doi.org/10.1016/S0168-9525(98)01547-9

Phelan, P., Goulding, L. A., Tam, J. L. Y., Allen, M. J., Dawber, R. J., Davies, J. A., & Bacon, J. P. (2008). Molecular Mechanism of Rectification at Identified Electrical Synapses in the Drosophila Giant Fiber System. In *Current Biology* (Vol. 18, Issue 24, pp. 1955–1960). Elsevier Ltd. https://doi.org/10.1016/j.cub.2008.10.067

Phelan, P., & Starich, T. A. (2001). Innexins get into the gap. *BioEssays*, *23*(5), 388–396. https://doi.org/10.1002/bies.1057

Pons, A., Perl, I., Ben-Dov, O., Maya, R., & Beatus, T. (2023). *Solving the thoracic inverse problem in the fruit fly*.

Port, F., Chen, H. M., Lee, T., & Bullock, S. L. (2014). Optimized CRISPR/Cas tools for efficient germline and somatic genome engineering in Drosophila. *Proceedings of the National Academy of Sciences of the United States of America*, *111*(29). https://doi.org/10.1073/pnas.1405500111

Pringle, J. W. S. (1949). The excitation and contraction of the flight muscles of insects. *The Journal of Physiology*, *108*(2), 226–232. https://doi.org/10.1113/jphysiol.1949.sp004326

Qiu, F., Lakey, A., Agianian, B., Hutchings, A., Butcher, G. W., Labeit, S., Leonard, K., & Bullard, B. (2003). Troponin C in different insect muscle types: identification of two isoforms in Lethocerus, Drosophila and Anopheles that are specific to asynchronous flight muscle in the adult insect. *Biochem. J*, *371*, 811–821. https://doi.org/10.1042/BJ20021814

Rome, L. C., & Lindstedt, S. L. (1998). The quest for speed: muscles built for high-frequency contractions. *News in Physiological Sciences*, *13*(6), 261–268. https://doi.org/10.1152/physiologyonline.1998.13.6.261

Ryglewski, S., & Duch, C. (2012). Preparation of Drosophila Central Neurons for in situ Patch Clamping. *Journal of Visualized Experiments*, *68*. https://doi.org/10.3791/4264

Ryglewski, S., Kadas, D., Hutchinson, K., Schuetzler, N., Vonhoff, F., & Duch, C. (2014). Dendrites are dispensable for basic motoneuron function but essential for fine tuning of behavior. *Proceedings of the National Academy of Sciences*, *111*(50), 18049–18054. https://doi.org/10.1073/pnas.1416247111

Sadava, D., Hillis, D. M., Heller, H. C., Berenbaum, M. R., & Markl, J. (2011). *Purves Biologie* (9. Auflage). Spektrum Akademischer Verlag.

Sato, H., & Maharbiz, M. M. (2010). Recent developments in the remote radio control of insect flight. In *Frontiers in Neuroscience* (Vol. 4, Issue DEC). Ellington Dickinson and Tu. https://doi.org/10.3389/fnins.2010.00199

Schlurmann, M., & Hausen, K. (2007). Motoneurons of the flight power muscles of the blowfly Calliphora erythrocephala: Structures and mutual dye coupling. *The Journal of Comparative Neurology*, *500*(3), 448–464. https://doi.org/10.1002/cne.21182

Selverston, A. I. (2010). Invertebrate central pattern generator circuits. *Philosophical Transactions of the Royal Society B: Biological Sciences*, *365*(1551), 2329–2345. https://doi.org/10.1098/rstb.2009.0270

Sevetson, J., & Haas, J. S. (2015). Asymmetry and modulation of spike timing in electrically coupled neurons. In *Journal of Neurophysiology* (Vol. 113, Issue 6). https://doi.org/10.1152/jn.00843.2014

Sherman, A., & Rinzel, J. (1992). Rhythmogenic effects of weak electrotonic coupling in neuronal models. *Proceedings of the National Academy of Sciences*, *89*(6), 2471–2474. https://doi.org/10.1073/pnas.89.6.2471

Smith, J. C., Abdala, A. P. L., Borgmann, A., Rybak, I. A., & Paton, J. F. R. (2013). Brainstem respiratory networks: Building blocks and microcircuits. *Trends in Neurosciences*, *36*(3), 152–162. https://doi.org/10.1016/j.tins.2012.11.004

Song, J., Ampatzis, K., Björnfors, E. R., & El Manira, A. (2016). Motor neurons control locomotor circuit function retrogradely via gap junctions. *Nature*, *529*(7586), 399–402. https://doi.org/10.1038/nature16497

Stork, N. E. (2018). How Many Species of Insects and Other Terrestrial Arthropods Are There on Earth? *Annual Review of Entomology*, *63*(1), 31–45. https://doi.org/10.1146/annurev-ento-020117-043348

Straight, C. R., Bell, K. M., Slosberg, J. N., Miller, M. S., & Swank, D. M. (2019). A myosin-based mechanism for stretch activation and its possible role revealed by varying phosphate concentration in fast and slow mouse skeletal muscle fibers. *American Journal of Physiology-Cell Physiology*, *317*(6), C1143–C1152. https://doi.org/10.1152/ajpcell.00206.2019

Swank, D. M. (2012). Mechanical analysis of Drosophila indirect flight and jump muscles. *Methods*, *56*(1), 69–77. https://doi.org/10.1016/j.ymeth.2011.10.015

Szentesi, P., Zaremba, R., Van Mechelen, W., & Stienen, G. J. M. (2001). ATP utilization for calcium uptake and force production in different types of human skeletal muscle fibres. *Journal of Physiology*, *531*(2), 393–403. https://doi.org/10.1111/j.1469-7793.2001.0393i.x

Talay, M., Richman, E. B., Snell, N. J., Hartmann, G. G., Fisher, J. D., Sorkaç, A., Santoyo, J. F., Chou-Freed, C., Nair, N., Johnson, M., Szymanski, J. R., & Barnea, G. (2017). Transsynaptic Mapping of Second-Order Taste Neurons in Flies by trans-Tango. *Neuron*, *96*(4), 783-795.e4. https://doi.org/10.1016/j.neuron.2017.10.011

Tanaka, S., Asignacion, A., Nakata, T., Suzuki, S., & Liu, H. (2022). Review of Biomimetic Approaches for Drones. *Drones*, *6*(11), 1–15. https://doi.org/10.3390/drones6110320

Trenholm, S., Ph, D., Awatramani, G. B., & Ph, D. (2019). *Gap junctions in the retina and how they affect receptive field size Photoreceptors*. 1–49.

Vervaeke, K., Lőrincz, A., Gleeson, P., Farinella, M., Nusser, Z., & Silver, R. A. (2010). Rapid Desynchronization of an Electrically Coupled Interneuron Network with Sparse Excitatory Synaptic Input. *Neuron*, *67*(3), 435–451. https://doi.org/10.1016/j.neuron.2010.06.028

Vigoreaux, J. (2006). *Nature s Versatile Engine : Insect Flight Muscle Inside and Out*.

Wang, Q., Zhao, C., & Swank, D. M. (2011). Calcium and stretch activation modulate power generation in Drosophila flight muscle. *Biophysical Journal*, *101*(9), 2207–

2213. https://doi.org/10.1016/j.bpj.2011.09.034

Wegener, G. (1996). Flying insects: Model systems in exercise physiology. In *Experientia* (Vol. 52, Issue 5, pp. 404–412). https://doi.org/10.1007/BF01919307

Wiersma, C. A. G., & Hughes, G. M. (1961). On the functional anatomy of neuronal units in the abdominal cord of the crayfish,Procambarus clarkii (girard). *The Journal of Comparative Neurology*, *116*(2), 209–228. https://doi.org/10.1002/cne.901160209

Wilson, B. Y. D. M. (1961). The Central Nervous Control of Flight in a Locust. *Journal of Experimental Biology*, *38*(2), 471–490.

Wilson, D. M., & Wyman, R. J. (1963). Phasically unpatterned nervous control of dipteran flight. *Journal of Insect Physiology*, *9*(6), 859–865. https://doi.org/10.1016/0022-1910(63)90044-1

Wilson, D. M., & Wyman, R. J. (1965). Motor Output Patterns during Random and Rhythmic Stimulation of Locust Thoracic Ganglia. *Biophysical Journal*, *5*(2), 121–143. https://doi.org/10.1016/S0006-3495(65)86706-6

Wu, L., Dong, A., Dong, L., Wang, S.-Q., & Li, Y. (2019). PARIS, an optogenetic method for functionally mapping gap junctions. *ELife*, *8*, 1–22. https://doi.org/10.7554/eLife.43366

Wyman, R. (1965). Probabilistic Characterization of Simultaneous Nerve Impulse Sequences Controlling Dipteran Flight. *Biophysical Journal*, *5*(4), 447–471. https://doi.org/10.1016/S0006-3495(65)86729-7

Wyman, R. J. (1966). Multistable firing patterns among several neurons. *Journal of Neurophysiology*, *29*(5), 807–833. https://doi.org/10.1152/jn.1966.29.5.807

Wyman, R. J. (1969). Lateral inhibition in a motor output system. I. Reciprocal inhibition in Dipteran flight motor system. *Journal of Neurophysiology*, *32*(3), 297–306. https://doi.org/10.1152/jn.1969.32.3.297

Zhang, Y., Rózsa, M., Liang, Y., Bushey, D., Wei, Z., Zheng, J., Reep, D., Broussard, G. J., Tsang, A., Tsegaye, G., Narayan, S., Obara, C. J., Lim, J. X., Patel, R., Zhang, R., Ahrens, M. B., Turner, G. C., Wang, S. S. H., Korff, W. L., … Looger, L. L. (2023). Fast and sensitive GCaMP calcium indicators for imaging neural populations. In *Nature* (Vol. 615, Issue March). Springer US. https://doi.org/10.1038/s41586-023-05828-9

Zhao, C., & Swank, D. M. (2013). An Embryonic Myosin Isoform Enables Stretch Activation and Cyclical Power in Drosophila Jump Muscle. *Biophysical Journal*, *104*(12), 2662–2670. https://doi.org/10.1016/j.bpj.2013.04.057

6 Acknowledgements

7 Appendix

MN firing frequency
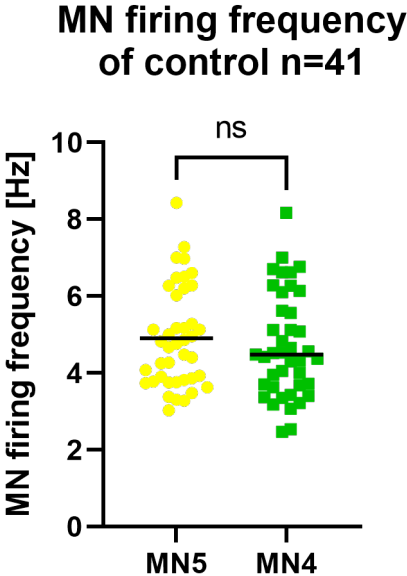## of control n=41

Figure 52: MN firing frequency of control animals of CantonS and Valium pooled. There is no significant difference between MN4 and MN5. Normally distributed (Kolmogorov-Smirnov test), unpaired t test p=0.47.
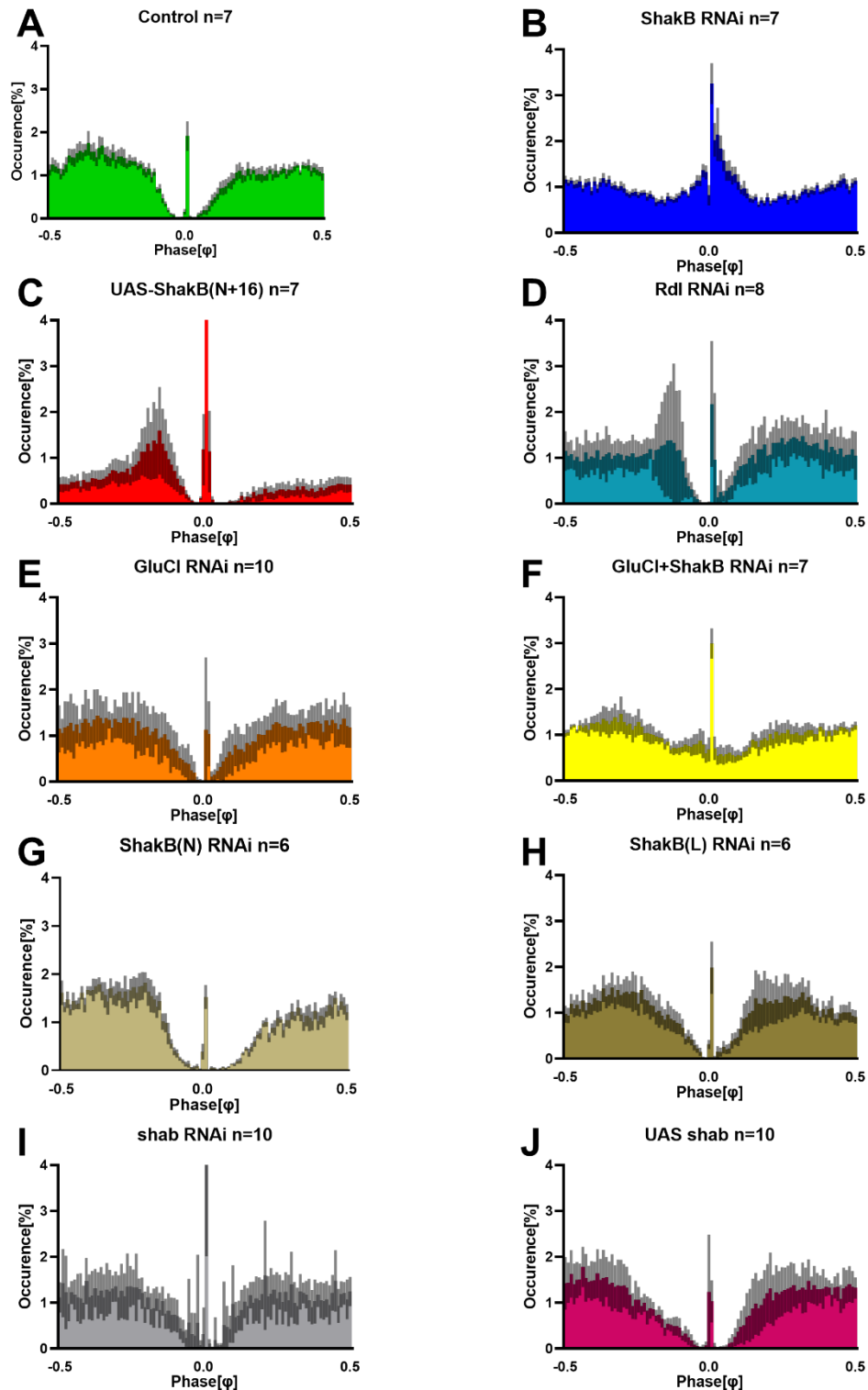
Figure 53: Phase histograms of MN5 to MN4 in different genetic manipulations. **(A)** In VALIUM control animals are short exclusion bands shortly before and after synchronous firing. **(B)** in *shakB* RNAi animals there are no exclusion bands and slightly more synchronous firing. **(C)** The overexpression of the ShakB(N+16) isoform leads to an increase in synchronous but not near synchronous spikes. **(D, E)** Rdl and GluCl knockdowns show exclusion bands, but there is a higher SEM. **(F)** The double knockdown of GluCl and ShakB shows no exclusion bands, but the effect is less strong as in the *shakB* knockdown in **B**. **(G, H)** In single ShakB isoform knockdowns (ShakB(N) and ShakB(L)) exclusion bands are visible. **(I)** The Shab knockdown shows a slight increase of synchronous spikes, but exclusion bands are observable. (J) The overexpression of Shab has no effect in the phase histogram of MN5 and MN4.
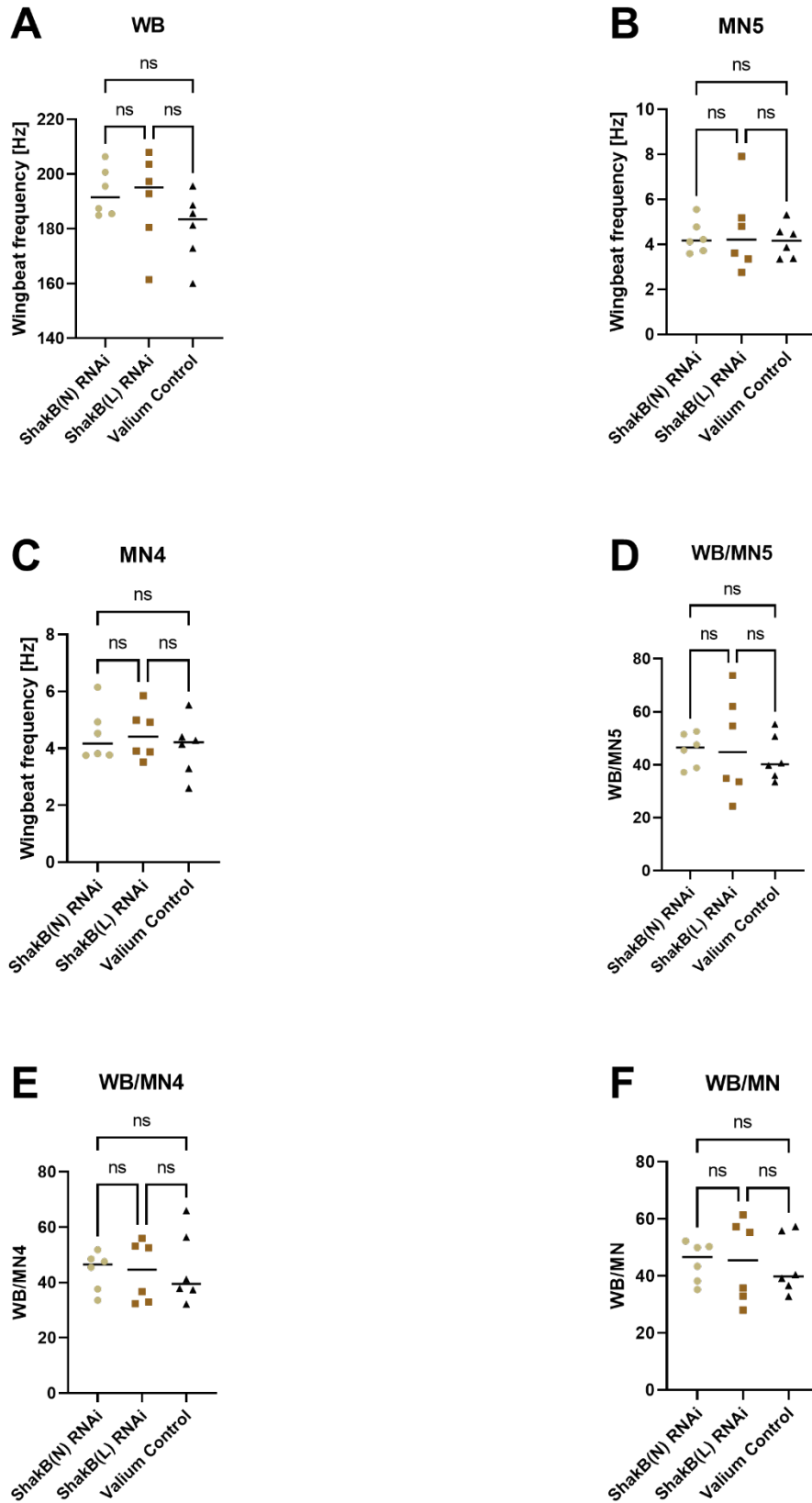
Figure 54: The RNAi knockdown of the ShakB(L) or ShakB(N) isoform has no influence on the wingbeat frequency or MN firing frequency. All data points are normally distributed (Shapiro Wilk test), and one way ANOVA Tukey's multiple comparisons test showed no significant differences. Data were acquired by Tamara Kaufman.
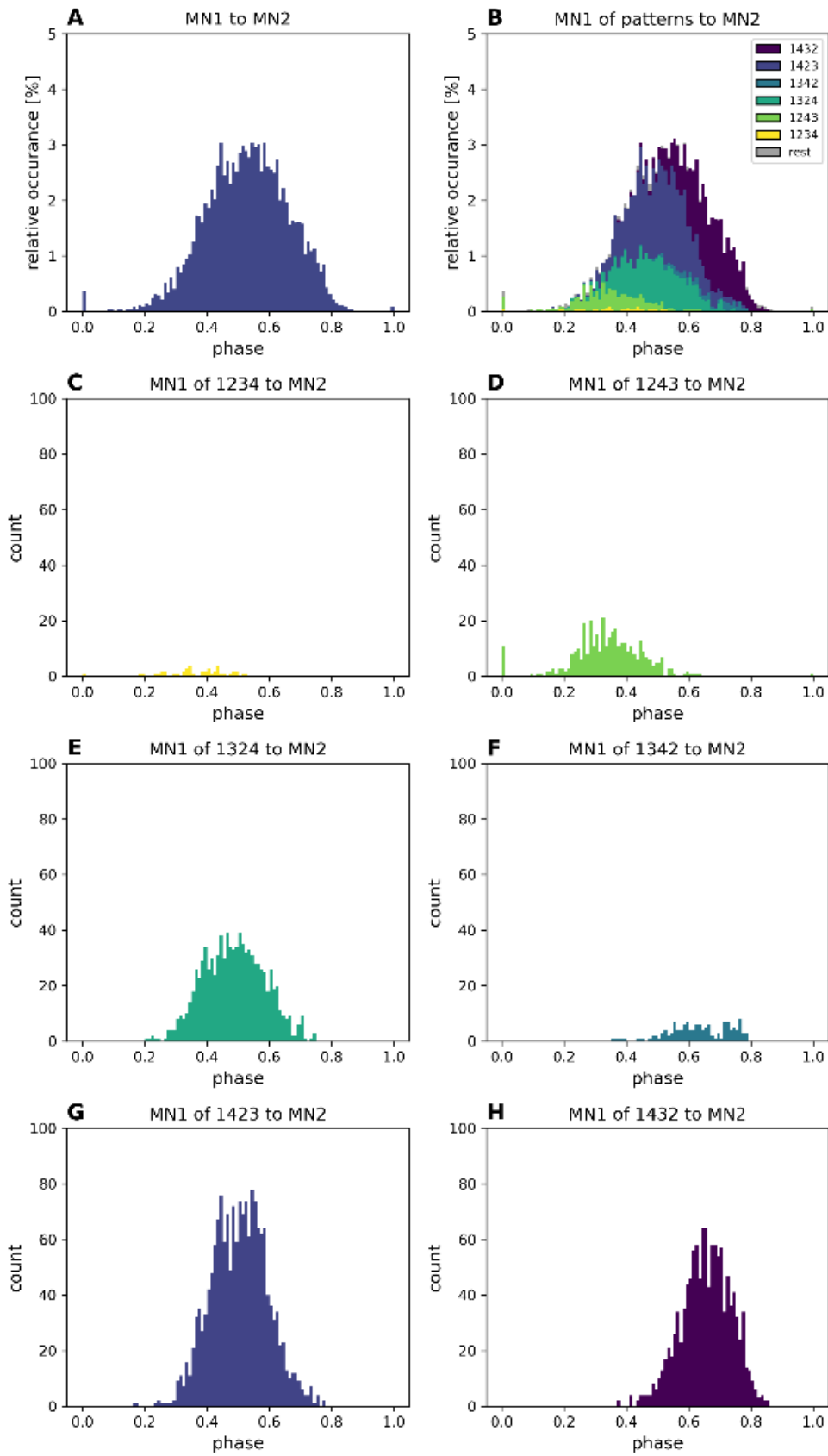
Figure 55: MN firing frequency of different firing patterns in control and *shakB* knockdown. There are more significant differences between MN firing frequencies in control **(A-C)** compared to the *shakB* knockdown **(D-F)**.

Figure 56: Phase histograms for MN1 in all patterns to MN2. **A** MN1 is firing mostly in the phase 0.2 to 0.8. **B** The same phase histogram as in A, but MN1 is color coded in the six possible patterns (legend). **C-H** Phase histograms of single patterns as in B, but with absolute numbers (count).

Figure 57: Phase histograms for MN1 in all patterns to MN4. **A** MN1 is firing nearly during the whole phase, but not shortly after 0 and before 1. The distribution is biphasic, with a higher probability of firing around the phase 0.2 and 0.8. **B** The same phase histogram as in A, but MN1 is color coded in the six possible patterns (legend). **C-H** Phase histograms of single patterns as in B, but with absolute numbers (count).
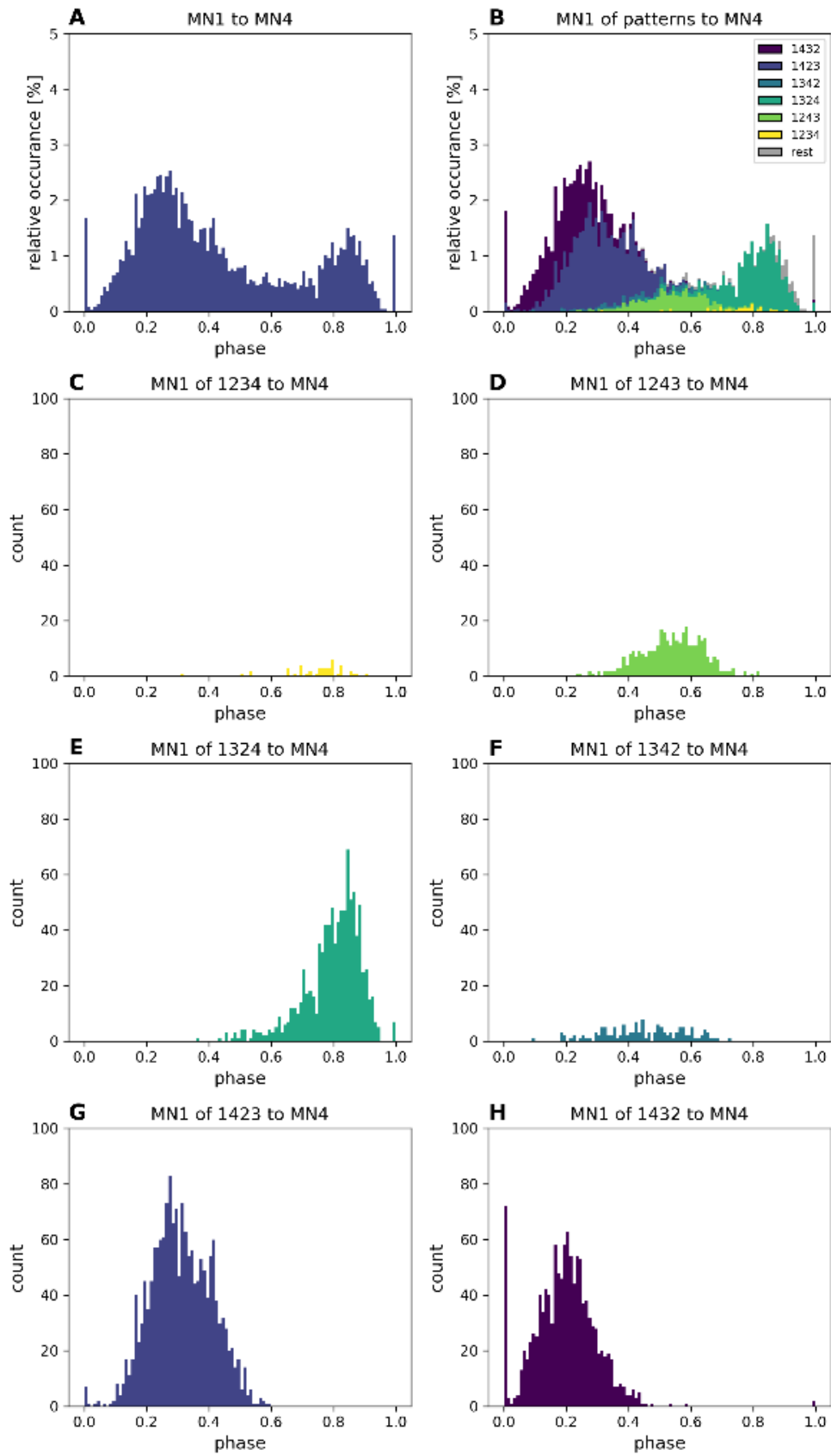
113

Figure 58: Phase histograms for MN1 in all patterns to MN5. **A** MN1 is firing nearly during the whole phase, but not shortly after before 1. **B** The same phase histogram as in A, but MN1 is color coded in the six possible patterns (legend). **C-H** Phase histograms of single patterns as in B, but with absolute numbers (count).
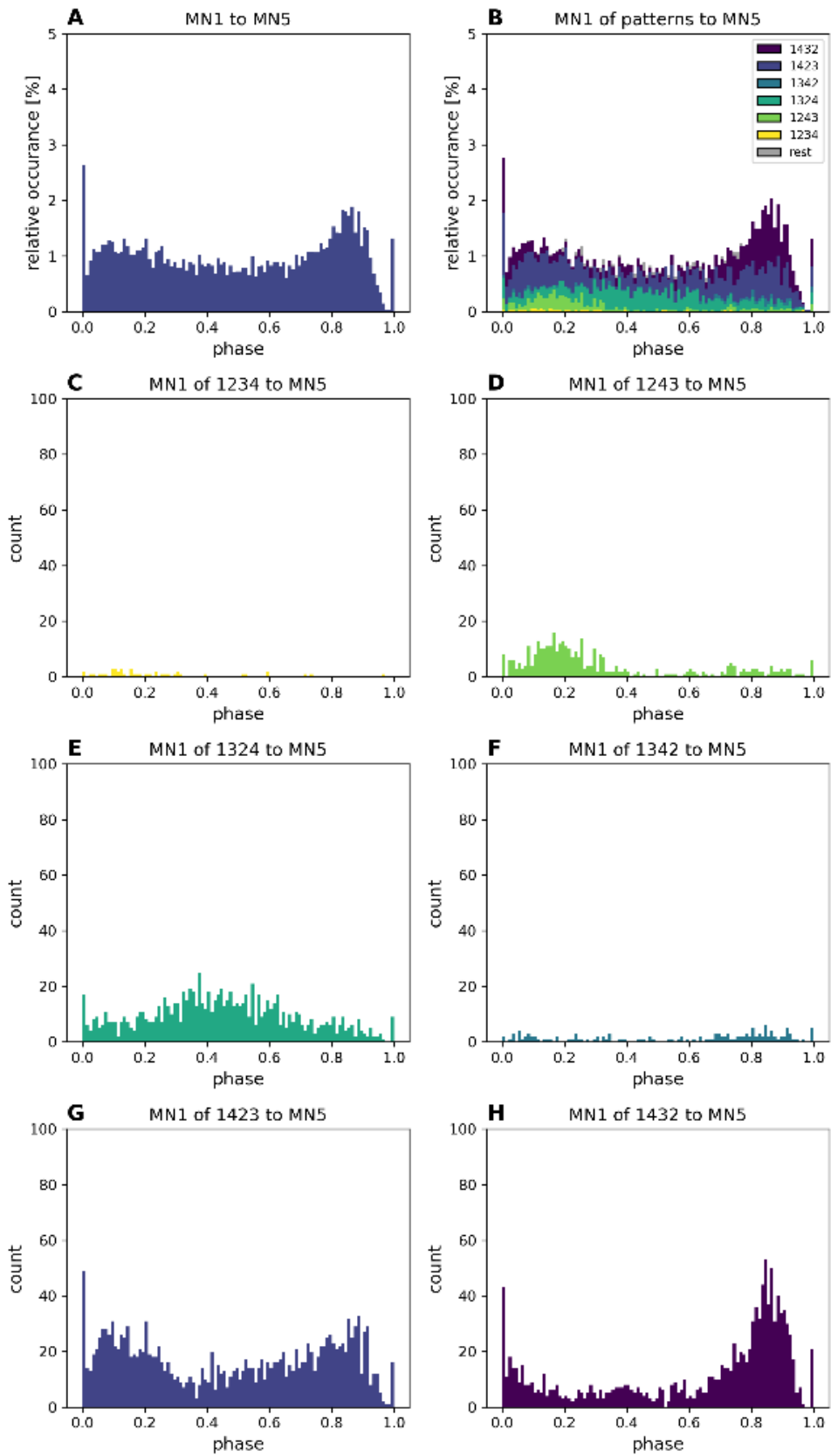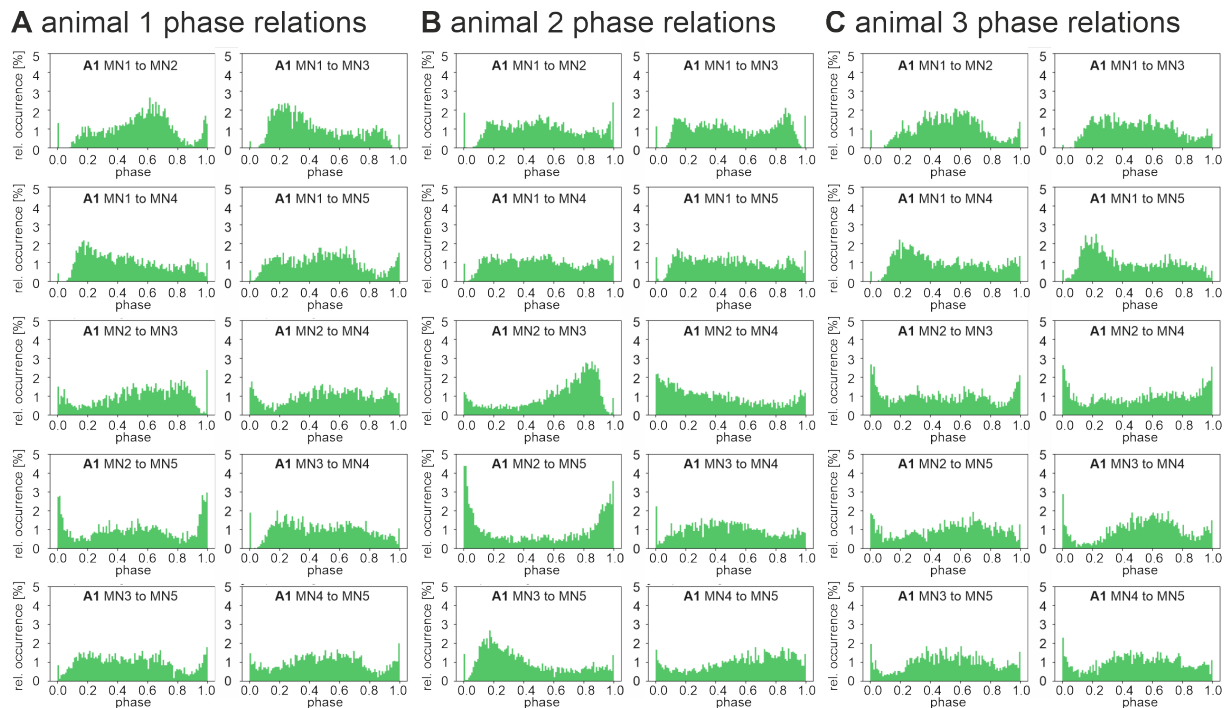
114

Figure 59: Phase histograms for three animals with a *shakB* RNAi knockdown in MN1-5. For each of the three (**ABC**) animals all 10 possible pairwise combinations of MN1-5 are visible. The flight time is 600 sec and approximately 3000 spikes per MN are sorted into 100 bins of the ISI of the compared MN. The phase histograms show some missing near synchronous firing in the phase ~0.0-0.1 or ~0.9-1 but mostly these phases are filled with spikes. The MN2 to MN5 phase histograms for example show a high amount of near synchronous firing, whereas MN1 to MN2 not. (Hürkey et al., 2023).
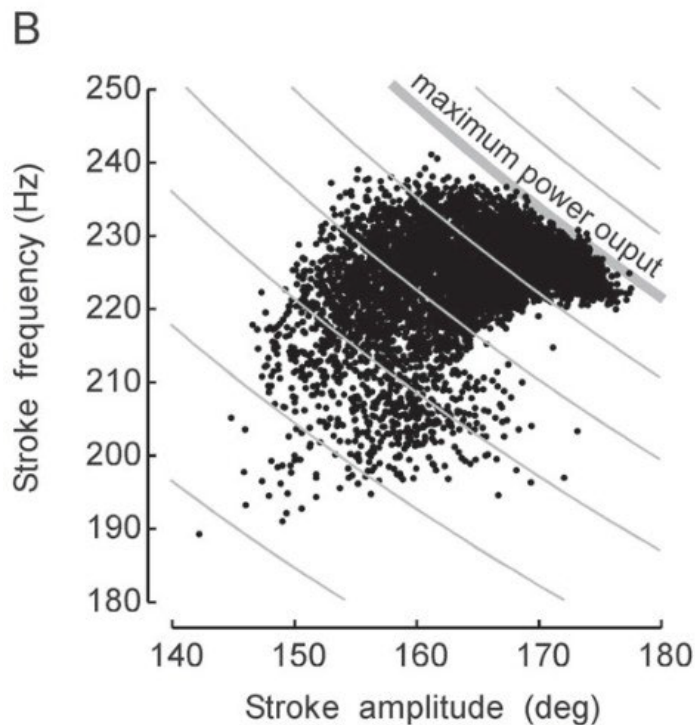
Figure 60: The flight system can reach a maximum power output. On the x-axis is the stroke amplitude (=wingbeat amplitude) and the stroke frequency (=wingbeat frequency) on the y-axis. The maximum power output is depicted by the thicker grey bar. When a high stroke amplitude with ~175 degree is reached the stroke frequency cannot be higher than ~222 Hz. With a lower stroke amplitude of ~160 degrees a stroke frequency of 240 can be reached. (F.-O. F. Lehmann, 2004).

115

Fly stocks

Used genotypes only of male F1 generation.

ShakB RNAi knockdown in DLM-MNs

$$\frac{w}{\rightarrow} ; \frac{\text{GMR23H06} - \text{pBPp65ADZpUw\}attp40}}{+} ; \frac{\text{GMR30A07} - \text{pBPZpGAL4.BD.Uw\}attP2}}{\text{P\{y[+t7.7] v[+t1.8]} = \text{TRiP.HMC04895\}attP2}}$$

ShakB(N) RNAi knockdown in DLM-MNs

$$\frac{w}{\rightarrow} ; \frac{\text{GMR23H06} - \text{pBPp65ADZpUw\}attp40}}{+} ; \frac{\text{GMR30A07} - \text{pBPZpGAL4.BD.Uw\}attP2}}{\text{P\{y[+t7.7] v[+t1.8]} = \text{TRiP.JF02603\}attP2}}$$

ShakB(L) RNAi knockdown in DLM-MNs

$$\frac{w}{\rightarrow} ; \frac{\text{GMR23H06} - \text{pBPp65ADZpUw\}attp40}}{+} ; \frac{\text{GMR30A07} - \text{pBPZpGAL4.BD.Uw\}attP2}}{\text{P\{y[+t7.7] v[+t1.8]} = \text{TRiP.JF02604\}attP2}}$$

ShakB(N+16) overexpression in DLM-MNs

$$\frac{w}{\rightarrow} ; \frac{\text{GMR23H06} - \text{pBPp65ADZpUw\}attp40}}{\text{UAS} - \text{shakB(N} + 16) - 89} ; \frac{\text{GMR30A07} - \text{pBPZpGAL4.BD.Uw\}attP2}}{x}$$

VALIUM control expression in DLM-MNs

$$\frac{w}{\rightarrow} ; \frac{\text{GMR23H06} - \text{pBPp65ADZpUw\}attp40}}{+} ; \frac{\text{GMR30A07} - \text{pBPZpGAL4.BD.Uw\}attP2}}{P\{UAS - GFP.VALIUM10\}attP2}$$

GluClα RNAi knockdown in DLM-MNs

$$\frac{w}{\rightarrow} ; \frac{\text{GMR23H06} - \text{pBPp65ADZpUw\}attp40}}{UAS - GluCl\ RNAi} ; \frac{\text{GMR30A07} - \text{pBPZpGAL4.BD.Uw\}attP2}}{+}$$

Shab RNAi knockdown in DLM-MNs

$$\frac{w}{\rightarrow} ; \frac{\text{GMR23H06} - \text{pBPp65ADZpUw\}attp40}}{+} ; \frac{\text{GMR30A07} - \text{pBPZpGAL4.BD.Uw\}attP2}}{UAS - Shab\ RNAi}$$

Channelrhodopsin-XXL in DLM-MNs

$$\frac{y\ w}{\rightarrow} ; \frac{\text{PBac\{y[+mDint2] w[+mC]} = \text{UAS} - \text{ChR2.XXL\}VK00018}}{\text{GMR23H06} - \text{pBPp65ADZpUw\}attp40}} ; \frac{fru - GAL4}{\text{GMR30A07} - \text{pBPZpGAL4.BD.Uw\}attP2}}$$

Channelrhodopsin-XXL in cholinergic neurons

$$\frac{y1\ w}{\rightarrow} ; \frac{\text{PBac\{y[+mDint2] w[+mC]} = \text{UAS} - \text{ChR2.XXL\}VK00018}}{+} ; \frac{ChaT - GAL4}{+}$$

UAS-RNAi for FMRP fragile X mental retardation protein

$$\frac{\text{w[1118]}+}{\rightarrow} ; \frac{\text{P\{KK107935\}VIE} - 260B}{23H06 - ADZ\ UAS - CD4 - td - GFP} ; \frac{30A07 - DBD}{+}$$

GCaMP8f in the DLMs

$$\frac{\text{w}}{\rightarrow} ; \frac{\text{P\{20XUAS} - IVS - jGCaMP8f\}su(Hw)attP5}{+} ; \frac{\text{P\{Act88F} - GAL4.1.3\}3}{+}$$

Shab overexpression in DLM-MNs

$$\frac{w}{\rightarrow} ; \frac{\text{GMR23H06} - pBPp65ADZpUw\}attp40}{+} ; \frac{\text{GMR30A07} - pBPZpGAL4.BD.Uw\}attP2}{P\{UAS - Shab\}pJFRC81\ attP2}$$

ShakB(N+16) & Shab overexpression in DLM-MNs

$$\frac{w}{\rightarrow} ; \frac{\text{GMR23H06} - pBPp65ADZpUw\}attp40}{UAS - shakB(N+16) - 89} ; \frac{\text{GMR30A07} - pBPZpGAL4.BD.Uw\}attP2}{P\{UAS - Shab\}pJFRC81\ attP2}$$

Trans-tango in period interneurons

$$\frac{y\ w * UAS - myrGFP.QUAS - mtdTomato - 3xHA\}su(Hw)attP8}{w *} ; \frac{\text{P\{w[+mC]} = GAL4 - per.BS\}3}{P\{y[+t7.7]w[+mC] = trans - Tango\}attP40}$$

Trans-tango in LC4 visual interneurons

$$\frac{y\ w * UAS - myrGFP.QUAS - mtdTomato - 3xHA\}su(Hw)attP8}{w *} ;$$

$$\frac{\text{P\{y[+t7.7]w[+mC]} = R47H03 - p65.AD\}attP40}{P\{y[+t7.7]w[+mC] = trans - Tango\}attP40} ; \frac{\text{P\{y[+t7.7]\ w[+mC]} = R86D05 - GAL4.DBD\}attP2}{+}$$

Active zone marker brp short for marking output synapses

$$\frac{y\ w *}{\rightarrow} ; \frac{UAS - brp.S(D3) - mStrawberry}{\text{GMR23H06} - pBPp65ADZpUw\}attp40\ P\{UAS - CD4 - tdGFP\}8M1} ; \frac{\text{GMR30A07} - pBPZpGAL4.BD.Uw\}attP2}{+}$$

Lebenslauf